

# Newsletter n°6

23 December 2024

**ACCORD 4th All Staff Workshop, Norrköping, Avril 2024**



*Credit: Anne-Lise Dhomps*

**ACC  RD**

A Consortium for CONvection-scale modelling  
Research and Development

## CONTACT US

Claude Fischer, ACCORD Programme Manager

@ [pm@accord-nwp.org](mailto:pm@accord-nwp.org)

Anne-Lise Dhomps, Consortium Scientific Secretariat

@ [css@accord-nwp.org](mailto:css@accord-nwp.org)

<http://www.accord-nwp.org/>

# Contents

<b>Edito</b>	3
<i>Claude Fischer, PM</i>	
<b>Nils Gustafsson (1942-2024): Scientific Career and Legacy</b>	4
<i>Magnus Lindskog, Jelena Bojarova, Heiner Körnich, Anna Rutgersson, Michael Tjernström, Nedjeljka Žagar, Åke Johansson</i>	
<b>Headline report from Workshop on Perspectives of data assimilation on hecto-metric scales - In Memoriam of Nils Gustafsson</b>	11
<i>Claude Fischer, PM</i>	
<b>Synergistic operational implementation of 3DnVar in AROME-France</b>	14
<i>Pierre Brousseau, Valérie Vogt, Etienne Arbogast, Loïk Berre, Maud Martet, Vincent Chabot, Vivien Pourret, Guillaume Thomas</i>	
<b>ACCORD DAP visit report: cloud data assimilation using observation penalty function</b>	17
<i>Alina Lerner-Vilu, Siebren de Haan</i>	
<b>TUNING AND DIAGNOSTICS Working Week Report</b>	23
<i>Jana Sanchez Arriola, Åsmund Bakketun, Per Dahlgren, Idir Dehmous, Stephanie Guedj, Magnus Lindskog, Benjamin Menetrier</i>	
<b>Scientific visit on spatial methods with harp and panelification for harp</b>	35
<i>Polly Schmederer, Carlos Peralta, Fabrizio Baordo</i>	
<b>Evaluation of AROME-DUST-CY46 configuration over Southern Algeria</b>	40
<i>Ayoub Mehballi, Mohamed Mokhtari</i>	
<b>The use of ECOCLIMAP Second Generation in AROME and its impact on urban simulation over Algiers</b>	50
<i>Nour El Isslam Kerroumi, Rafiq Hamdi</i>	
<b>AROME-500m operational configurations at Météo-France</b>	62
<i>Salomé Antoine, Yann Seity, Eric Bazile, Ludovic Auger, Rachel Honnert, Patrick Le Moigne, Valéry Masson, Adrien Napoly, Jean Wurtz</i>	
<b>Towards 3D turbulence modelling in AROME at hectometric resolution : Sensitivity in stable regime and complex terrain</b>	74
<i>Léo Rogel, Fabrice Voitus, Eric Bazile, Rachel Honnert</i>	
<b>Reducing the Nocturnal Warm Bias in C-LAEF 1k Simulations for Alpine Valleys</b>	84
<i>Daniel Deacu, Clemens Wastl and Christoph Wittmann</i>	
<b>Analysis of Wind Shear Intensity at Constantine Airport</b>	91
<i>Imad Eddine, Helali Mahiddine, Mohamed Mokhtari Khaled Deiboune</i>	
<b>Recent developments in ACCORD Poland team</b>	99
<i>Piotr Sekula, Jadwiga Róg, Gabriel Stachura, Natalia Szopa, Małgorzata Szczęch-Gajewska, Marcin Kolonko, Bogdan Bochenek</i>	
<b>Patricia around ACCORD 26 beautiful countries in 2024</b>	104
<i>Patricia Pottier</i>	
<b>Previous editions</b>	109
<i>Anne-Lise Dhomps, CSS</i>	



# Edito

Claude Fischer, ACCORD Programme Manager

The previous ACCORD newsletter (NL5) was published in March 2024. Since then, a rather intense activity has taken place in our consortium: the All Staff Workshop in Norrköping, the scientific Working Weeks and Visits organized in ACCORD (with a very high level of realized actions with respect to what was planned), and quite specifically for 2024 the preparation of the scientific strategy for 2026-2030. This NL6 contains two reports from workshops and working weeks held this year, as well as reporting of a few of the scientific visits. One data assimilation workshop was organized in memory of our colleague Nils Gustafsson who is also remembered in this newsletter.

2024 was the fourth year of ACCORD under the governance of the 1st Memorandum of Understanding (2021-2025), and an increasing preparation for organizing the next phase has taken place over this year. These efforts have found their first concrete outcomes in the decisions of the 9th Assembly who met in Reading on 9 December (A/A-9). The A/A-9 indeed approved the scientific strategy prepared since last winter in a bottom-up approach involving the Task Teams, the participants of the Strategy workshop (May, Toulouse) and the drafting team. The strategy proposal benefited from the reviewing process organized with STAC. During this preparation, consensus could not always be reached, or not in a first straight-away manner. In such an exercise, differences of opinions can arise, and indeed did arise most notably on the topic of the common scripting system (CSSy). These differences of opinions have been dealt with by organizing additional consultation across ACCORD families in order to clarify the expectations, the motivations and the benefits. A concrete outcome of the consultation was the proposal of organizing a Task force in charge of drafting a development roadmap for the CSSy. The Task Force shall be active in the first part of 2025. The adoption of the strategy proposal by the ACCORD Members during the Assembly is a first successful step in the preparation of 2026-2030, and all the experts involved in its preparation have been strongly thanked by the Assembly for their hard work. The A/A-9 furthermore adopted some first updates in the Memorandum and this work will be continued in 2025 by a dedicated Working Group. The A/A-9 also approved an overall procedure and timeline for the nomination of all management positions for the next phase. Details on the procedure will be communicated in the beginning of 2025, under the lead of the ACCORD Bureau who will organize the first steps.

Back to the content of the NL6. You will find several contributions in close connection with sub-km modelling seen either from the R&D perspective (how to improve model features: surface parameter description, turbulence, complex orography) or from the perspective of operational experience. NL6 also contains several contributions related to data assimilation (workshop report on the challenges of data assimilation at hectometric scales, assimilation of cloud boguses, the first operational implementation of OOPS and EnVar in an ACCORD institute - two important milestones of our R&D in the past decade). More specific applications are described in the contributions of our Algerian and Polish colleagues (dust modelling, high-resolution forecasts at airports, use of a forecast AI emulator for EPS).

I wish readers to enjoy checking these contributions as an end-of-the-year or beginning-of-the-year more “relaxed” activity, and this NL publication comes along with my best wishes to everyone in ACCORD for happy and peaceful celebrations.

# Nils Gustafsson (1942-2024)

## Scientific Career and Legacy

Magnus Lindskog, Jelena Bojarova, Heiner Körnich, Anna Rutgersson, Michael Tjernström, Nedjeljka Žagar, Åke Johansson

### 1. Introduction

---

Our colleague, mentor and source of inspiration Nils passed away on Sunday 21 July, 2024. With his enthusiastic style and great knowledge, he influenced several generations of researchers in data assimilation (DA) and numerical weather prediction (NWP). Nils was an internationally respected researcher and a world leader in his field. He has contributed fundamentally to the development of regional NWP in Sweden, Europe and worldwide. In particular, Nils excelled in the development of novel methods for data assimilation, being at the forefront of the field for half a century. His international collaborative efforts contributed to the successful NWP consortia HIRLAM and ACCORD. He taught meteorology courses worldwide and ensured the transfer of knowledge to the next generation of researchers and forecasters. As we are mourning the loss of Nils, we honour his legacy and especially his inspiring way to pass on his knowledge to the next generation of NWP developers.

### 2. Childhood and undergraduate studies

---

Nils Gustafsson (Nicku) was born on 2 July 1942 in Angelbos, Lärbro, on the Baltic Sea island of Gotland. Already from his young years his special interest in mathematics became evident, and a lot of thanks to his high school teacher in Visby, assistant professor in mathematics Anton Ulfstand. In August 1963 after finishing his military service Nils went to Uppsala University to study mathematics. When he stepped through the University door on the first day, Nils read the famous motto of Thomas Thorild, a Swedish poet, critic and philosopher “To think freely is great, to think right is greater”. Let my motto be “To think right is great, to think freely is greater” thought Nils. One can say that Nils has lived by this, even if mathematics means a lot of thinking right, you can always find alternative ways to achieve your goal. With completed exams in 1.5 years of mathematics, 1.5 years of computing sciences including numerical methods and 1 year of mathematical statistics Nils obtained a bachelor degree and was quite tired of studies. He started to look for a job, primarily as a computer programmer.

### 3. In service of advancing numerical weather prediction

---

In 1967 a young Nils first took up a position at SMHI in Sweden. It may have been by chance - or maybe not - that Nils came into meteorology. Eventually Nils was offered a job as a programmer at IBM's Nordic Laboratory at Lidingö in Stockholm. Nils would participate in the development of a compiler for the ALGOL programming language. With great pain and pondering young Nils took this offer. The tasks were interesting and probably suited him but “the work served US imperialism”. The war in Vietnam and the conflicting flow of news from there had turned upside down the political thinking of Nils. What made these FNL-soldiers fight against the mighty USA? But the Nils' problem with work was solved in an excellent way. He happened to meet meteorologist Bo Lindgren one Saturday Evening at Gotland Nation (one of the 13 student unions at Uppsala University) pub in

Uppsala and described his problem. "I'll fix this" said Bosse. Shortly thereafter Nils became employed at the SMHI and with all his soul contributed to the research there for more than 50 years.

At SMHI, he initially worked as a computer programmer while studying meteorology at Stockholm University. In 1972, he continued to work with computers to develop time-continuous data assimilation [1], initially together with his supervisor Lennart Bengtsson. An assimilation system developed early by Nils, based on the optimal interpolation methodology, was successfully implemented operationally at SMHI in 1975. It was subsequently used by a number of European meteorological weather services. During the early 1970s, Nils also carried out early research in two of the most important areas of data assimilation. The first deals with the multivariate balance relationship, that an analysis should use as a constraint in order to produce useful forecasts from the start, and the second explores the impact on NWP by the now all-important satellite data. At this early stage, few understood the revolutionary impact that satellite data would have on NWP [2,3].

Some years later (1977), Nils was appointed head of the level IIb FGGE (First GARP Global Experiment) data centre in Norrköping, Sweden, an important node in this pioneering world wide data experiment that greatly accelerated progress in global data assimilation and NWP. Nils led this work with great enthusiasm and took a particular interest in data quality control procedures and database systems where he developed algorithms and designed systems. At the same time, he continued working on refinements of his optimal interpolation analysis scheme.

The next milestone in his career happened in the 1980s, when he became part of the research team that developed the first version of HIRLAM. Based in Copenhagen, Bennert Machenhauer headed the team that built the extremely successful collaborative consortium known as HIRLAM. One of the first international regional NWP models [4,5] was developed. It subsequently became the operational NWP model in several meteorological services in Europe. The first data assimilation implementation in HIRLAM was based on the optimum interpolation scheme developed by Nils [6]. In addition to the Nordic countries, Spain, Ireland and the Netherlands started to use HIRLAM for operational, meso-scale weather prediction and were subsequently incorporated into the HIRLAM consortium. HIRLAM was an integral part of European NWP collaboration on several levels. Over several decades, Nils had many different leading roles in the HIRLAM community; he has been both the project leader and responsible for subprojects. His work included development of a parallel spectral forecast model [7, 8] and the treatment of the lateral boundary conditions [9]. Moreover, he had a unique overview of the entire HIRLAM modelling system [10].

An important part of the HIRLAM system development was its data assimilation component; Nils developed the four-dimensional (4D) variational data assimilation (Var) for the spectral version of the model, including its linearized and adjoint versions. While the purpose of the development was the adjoint modelling, 4D-Var with the spectral model was shown to be competitive with the operational grid-point version. During this period Nils also foresaw the coming importance of parallel computing and hence he developed a parallel code version of an early HIRLAM system. In 1995 Nils took the lead to develop a comprehensive variational data assimilation scheme for limited area models, together with a research group from the HIRLAM member institutes [11, 12, 13, 14]. An important component was the parallelized spectral limited area model, including linearized and adjoint versions. Later Nils led this work for the complete HIRLAM system together with computer experts and colleagues. The HIRLAM variational DA development led to operational implementations of 3D-VAR [15, 16, 17, 18] with use of conventional types of observations [19] and satellite data [20, 21, 22]. HIRLAM 3D-Var became operational at SMHI on 13 June, 2001, where it replaced the old data assimilation system based on optimal interpolation. Around the same time 3D-Var became operational in several other HIRLAM countries.

In the 1990s Nils also took a new role as a lead scientist in BALTEX (the Baltic Sea Experiment), a Regional Hydroclimate Project (RHP) within the Global Energy and Water Exchanges program (GEWEX) of the World Climate Research Programme (WCRP). BALTEX Phase I (1993-2002) focused on the hydrological cycle and the exchange of energy between the atmosphere and the surface



of the Earth, as they control and regulate the climate in a fundamental manner. Nils was managing the re-analysis activities and he early realised the importance of coupling between the atmosphere and the lower boundary [23, 24, 25].

In the early 2000s Nils continued with intense work on the development of HIRLAM 4D-Var [25, 26, 27]. Nils early also realised the potential of using the model within the assimilation process to improve balances and also better utilise the time dimension. Moreover, he understood early on the potential to use the digital filter within variational data assimilation [26] and was the first to develop a digital filter as a weak constraint in 4D-Var in order to control spurious high-frequency oscillations [28]. HIRLAM 4D-Var became operational at SMHI on January 30, 2008 and about the same time also in other HIRLAM countries. During the same period Nils was also involved in several projects on the assimilation of GNSS ZTD [29,30] funded by the European Union. In addition some first steps were taken towards assimilation of cloud-affected satellite radiances from the SEVIRI instrument [31, 32], within the 4D-Var framework, together with an EUMETSAT fellow. Nils was exploiting how to better handle model errors and lateral boundary conditions in the variational procedure [33]. Another milestone in Nils's career took place in 2005, when a close collaboration between the ALADIN and the HIRLAM consortia started. The collaboration kicked off with Nils's visit to Meteo France together with several HIRLAM colleagues to contribute to the development of ALADIN 4D-Var. This was the first step towards HARMONIE-AROME 4D-Var.

In the next decade Nils, together with several colleagues, extended the variational schemes to also include ensemble information [34, 35]. He was also involved in exploring novel approaches for handling non additive errors in data assimilation [36], using the temporal dimension of 4D-Var to better explore observations in 4D-Var [45, 46, 47] and contributed to reviews of data assimilation procedures at km scale [48, 37]. Aware that km-scale data assimilation is largely inherited from synoptic scales, Nils worked on ways to cope with limitations of the background error covariances using ensemble approaches [38]. During this period, Nils also started to familiarise himself with the object oriented framework OOPS, first using a quasi-geostrophic model environment.

In the beginning of 2020 Nils officially retired. However, he continued doing research, attended online meetings and provided advice to colleagues. Moreover, he made significant contributions to the HARMONIE-AROME 4D-Var development and documentation [39]. He also continued the work to explore the merits and drawbacks of various km-scale modelling frameworks [40]. It is also worth mentioning that the HIRLAM 4D-Var scheme developed largely by Nils was still running operationally at SMHI in the 2020s for special customers and was only recently turned off.

#### 4. Academic career and teaching

Nils has been based at the Swedish Meteorological and Hydrological Institute in Norrköping, Sweden, throughout most of his career, but his work in meteorology and numerical weather prediction has influenced many other meteorological services in Europe and worldwide. Long before formally defending his PhD in 1997, Nils was a guest lecturer at many institutes and workshops worldwide. He has published scientific papers and contributed to books [49] throughout his long career, starting long before his PhD. It was in fact a surprise to many that he was not already a doctor before defending his thesis. For his summary thesis he used only a few of his already published papers and very soon after the thesis defence, Nils was awarded the honorary "Docent" title (corresponding to an Associate Professor), also based on already published material. When asked for a vision for NWP by the grading committee at his thesis defence, his answer was kilometre-scale non-hydrostatic models over more limited areas and forced by coarser scale global models; almost three decades this is exactly what the community is doing! As an adjunct professor at Stockholm University, Nils regularly lectured on NWP and supervised several students. He was instrumental in developing the so-called HIRLAM-course at Stockholm University, that became a de facto mandatory course for many students. Formally, Nils has (co)supervised four PhD students [41, 42, 43, 44], but in reality he has advised numerous other early-stage researchers and NWP developers. Together with his students and collaborators, Nils

produced numerous peer-reviewed publications covering various aspects of data assimilation, observation handling and meso-scale prediction.

Nils was a dear guest and speaker at numerous institutes. As an example, he was repeatedly invited to both ECMWF in Europe and NCAR in the United States to lecture and in the latter case to advise on the data assimilation development for the WRF model. Amongst other lectures and courses in Europe, Nils organised an NWP course in Riga, Latvia and was a frequent visitor and lecturer at the University of Gent.

## 5. Summary

---

Although Nils spent his whole career at the Swedish Meteorological and Hydrological Institute in Norrköping (except for a brief period in Norway), he was a global leading researcher. He has been a driving force behind the development of limited-area NWP, in particular data assimilation, for almost half a century. His unique expertise in mathematical, numerical and physical aspects of modern numerical weather prediction has made him one of the giants of NWP worldwide. In addition, he had a keen interest for the operational applications of weather forecasts which is more rare for NWP developers. His inspiring and supportive attitude towards colleagues, students and friends has always fostered cooperation, and mutual learning and respect. Many colleagues around the world have been galvanised by his support and enthusiasm extending the heritage of Nils's work and mentorship to next generations.

He has contributed fundamentally to the development of limited area numerical weather prediction in Sweden, Europe and all over the world. He pioneered and excelled in the development of variational assimilation methods, and until the very end of his life was developing new ideas for km-scale ensemble forecasting and data assimilation. Besides data assimilation methods, throughout his career Nils contributed to the improved use of observational information in NWP. His international collaboration efforts led to successful NWP consortia and provided a foundation for multi-lateral joint operational forecasting. Finally, his international activities in teaching meteorology ensured the knowledge transfer to the next generation and long living of his legacy.

Nils was unwavering and courageous, and he never compromised with the science behind the operational applications. But he was also a very good friend, a generous and inviting person that was never too busy to offer advice or support. He always had the time to share a story, a pizza or perhaps a glass of red wine. He was - and will remain - an inspiration to many and he will be greatly missed by many.

## 6. References

---

- [1] Bengtsson, L. and N. Gustafsson, 1971: An experiment in the Assimilation of Data in Dynamical Analysis. *Tellus*, 23, 328-336.
- [2] Bengtsson, L. and N. Gustafsson, 1972: Assimilation of non-synoptic observations. *Tellus*, 24, 383-399.
- [3] Gustafsson, N., 1979: Impact of satellite information on short range numerical forecasts. Proc. Technical Conference on Use of data from Meteorological Satellites. Lannion, France, 17-21 Sept. 1979, 113-127.
- [4] Gustafsson, N., S. Järvenoja, P. Kållberg, and N. Woetmann Nielsen, 1986: Baseline experiments with a high resolution limited area model. HIRLAM Technical Report, No.1, January 1986, Available from SMHI.
- [5] Gustafsson, N., 1991: The HIRLAM Model. Seminar proceedings on Numerical Methods in Atmospheric Models. Volume II, pp. 115-146. Available from the ECMWF.

- [6] Gustafsson, N., 1986: An operational scheme for three-dimensional objective analysis of meteorological fields. Published as an Appendix in Andersson et al. (1986), 33 pp.
- [7] Gustafsson, N. and A. McDonald, 1996: A comparison of the HIRLAM gridpoint and spectral semi-Lagrangian models. *Mon. Wea. Rev.*, 124, 2008-2022
- [8] Gustafsson, N. and D. Salmond, 1994: A parallel spectral HIRLAM with the data parallel programming model and with message passing. A comparison. In *Coming of Age, Proceedings of the 6th ECMWF Workshop on the use of Parallel processors in Meteorology*.
- [9] Gustafsson, N., 1990: Sensitivity of limited area model data assimilation to lateral boundary condition fields. *Tellus*, 42A, 109-115.
- [10] Gustafsson, N., 1993: HIRLAM 2 Final Report. HIRLAM Technical Report, Nr 9, 129 pp. Available from SMHI, S-60176 Norrköping, Sweden.
- [11] Huang, X.-Y., Gustafsson, N. and Källén, E., 1997: Using an adjoint model to improve an optimum interpolation based data assimilation system. *Tellus*, 49, 151-176. DOI: 10.3402/tellusa.v49i2.14461.
- [12] Gustafsson, N. and Huang, X.-Y. 1996: Sensitivity experiments with the spectral HIRLAM and its adjoint. *Tellus*, 48A, 501-517.
- [13] Gustafsson, N., 1996: Data assimilation for Mesoscale models. To appear in the *Proceedings from the 1996 ECMWF Seminars on Data Assimilation*. Available from ECMWF.
- [14] Gustafsson, N., P. Lönnberg and J. Pailleux, 1996: Data assimilation for high resolution limited area models. *J. of Met. Soc. of Japan*, 75, 367 - 382.
- [15] Gustafsson, N., Hörnquist, S., Lindskog, M., Berre, L., Navascués, B., Thorsteinsson, S., Huang, X.-Y., Mogensen, S. K. and Rantakokko, J., 1999. Three-dimensional variational data assimilation for a high resolution limited area model (HIRLAM). HIRLAM Technical Report, 40, 72 pp.
- [16] Gustafsson, N., Berre, L., Hörnquist, S., Huang, X.-Y., Lindskog, M., Navascués, B., Mogensen, K. S. and Thorsteinsson, S., 2001: Three-dimensional variational data assimilation for a limited area model. Part I: General formulation and the background error constraint. *Tellus*, 53A, 425-446.
- [17] Berre, L., 1997: Non-separable structure functions for the HIRLAM 3DVAR. HIRLAM Tech. Rep. 30, 38 pp. [Available from Met Éireann, Glasnevin Hill, Dublin 9, Ireland.]
- [18] Gustafsson, N., Landelius, T., Lindskog, M., Schyberg, H., Thorsteinsson, S., Tveter, F. and Vignes, O., 2001. Assimilation of AMSU-A radiances in HIRLAM 3D-Var. Technical Proceedings of The Eleventh International ATOVS Study Conference, Budapest, Hungary 20- 26 September 2000, 129-137.
- [19] Lindskog, M., Gustafsson, N., Navascués, B., Mogensen, K. S., Huang, X.-Y., Yang, X., Androe, U., Berre, L., Thorsteinsson, S. and Rantakokko, J., 2001. Three-dimensional variational data assimilation for a limited area model. Part II: Observation handling and assimilation experiments. *Tellus*, 53A, 447-468.
- [20] Schyberg, H., Landelius T., Thorsteinsson S., Tveter F., Vignes, O., Amstrup B., Gustafsson N., Järvinen H. and Lindskog M., Use of ATOVS data in the HIRLAM 3D-Var system, HIRLAM Workshop Report, March 2002, 65-67.
- [21] Schyberg, H., Landelius T., Thorsteinsson S., Tveter F., Vignes, O., Amstrup B., Gustafsson N., Järvinen H. and Lindskog, M., 2003: Assimilation of ATOVS data in the HIRLAM 3D-VAR system. HIRLAM Technical Report. Available from SMHI.
- [22] Gustafsson, N., L. Nyberg and A. Omstedt, 1998: Coupling a High-resolution atmospheric model and an ocean model for the Baltic Sea. *Monthly Weather Review*, 126, 2822-2846.



- [23] Andersson, T. and N. Gustafsson, 1994: Coast of Departure and Coast of Arrival: Two Important Concepts for the Formation and Structure of Convective Snowbands over Seas and Lakes. *Monthly Weather Review*, 122, 1036-1049.
- [24] Ljungemyr, P., N. Gustafsson and A. Omstedt, 1996: Parameterization of lake thermodynamics in a high-resolution weather forecasting model. *Tellus*, 48A, 608-621.
- [25] Huang, X.-Y., Yang, X., Gustafsson, N., Mogensen, K. and Lindskog, M., HIRLAM 4DVAR. 2002. HIRLAM Newsletter, No. 41, June 2002, 45-50.
- [26] Huang, X.-Y., Yang, X., Gustafsson, N., Mogensen, K.S. and Lindskog, M., 2002: Four-dimensional variational data assimilation for a limited area model. Technical Report 57, 44pp. Available from HIRLAM-5, c/o Per Undén, SMHI, S-60176 Norrköping, Sweden.
- [27] Gustafsson, N., Huang, X.-Y., Yang, X., Mogensen, K., Lindskog, M., Vignes, O., Wilhelmsson, T. and Thorsteinsson, S., 2012. Four-dimensional variational data assimilation for a limited area model. *Tellus A* 2012, 64, 14985, DOI: 10.3402/tellusa.v64i0.14985.
- [28] Gustafsson, N., 1992: Use of a digital filter as weak constraint in variational data assimilation. Workshop proceedings on Variational assimilation, with special emphasis on three- dimensional aspects, pp 327-338. Available from the ECMWF.
- [29] Elgered, G., L. Gradinarsky, N. Gustafsson, J. Johansson, M. Ridal, and B. Stoew, Meteorological Applications of the Swedish Ground-Based GPS Network, Proceedings of ESA Workshop: “Atmospheric Remote Sensing using Satellite Navigation Systems”, Matera, Oct. 13–15, 2003.
- [30] Ridal, Martin & Gustafsson, Nils. (2003). Assimilation of ground-based GPS data within the European COST-716 action.
- [31] Stengel, M., P. Undén, M. Lindskog, P. Dahlgren, N. Gustafsson, and Bennartz, R., 2009. Assimilation of SEVIRI infrared radiances with HIRLAM 4D-Var. *Q. J. R. Meteorol. Soc.*, 135 (645), 2100-2109.
- [32] Stengel, M., M. Lindskog, P. Undén, N. Gustafsson, and R. Bennartz, 2010. An extended observation operator in HIRLAM 4D-Var for the assimilation of cloud-affected satellite radiances. *Q. J. R. Meteorol. Soc.* doi:{10.1002/qj.621}.
- [33] Dahlgren, P., and N. Gustafsson, 2012: Assimilating host model information into a limited area model. *Tellus*, 64A, 15836, <https://doi.org/10.3402/tellusa.v64i0.15836>.
- [34] Gustafsson, N., Bojarova, J. and O. Vignes, 2014. Hybrid Variational Data Assimilation for High Resolution Limited Area Model (HIRLAM). *Non-linear Processes in Geophysics*, 21, 303–323, <https://doi.org/10.5194/npg-21-303-2014>.
- [35] Gustafsson, N. and Bojarova, J. (2014) Four-dimensional ensemble variational(4D-En-Var) data assimilation for the HIRLAM. *Nonlinear Processes in Geophysics*, 21, 745–762. <https://doi.org/10.5194/npg-21-745-2014>.
- [36] Landelius, T., J. Bojarova, N. Gustafsson and M. Lindskog, 2013: Correction of non-additive errors in variational and ensemble data assimilation using image registration, in *Geophysical Research Abstracts Vol. 15*, EGU2013-3891, 2013.
- [37] Gustafsson, N., Janjić, T., Schraff, C., Leuenberger, D., Weissmann, M., Reich, H., Brousseau, P., Montmerle, T., Wattrelot, E., Bučánek, A., Mile, M., Hamdi, R., Lindskog, M., Barkmeijer, J., Dahlbom, M., Macpherson, B., Ballard, S., Inverarity, G., Carley, J., Alexander, C., Dowell, D., Liu, S., Ikuta, Y. and Fujita, T. 2018. Survey of data assimilation methods for convective-scale numerical weather prediction at operational centres. *Quart. J. Roy. Meteorol. Soc.*, 144, 1218-1256, DOI: 10.1002/qj.3179.

- [38] Jelena Bojarova & Nils Gustafsson (2019) Relevance of climatological background error statistics for mesoscale data assimilation, *Tellus A: Dynamic Meteorology and Oceanography*, 71:1, 1-22, DOI: 10.1080/16000870.2019.1615168
- [39] Barkmeijer, Jan, Lindskog, Magnus, Gustafsson, Nils, Bojarova, Jelena, Azad, Roohollah, Monteiro, Isabel, Escribà, P. , Whelan, Eoin, Ridal, Martin, Sanchez Arriola, Jana, Vignes, Ole, Stappers, Roel and Randriamampianina, Roger, HARMONIE-AROME 4D-VAR, 2021. [https://knmi-wwwknminl-prd.s3.eu-west-1.amazonaws.com/system/data\\_center\\_publications/files/000/071/042/original/HARMONIE\\_AROME\\_4DVAR\\_V2.pdf?1671207922](https://knmi-wwwknminl-prd.s3.eu-west-1.amazonaws.com/system/data_center_publications/files/000/071/042/original/HARMONIE_AROME_4DVAR_V2.pdf?1671207922)
- [40] Abolfazl Neyestani, Nils Gustafsson, Sarmad Ghader, Ali Reza Mohebalhojeh, Heiner Körnich, Operational convective-scale data assimilation over Iran: A comparison between WRF and HARMONIE-AROME, *Dynamics of Atmospheres and Oceans*, 10.1016/j.dynatmoce.2021.101242, 95, (101242), (2021).
- [41] Berre, L., 2001 : Représentation des covariances spatiales des erreurs de prévision pour une assimilation variationnelle dans un modèle atmosphérique à aire limitée. PhD Thesis of Paul Sabatier University, Toulouse, France, 250 pp.
- [42] Žagar, Nedjeljka, 2004: Dynamical aspects of atmospheric data assimilation in the tropics. Thesis for the degree of Filosofie Doctor at Stockholm University. Available from Stockholm University, Sweden.
- [43] Lindskog, Magnus, 2007: On errors in meteorological data assimilation. Thesis for the degree of Filosofie Doctor. Available from SMHI ,Norrköping, SE-601 76, Norrköping, Sweden.
- [44] Bojarova, Jelena, 2010: Toward sequential data assimilation for numerical weather prediction (NWP) models using Kalman filter tools. Available from SMHI ,Norrköping, SE-601 76, Norrköping, Sweden.
- [45] Žagar, N., N. Gustafsson and E. Källén, 2004: Variational data assimilation in the tropics: the impact of a background error constraint. *Q.J.R. Meteorol. Soc.*, 130, 103-125. doi: 10.1256/qj.03.13
- [46] Žagar, N., N. Gustafsson and E. Källén, 2004: Dynamical response of equatorial waves in four-dimensional variational data assimilation. *Tellus*, 56A, 29-46. <http://dx.doi.org/10.3402/tellusa.v56i1.14389>
- [47] Zaplotnik, Ž., N. Žagar, and N. Gustafsson, 2018: An intermediate-complexity model for the four-dimensional variational data assimilation including moist processes. *Q. J. R. Meteorol. Soc.*, 144, 1772-1787, <https://doi.org/10.1002/qj.3338>
- [48] Žagar, N., J. Bojarova, N. Gustafsson, T. Janjić, G-J. Marseille, M. Rennie, A. Stoffelen and M. Šavli, 2017: Summary of Ljubljana workshop on “Mesoscale data assimilation and the role of winds in limited-area models for NWP in Europe”, *ALADIN-HIRLAM Newsletter*, 8, 119-123.
- [49] Gustafsson, N, 1981: A Review of Methods for Objective Analysis. Pages 17-76 in *Dynamic Meteorology: Data Assimilation Methods* by Lennart Bengtsson, Michael Ghil, Erland Källén. <https://doi.org/10.1007/978-1-4612-5970-1>.

# Headline Report from the Workshop on Perspectives of data assimilation on hecto-metric scales

## In Memoriam of Nils Gustafsson

Short report prepared for the ACCORD Newsletter by the editors



*Figure 1: Tofta, Gotland, Sweden, 10- 12 September, 2024*

Hereafter is a summary headline report from the Workshop held in September. The full report is available here [https://www.umr-cnrm.fr/accord/accord/accord/accord/IMG/pdf/wr\\_report\\_hecdca.pdf](https://www.umr-cnrm.fr/accord/accord/accord/accord/IMG/pdf/wr_report_hecdca.pdf).

The presentations are available here:

[https://drive.google.com/drive/u/0/folders/1xJmkoklTZBtG\\_aaHuPa6ZSuPMwOPuqi](https://drive.google.com/drive/u/0/folders/1xJmkoklTZBtG_aaHuPa6ZSuPMwOPuqi)

The workshop participants were: Loïk Berre (remote), Jelena Bojarova, Pau Escribà, Elias Holm, Heikki Järvinen (remote), Tomas Landelius, Magnus Lindskog, Kristian Mogensen, Patrick Samuelsson, Michael Tjernström, Ole Vignes, Tomas Wilhelmsson, Xiaohua Yang. It was organized in the context of the qCONDOR (a Quasi CONTinuous Data assimilation for nOwcasting and a very short Range forecasting ) project of the Swedish National Space Board (SNSA) and is sponsored by the International Meteorological Institute (IMI) Visitors Program of The Meteorological Institute at Stockholm university.



The content of the workshop was organized as follows:

### **Workshop scope**

This workshop is focusing on data assimilation for hectometric scales. How can we build on previous experiences from larger scales and what are the key aspects to address when approaching higher resolutions? Here we will try to take a variety of different aspects into account, including assimilation algorithms, resolution versus domain size, uncertainty estimates and modeling,

observation handling, coupling strategy, model physics, model spin-up, optimal length of assimilation window as well as computational aspects. How should the efficient data assimilation algorithm be designed? How can we profit in the best way from rapidly emerging technologies of data processing and analysis, known as Machine Learning (ML) or Artificial Intelligence (AI). Do we need the data assimilation at all on the hecto-metric scales? The workshop was organized in the context of the qCONDOR (a Quasi CONTinuous Data assimilation for nOwcasting and a very short Range forecasting ) project of the Swedish National Space Board (SNSA) and was sponsored by the International Meteorological Institute (IMI) Visitors Program of The Meteorological Institute at Stockholm university. The primary activity IMI is to support scientific visits to Sweden within the atmospheric, oceanic and climate sciences and closely related fields. Roughly 50 scientific visits are made possible each year through funding from the institute.

### **Scientific topics**

- Nonlinearity and non-gaussianity of the error evolution at hecto-metric scales and appropriate data assimilation algorithms
- Machine Learning and Artificial Intelligence
- Computational aspects
- Uncertainty estimates and modeling of these
- Predictability, model spin-up and adjustment processes
- Resolution, domain size, update frequency and length of the assimilation window
- Observability at hectometric scales, observation handling and quality control
- Process-oriented modeling: atmosphere – land surface – ocean interactions and challenges of coupled data assimilation
- Model development (vertical)+opt model
- Quality/success ratio

### **Workshop recommendations**

- Here we provide a short summary of main findings. These could be addressed from the perspective of short (up to two years, S) and long (five years, L) time scales of the developments.
- There is room for innovation regarding improvements of observation quality control and bias correction procedures, possibly utilizing elements of machine learning. (S)
- Improvement of boundary information within the data assimilation procedure is needed, regarding both coupling procedures and use of observations. (S)
- It is seen as beneficial to focus development towards coupled atmospheric-land-ocean data assimilation systems. (S)
- To benefit from the data assimilation also the model improvements are needed of particularly vertical profiles and in stable conditions. Such model improvements could benefit from objective model parameter tuning. (S)
- Verification scores emphasizing high impact weather are needed. (S)

- The Limited Area Modelling (LAM) community should tighten relationships with global Earth Modelling. The quality of LAM forecasts will always depend on the quality of boundary conditions provided by the host model. (S)
- Ensemble methods allow non linear effects of observation and model uncertainties to be simulated in data assimilation and forecasts. They are important to consider in order to optimize the impact of highly dense observations with flow-dependent error covariances in high resolution DA and also in order to initialise associated ensemble predictions. (S)
- Continuous data assimilation procedure with progressively increasing data assimilation window provides an opportunity to allow for late arriving observations in advanced data assimilation procedures. (S)
- Modular and transparent code structure that is generic enough to be executed on different computer architectures is needed in order to utilize the best technological advances, for example to combine physics-based and statistical models. (S)
- Insufficient understanding and handling of spatially correlated observation errors hampers hecto-metric scale data assimilation. (L)
- While ensemble approaches are already operational for km-scale NWP, ensemble forecasting at higher resolution implies high computational cost, depending on future available computer power, target resolution and domain sizes. Variety of approaches can be explored to optimize ensemble generation, including multi-resolution ensemble, multi-scale Monte Carlo, generative AI models to enlarge ensemble size. (L)
- Assimilate aggregated entities (e.g. moments) to reduce position errors and obtain easier correlated error structures. (L)
- Use of AI approaches like diffusion or normalizing flow to turn non-Gaussian errors into Gaussian ones to allow for efficient DA methods. (L)
- Employ AI auto-encoders to establish the physical balances at the hectometric scale and constrain the DA solution to obey these. (L)
- Exploit possibility of obtaining auto-differentiation when converting CPU codes to GPU ones. Opens up for having the full non-linear and the tangent-linear models in the cost function. (L)

### **Agenda.**

The detailed agenda along with the extended summary of the outcome of the discussions are available in the full workshop report (see link above).

### **In Memoriam of Nils Gustafsson**

# Synergistic operational implementation of 3DEnVar in AROME-France

Pierre Brousseau, Valérie Vogt, Etienne Arbogast, Loïc Berre, Maud Martet, Vincent Chabot, Vivien Pourret, Guillaume Thomas (Météo-France/CNRM/GMAP)

A new data assimilation (DA) scheme has been implemented operationally in AROME-France on 15 October 2024 with cycle 48T1 : a Three-Dimensional Ensemble-Variational formulation (3DEnVar) formulation is now used, replacing the 3D-Var scheme, which was previously operational since 2008. This corresponds to major improvements in background error covariances, which determine how locally observed information is spatialised by the analysis scheme, from observation locations towards surrounding model gridpoints. More precisely, the 3DEnVar analysis uses flow-dependent ensemble-based background error covariances, instead of static and horizontally uniform covariances in 3D-Var. This allows observed information to be better assimilated, as it is spatialised in a way that accounts for the meteorological situation : analysis corrections to the background are now more localised and more intense for instance in convective areas, which are affected by smaller scale uncertainties than in stable large-scale anticyclonic regions. This leads initial states to be made more accurate, e.g. for predicting severe precipitation events, as shown below by experimentations and evaluations over long periods of several months in cycle 48T1, in both research and e-suite configurations.

Such evaluations indicate that, thanks to 3DEnVar, the average quality of precipitation and wind gust forecasts is improved by about 4 % over the next two days of prediction. This is partly related to improvements in humidity analyses and forecasts, as shown by Figure 1 over a 6-month period. This improvement is valid over all seasons, and it is particularly noticeable over summer and autumn with severe thunderstorms. This is illustrated here by a case study over South France in Figure 2. The left panel corresponds to reference observations of 20-hour accumulated precipitation (in mm) on 19 September 2020. The top row corresponds to forecasts issued from the previous 3D-Var scheme : depending on the analysis time, an intense precipitation event is sometime predicted, but its location is misplaced compared to the real area identified by the yellow ellipsis. The bottom row illustrates the corresponding forecasts provided by the new 3DEnVar analyses : heavy precipitation is now systematically predicted in the correct region. Actually, it has been noticed similarly over many such convective cases that successive forecasts valid at the same time are now much more consistent with each other, which increases the reliability and confidence in such severe event predictions. These are numerous good examples which indicate that underlying 3DEnVar analysis increments, based on non linear ensemble runs, can provide consistent analyses and predictions of deep convection and of associated strongly non linear moist processes.

This is the most major evolution in data assimilation algorithms for AROME-France since its operational start in 2008. It has been made possible by several years of active research and development work, which have been conducted using the Object-Oriented Prediction System (OOPS), developed in collaboration with ECMWF and ACCORD partners. The OOPS system has been found to facilitate such innovative developments : it allows different components of the assimilation system, such as background error covariances, to be defined and handled in a flexible way. The 3DEnVar formulation, which is run at 1.3 km resolution in one-hourly DA cycling, uses information provided by



an AROME Ensemble Data Assimilation (EDA) system : the EDA simulates the evolution of errors in successive analysis and forecast steps ; it provides a sample of flow-dependent background perturbations, which are used to specify dynamical background error covariances in 3DEnVar. Error simulation is achieved in the EDA by adding and propagating observation and model perturbations in 50 parallel DA runs at 3.2 km resolution, corresponding to 50 different members of the EDA. These synergistic approaches, based on ensemble-variational (EnVar) formulations, OOPS and EDA, have been also applied to achieve major improvements in the representation of flow-dependent background error covariances in ARPEGE data assimilation ; this leads to great positive impacts for ARPEGE forecasts too. This illustrates large benefits of synergistic research, developments and results for limited area and global data assimilation. Several ACCORD partners are also actively experimenting 3DEnVar in this OOPS framework for their own system.

Moreover, it must be underlined that 3DEnVar has now enabled the operational assimilation of massive Mode-S observations in AROME-France, with clear positive impacts associated to the use of flow-dependent covariances. The eased possibility to include hydrometeors in the EnVar control variable with state-dependent covariances will then allow, within the next e-suites, the direct assimilation of radar reflectivities (without Bayesian inversion), allsky microwave and infrared radiances (ex : MTG-IRS) and lightning data (ex : MTG-LI). The OOPS and EnVar frameworks have been also adopted to renovate the land surface data assimilation, and to experiment ocean/atmosphere coupled data assimilation. One of the next major steps is now the foreseen implementation of a Four-Dimensional Ensemble Variational analysis (4DEnVar) in AROME-France, in order to assimilate observations at high frequency (every 15 minutes) in a new consistent four-dimensional way. This 4DEnVar analysis scheme will be part of the next AROME-France e-suite starting in 2025 with cycle 49T1.

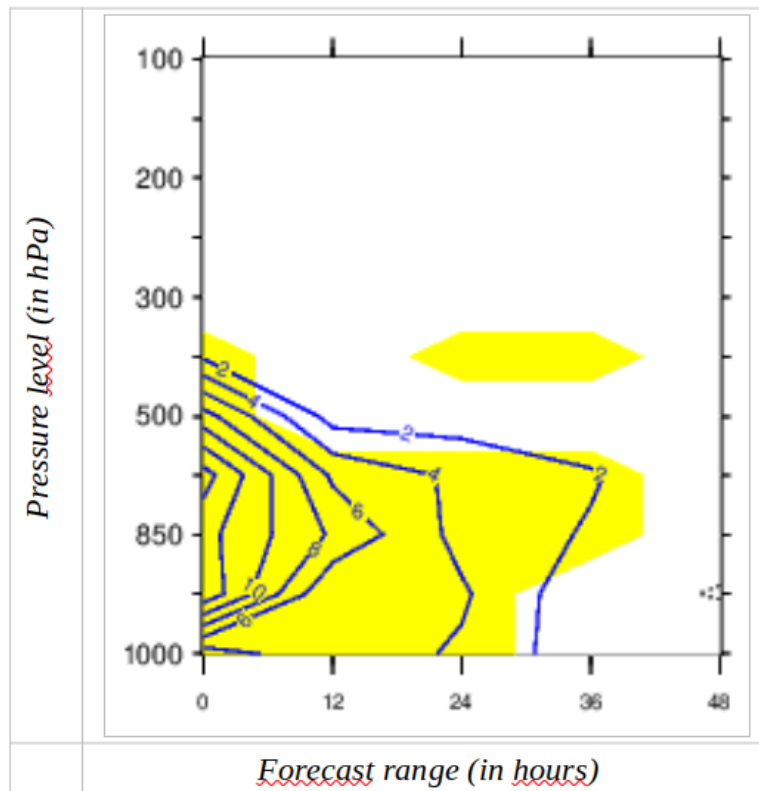


Figure 1 : Percentage of RMSE forecast differences between 3D-Var and 3D-EnVar experiments over a 6-month period, from 16/09/2020 to 01/03/2021, as a function of height (in hPa) and forecast range (in hours). RMSE values are computed against radiosonde measurements (verifying reference). Blue isolines and positive values indicate that RMSE values are smaller for 3D-EnVar than for 3D-Var. Yellow areas correspond to values which are statistically significant according to the bootstrap test.

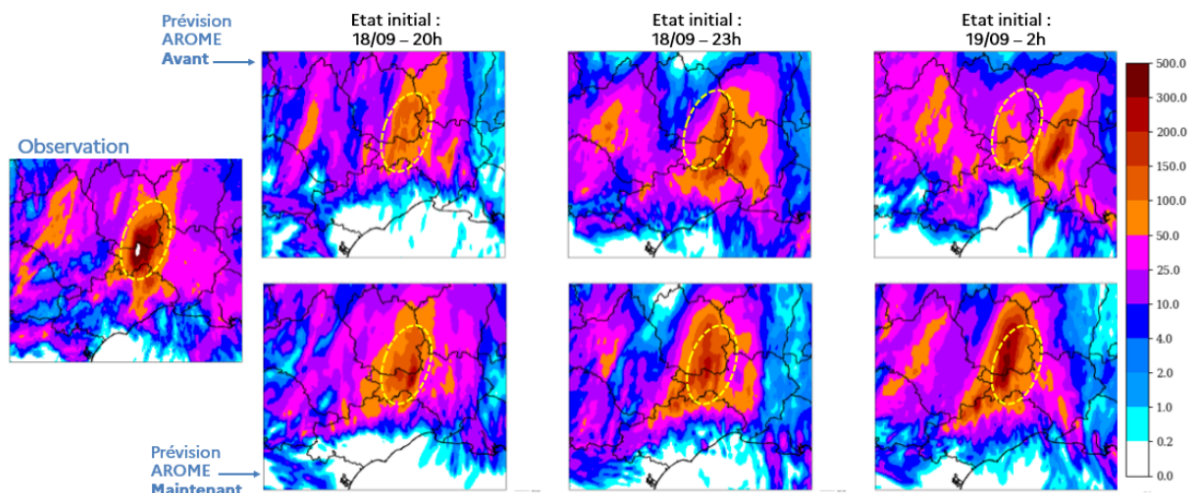


Figure 2 : 20-hour accumulated precipitation (in mm) for a High Precipitation Event over South France from 19/9/2020 at 6 UTC to 20/9/2020 at 2 UTC. Left panel : reference observation-based measurements. Top and bottom rows : predictions issued from different analysis times : 18 UTC (2nd column) on 18/09/2020, 21 UTC (3rd column) on 18/09/2020 and 00 UTC on 19/09/2020 (last column). Analyses are based on either 3D-Var (top row) or 3D-EnVar (bottom row). The yellow ellipsis identifies the region where heavy precipitation has been observed.

# ACCORD DAP visit report: cloud data assimilation using observation penalty function

Alina Lerner-Vilu, Siebren de Haan

## 1 Introduction

In the cloud data assimilation approach proposed by Siebren de Haan, we define the observation penalty function constraints based on the relative humidity profile at the ceilometer site. This method penalizes excessively high relative humidity values outside of cloud layers and excessively low values inside them. The concept is presented schematically in Figure 1. We assume the cloud layer is located between  $h_b$  - cloud base height - and  $h_t$  - cloud top height. For simplicity, we assume critical relative humidity is 100%, and  $\alpha$  is a drying threshold value. It implies:

$$\begin{cases} RH = 1 & \text{if } h_b \leq h \leq h_t \\ RH \leq \alpha < 1 & \text{otherwise} \end{cases} \quad (1)$$

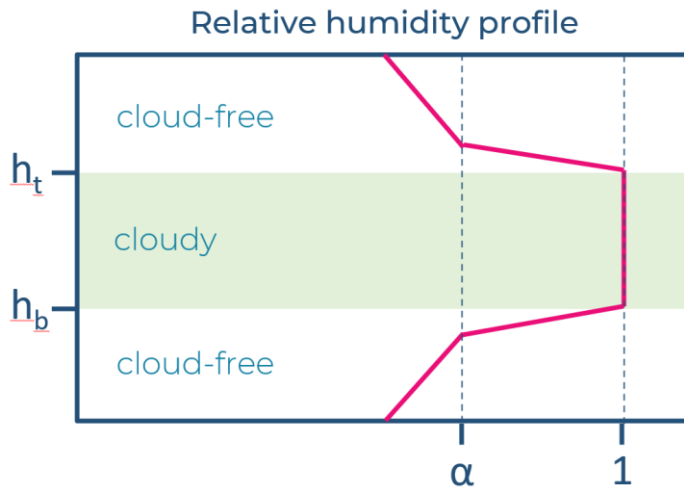


Figure 1. Schematic representation of the assimilation concept.

With the support of ACCORD, the collaboration started on 2023. We created a setup for the Harmonie-Arome cycle 43, which incorporates this method. In the spring of 2024, a series of successful single-observation experiments were conducted, demonstrating that the method works technically and is capable of producing analysis increments in the correct direction.

The methodology details, derivation and single-observation experiments results are going to be explained in an article, which is by now submitted to a peer-reviewed journal. In this report we demonstrate the results of the first experiment based on the real observations.

## 2 Observations preparation

We run the Harmonie-Arome model using DKCOEXP domain for the period of 2024081606-2024081609 with one data assimilation (DA) cycle at 9 UTC. Only the cloud observations were included in the DA in order to assess the cloud DA results isolated from others.

Cloud top height observations were derived from NWCSAF NetCDF output. Cloud base height observations were read from SYNOP BUFR messages. Then, we collocated the cloud base and cloud

top observations. At each SYNOP station site, where we got cloud base height from, we search for the cloud top values from the 9 closest satellite product grid points, which means we get data from 9 km radius around ground-based observation.

For now, some restrictions were applied to the observations to be assimilated. We used:

- only the clouds which cloud tops are warmer than 0 °C;
- only the clouds which bases are located lower than 500 hPa;
- cloud cover is more than 3 octas;
- only the data points, where both cloud base and cloud top are detected OR neither cloud base nor cloud top are detected (cloudy or cloud-free in both observation sources).

Therefore, using the cloud base and top heights we printed out the OBSOUL file in the needed format. The OBSOUL structure we use implies supplying every model layer with the measured cloud fraction. Model levels, where a cloud layer has been detected, are assigned a positive value of cloud fraction, cloud-free model levels are assigned value of 0 of cloud fraction.

Thus, critical RH value is derived by parameterizing the cloud fraction as a function of the saturation deficit, which is integrated with the HARMONIE condensation scheme. Setting RH to the saturation inside the observed cloud layer provokes the model's cloud microphysics scheme to convert excess water vapor to clouds.

### 3 Results

The test run was successfully complete. 97 cloud observations (see Figure 2) passed screening and minimisation. A lot of observations were dropped before surpassing the DA cycle, during the OBSOUL printing process. In the future we should reassess the observation processing we do before Bator.

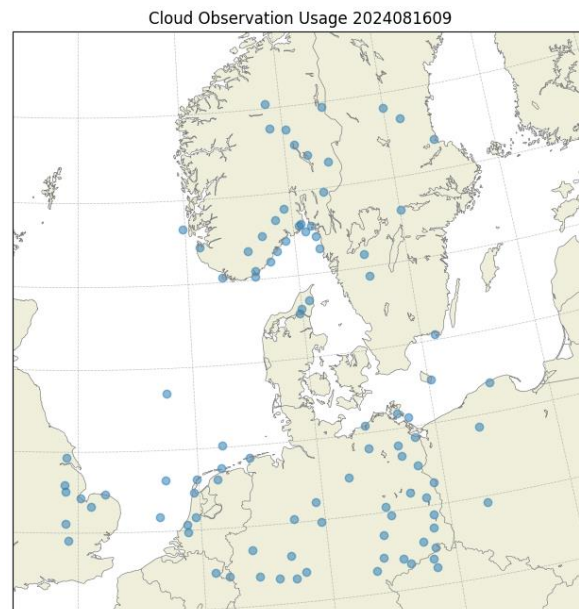


*Figure 2. Locations of the observations used in the assimilation cycle.*

Figure 3 shows the analysis minus first guess specific humidity increments at level 55 and 45, as well as low and middle cloud fraction increments, and NWCSAF cloud top height picture for comparison. We can see some strong positive increments of humidity around the Netherlands, near the Norway shore, above Sweden, Germany and Polish shore. As well as negative increments in vast areas. The increments are strongly smoother over large areas as can be often seen in 3D-Var. The positive side is the ability of the scheme to produce the clouds, which is seen from cloud fraction increments plots.



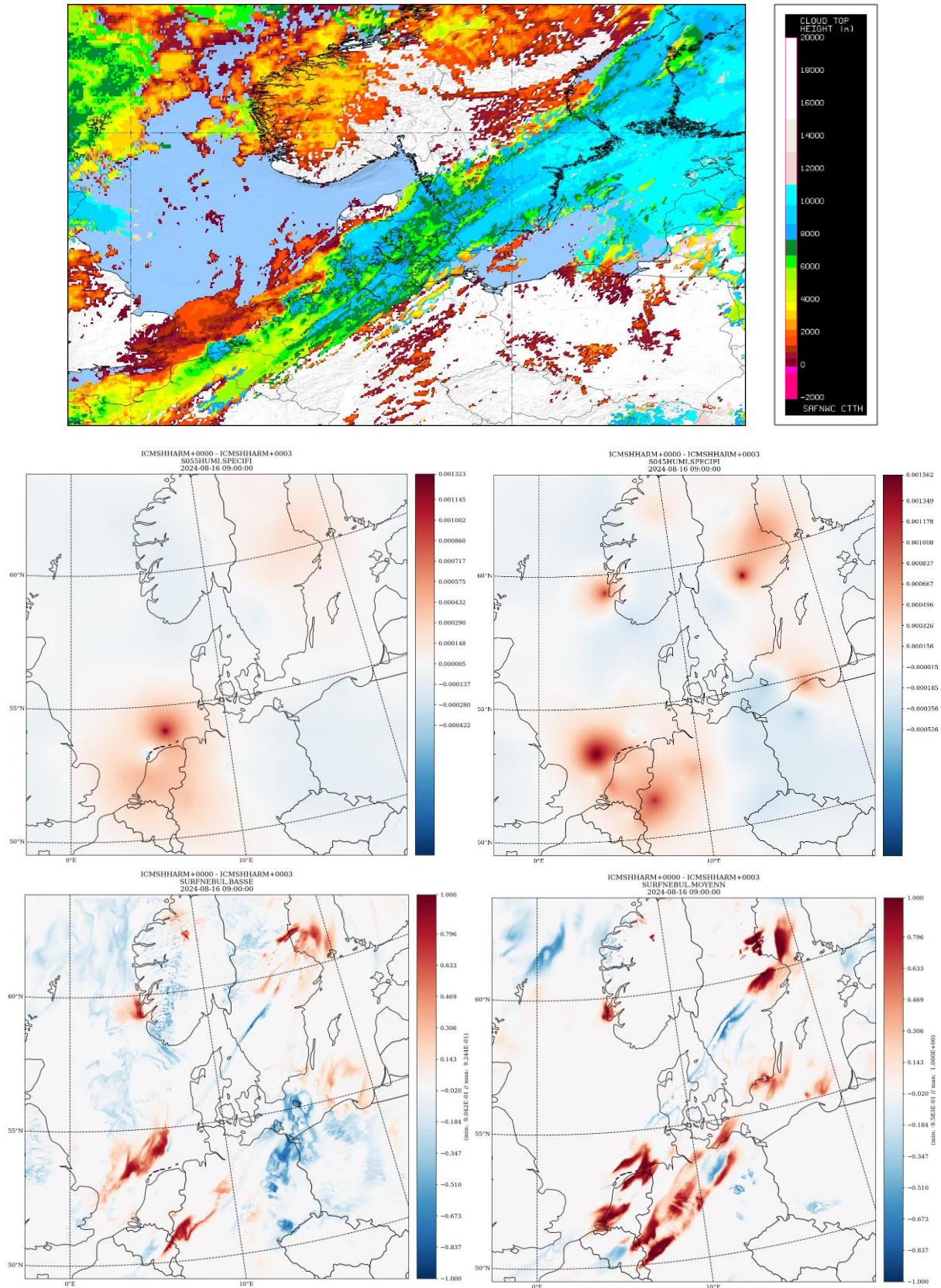


Figure 3. Above: NWCSAF+ECMWF-IFS cloud top height picture. Middle: analysis minus first guess specific humidity increments at level 55 (on the left) and level 45 (on the right). Down: analysis minus first guess low (on the left) and middle (on the right) cloud fraction increments.

Some examples of first guess versus analysis relative humidity profiles are presented below in the Figures 4-6. Figure 4 shows the profiles at sites, where single-layer cloud observation was passed to the system. In this case RH is pushed towards the saturation inside the cloud. Figure 5 shows the profiles at coordinates, where no clouds were observed. Then, RH is penalised to stay under saturation level. Figure 6 shows the profiles in the places, where several cloud bases were detected by ceilometer. In these cases, the system got the information about the thickness of the layer between the cloud top and the highest cloud base, while the lower bases were reported alone, with no thickness information. We see that in case of several cloud bases, the results do not look good enough.

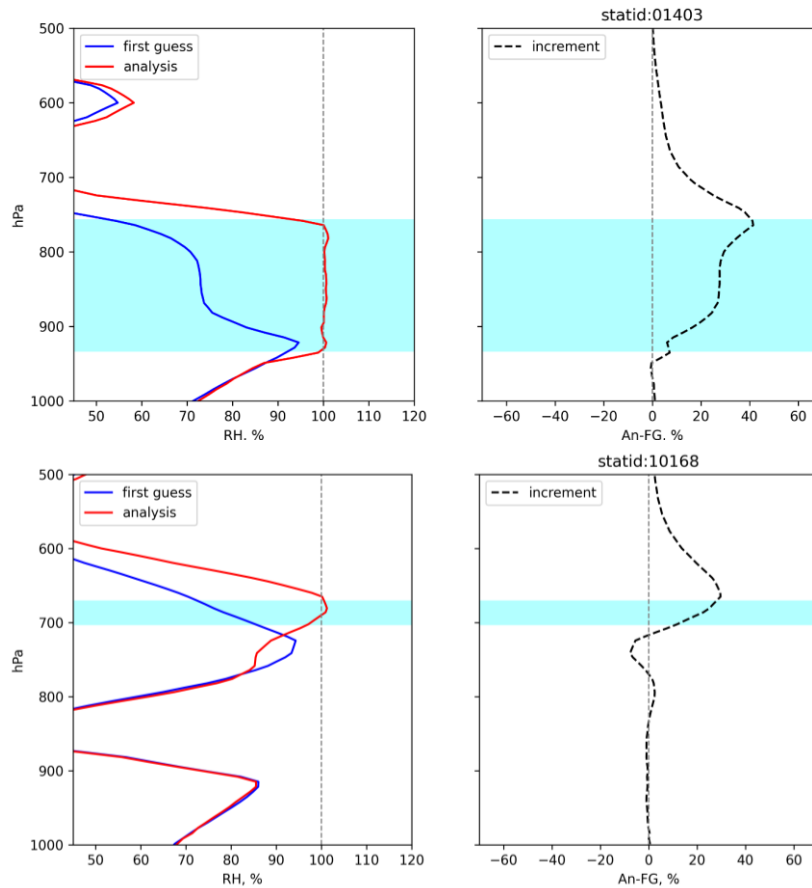


Figure 4. First guess (blue line), analysis (red line) and analysis minus first guess increment (dashed line) profiles of the relative humidity at the sites, where single layer cloud was observed. The cyan rectangle shows the observed cloud layer.



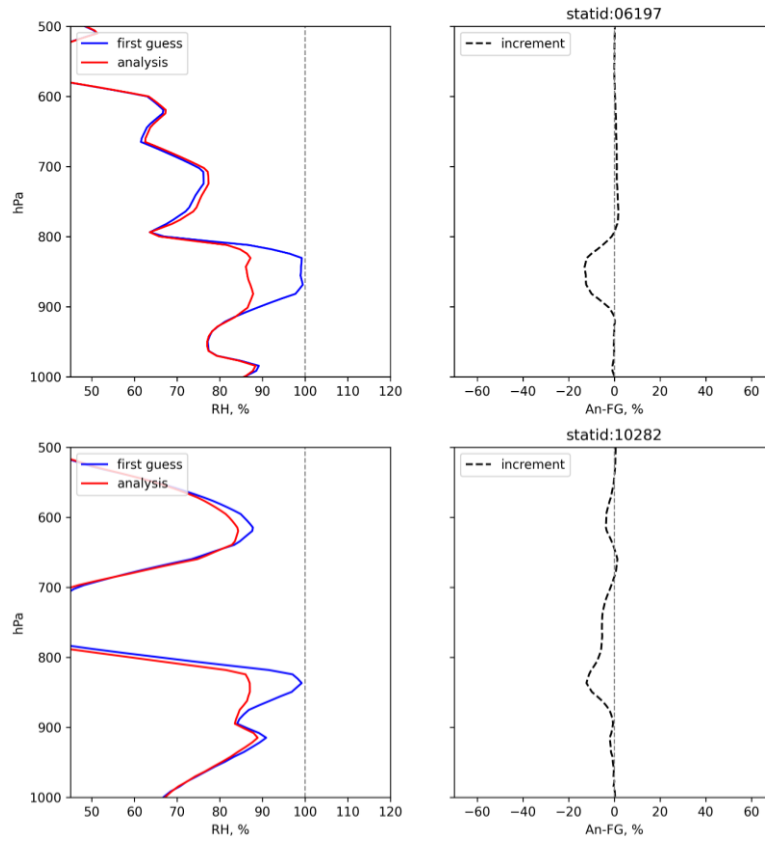


Figure 5. Analogous to Figure 4, but for the sites, where no clouds were observed.

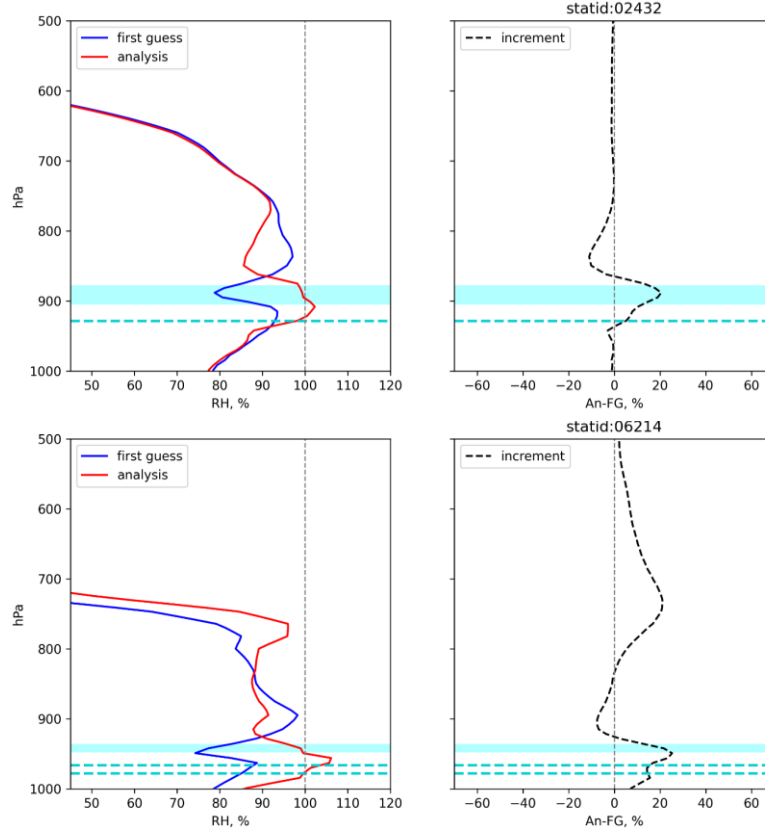


Figure 6. Analogous to Figures 4 and 5, but for the sites, where multiple cloud bases were observed. The cyan rectangle shows the cloud layer between upper cloud base and cloud top, dashed lines show the lower cloud bases.

We also checked, if the effect of cloud data assimilation still exists after 1, 2 and 3 hours of forecast. Figure 7 demonstrates the increments of low and middle cloud fraction between the forecast produced from DA cycle and the forecast produced in previous cycle: 1-hour forecast at 9 UTC minus 4-hour forecast at 6 UTC, 2-hour forecast at 9 UTC minus 5-hour forecast at 6 UTC, and 3-hour forecast at 9 UTC minus 6-hour forecast at 6 UTC. From these pictures we see, the cloud increments remain after several hours of forecast.

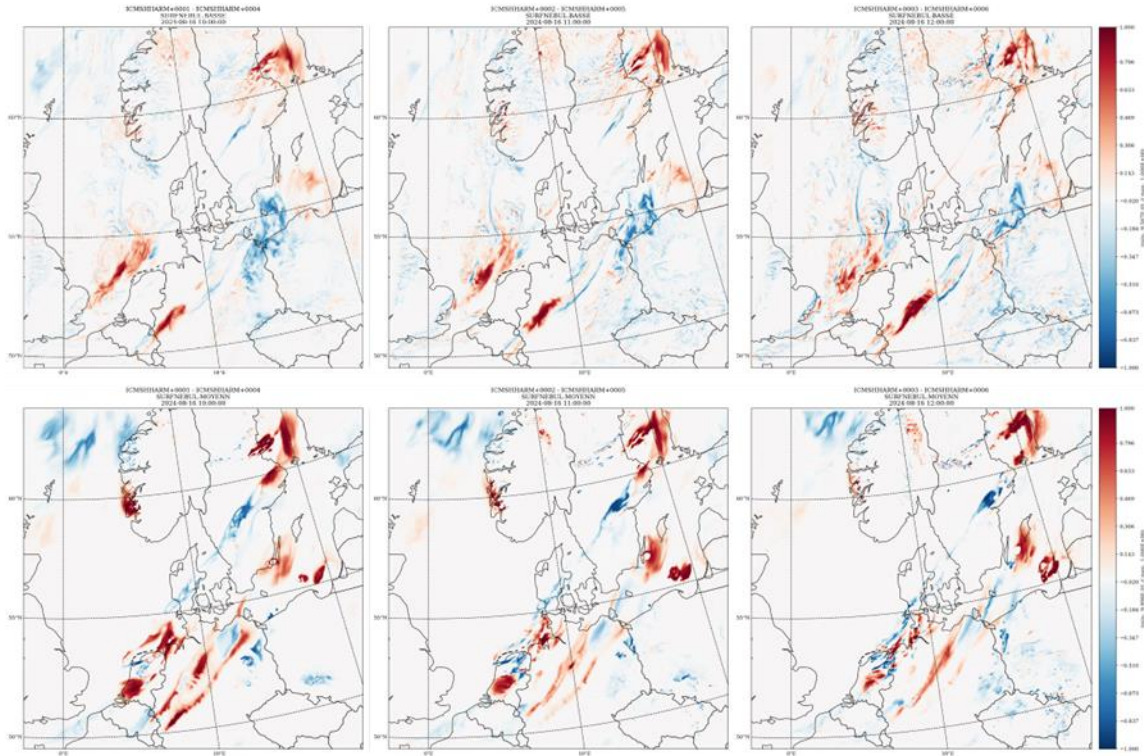


Figure 8. Increments of low (upper row) and middle (lower row) cloud fraction in 1-hour (left column), 2-hour (middle column), and 3-hour (right column) forecast.

## 4 Conclusions and foreseen next steps

The first experiment based on real observations demonstrates the scheme's ability to produce and remove the clouds through the manipulation of relative humidity profiles based on cloud layers locations. Moreover, the effect of assimilating the clouds is still present after 3-hour forecast. We will proceed with this study and point out some foreseen steps:

- Compute the observation error and scaling parameter for the cloud observations.
- Discuss more precisely the observations processing during the OBSOUL file creation.
- Run the model for the longer period, using the cloud observations along with the conventional observations + parallel suite without cloud observations. Do the verification.
- Do the setup in 4D-var or 3D-EnVar to see, if we could get rid of strong increments smoothing effect.

# Report on the TUNING AND DIAGNOSTICS Working Week

Oslo, Norway, 18-22 November, 2024

Jana Sanchez Arriola, Åsmund Bakketun, Per Dahlgren, Idir Dehmous, Stephanie Guedj,  
Magnus Lindskog, Benjamin Menetrier

## 1. Introduction

---

Jana Sanchez Arriola and Magnus Lindskog visited Stephanie Guedj, Benjamin Menetrier, Per Dahlgren, Åsmund Bakketun at Met to work with tuning and diagnostics. Initially it was planned that Idir Dehmous would also join Oslo. Due to administrative constraints Idir needed to join remotely.

The aim of the week was to extend some existing tuning softwares that were already working for conventional observations but that were not ready to be used with satellite data yet. So during the week the softwares has been adapted to most of the satellite data currently used by the models of ACCORD and then used to tune the cy46 Harmonie-AROME runs over Iberia, MetCoop, UWC-W and Arome Arctic domains.

## 2. Background errors in Observation Space (BGOS)

---

Benjamin prepared ACCORD OOPS code to use a fixed branch. This will make the BGOS developments more stable.

Adaptations of BGOS to satellite observations and understand large seasonal variation and spatial variation for MHS and not so large for AMSU-A. Now BGOS is working for all kinds of remote sensing and convention data as well from stored archived observation database (odb) files (BGOS\_only option).

BGOS was applied over AEMET and MetcOop domains during the visit. Figure 1 below shows currently used background and observation error standard deviations from AEMET domain and for AMSU-A and MHS instruments. Observation errors are static and dependent on instrument only. Background errors standard deviations in AMSU.A observation space (channel 6-9) are rather constant in between location and between season for AMSU-A but show a large seasonal dependence as well as flow dependence for MHS instrument (channel 3-5).

Comparison of same time different seasons (Summer and Winter)

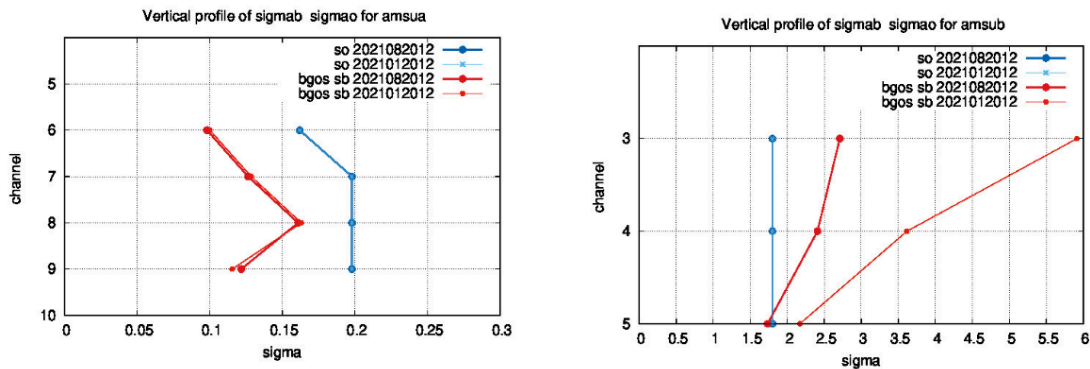


Figure 1. Observation error standard deviations (blue) and background error standard deviations red for AMSU-A instrument (left) and MHS instrument (right). Thin curves are for winter and thick curves are for summer.

The strong seasonal dependence for MHS is characterized by larger background errors in MHS observation space during winter and in areas of low humidity. An illustration of spatial variation is shown for one particular case in the case of background errors in MHS channel 3 observation space for 20230115 09 UTC over MetCoOp domain.

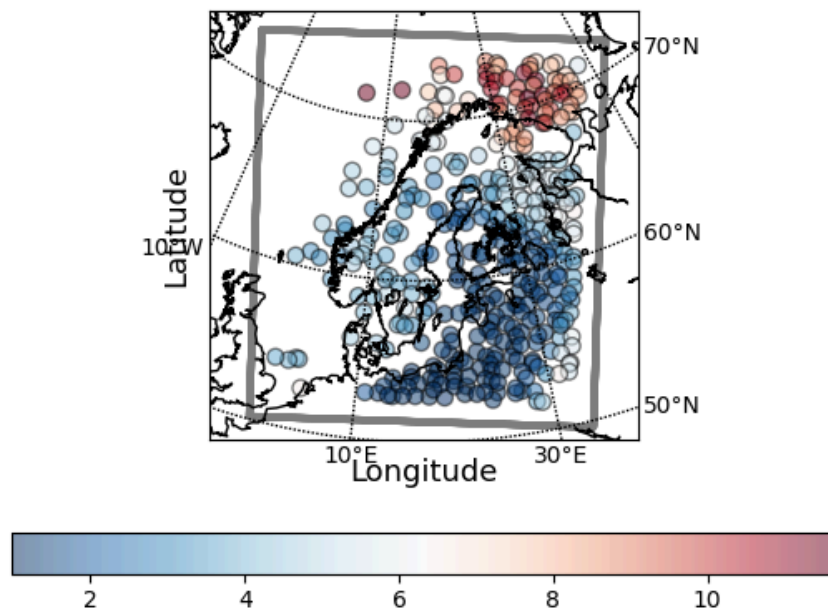
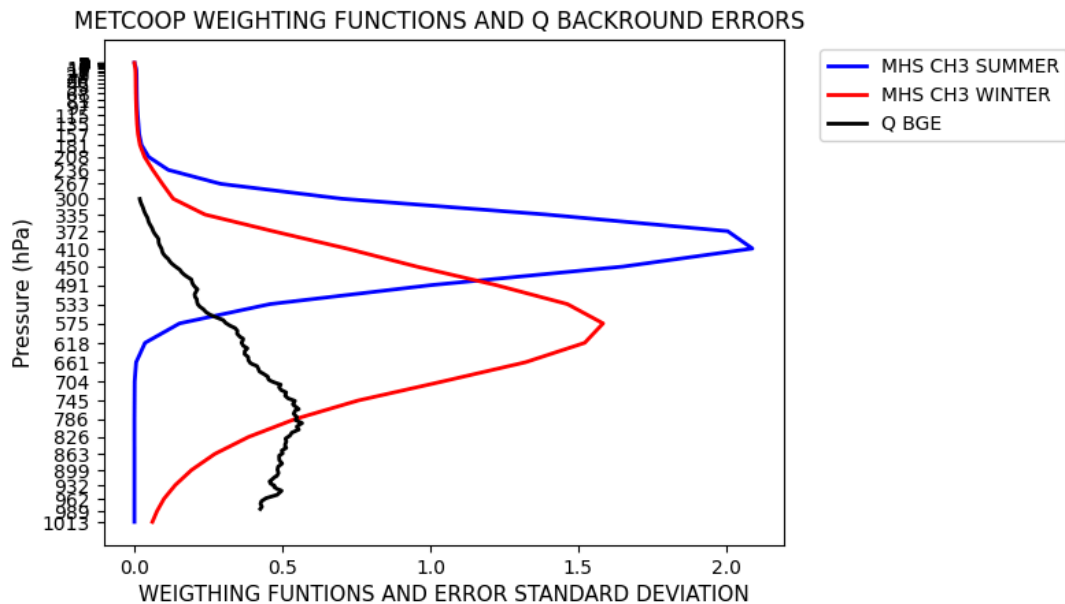


Figure 2. Background error standard deviations in MHS channel 3 observation space (unit K) for 20230115 09 UTC over MetCoOp domain.

The reason for the seasonal variation was investigated. It is quite independent of whether a nonlinear or a tangent linear observation operator is applied. The reason was found by applying a standalone RTTOV (version12) for winter and summer subarctic profiles and thereby investigating the response functions together with the static (in season) moisture background error standard deviation profiles applied in MetCoOp (Figure 3). This was done by Magnus and Per, which provided code and scripts

from his earlier studies for the Arctic Weather Satellite to derive and print weighting functions. It can be seen that during wintertime the weighting functions peak lower in the atmosphere and, since the background errors in MHS channel 3 space is approximately proportional to an integral of the background error standard deviation profile weighted by the weighting function, larger integrated values will result in winter when the weighting function peak lower (where seasonally independent static specific error background error standard deviations are larger).



*Figure 3: Illustration of MHS channel 3 weighting function and why it is largely dependent on summer/winter and also spatially dependent on background state. During low moisture (winter) channels peak lower in the atmosphere, where background errors are larger*

This seasonal variation leads to higher weight to the MHS observations in the data assimilation system during wintertime than during summertime. It is an artifact of the static moisture background error standard deviations. This static error also leads to more weight to radiosonde moisture observations during winter than during summer, due to temperature dependent observation error standard deviations with higher values during summer than during winter.

This artifact could be alleviated by introduction of seasonally dependent background error statistics. The ideal would be to use flow dependent background error statistics. To illustrate how introduction of seasonally dependent background error statistics would help background errors were calculated during this visit calculated specifically for summer and winter period specifically by Roohollah Azad and Ole Vignes and for the MetCoOp area. In operations an average of the two is used and both summer and winter ensemble files used for deriving these statistics were stored on discs. This made it relatively easy for Ole and Roohollah to rerun 'festat' program with summer and winter samples only, rather than combined. In future operations some could think to gradually shift between winter and summer ones, depending on season, like has been done in the CERRA reanalysis project for example (El-Said et al., 2022). Figure 4 is the same as Figure 1 but now also with specific humidity background error statistics also purely derived from summer and winter conditions included. Seasonally averaged, summer and winter profiles are all scaled with scaling REDNMC value 0.6.

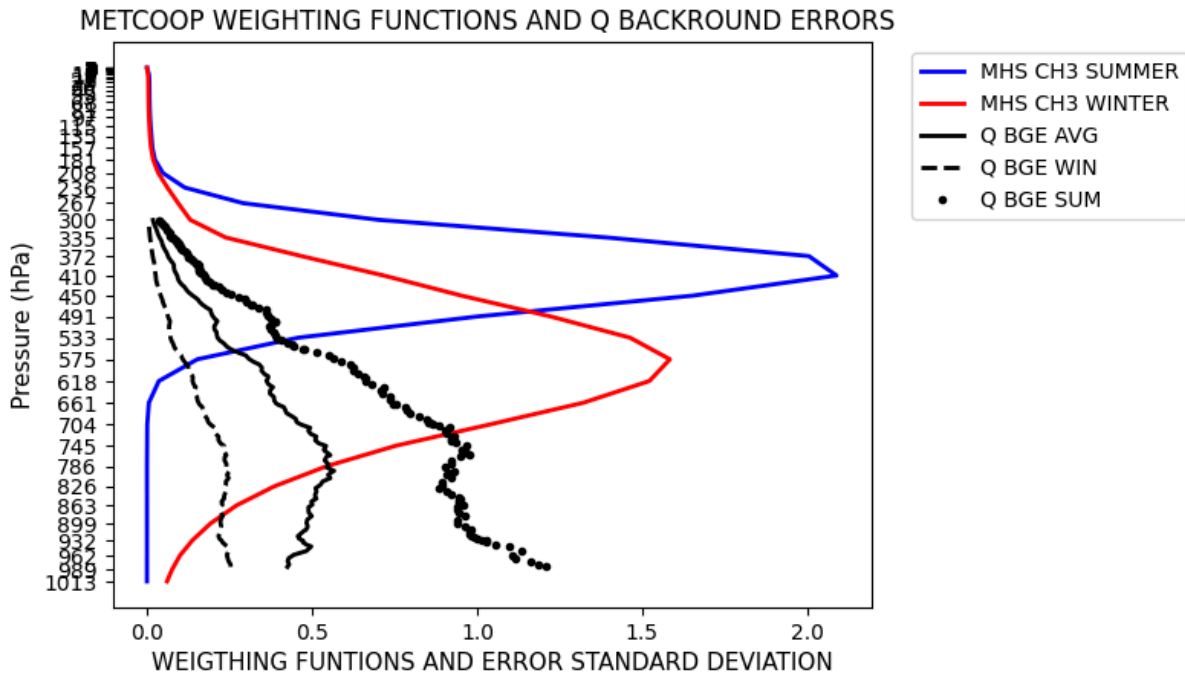


Figure 4: Illustration of MHS channel 3 weighting function and why it is largely dependent on summer/winter and also spatially dependent on background state when static errors are applied. With seasonally dependent background errors this is alleviated. Then the static background errors are larger during summer and smaller during winter, resulting in a smaller difference of background errors in MHS observation space between summer and winter.

In Figures 5 it is illustrated how artificial seasonal dependence of MHS ch 4-5 background errors in observation space seen when using static background error file (left) would change if seasonally dependent background errors were applied (right). It can be seen that with seasonally dependent background error files (stabal.cv and stabal.bal) the background errors in MHS observation space are even smaller during winter than during summer, which was not the case with static a B matrix.

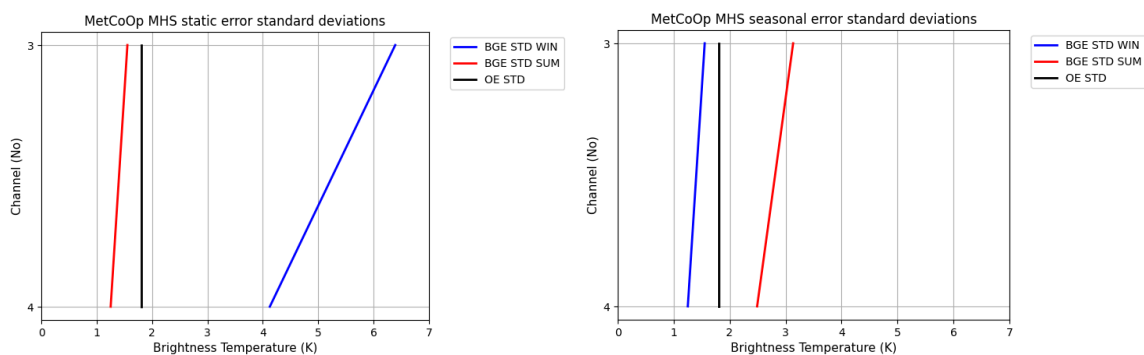


Figure 5. Background errors in MHS channel 3-4 observation space with standard operational MetCoOp B matrix (left) and when a seasonally dependent B matrix (right) was applied with summer errors for summer case and winter values for winter case. Black curve observation error; Blue winter background error in MHS ch 3-4 space and Red summer background error in MHS ch 3 space. Winter case 20230115 12 UTC and summer case 20220715 12 UTC.

### 3. Desroziers method to diagnose the observation and background errors

#### 1. General

This software was just prepared to calculate the diagnosed observation error standard deviations ( $\sigma_o$ ) and background error standard deviations ( $\sigma_b$ ) with Desroziers method and make plots for these values and the currently used  $\sigma_o$  and  $\sigma_b$  values. This was done for conventional observations by plotting a vertical value against the pressure. The  $\sigma_b$  values are obtained after running a BGOS experiment with the framework that has been prepared by Benjamin. In this working week Jana have extended this software to be able to get the observation and background error standard deviations from satellite: AMSU-A and MHS observations, and plot them for various channels of the instrument. These kinds of plots for currently used errors were shown in some of the plots in the previous section (Figure 1 for example). The extension to include as well Desroziers derived values is shown in sections below. In the coming weeks the software will be completed with more satellite sensors of the sensors and then it will be shared with the ACCORD community.

#### 2. Tuning of observation errors in Arome Arctic domain using the Desroziers diagnostics

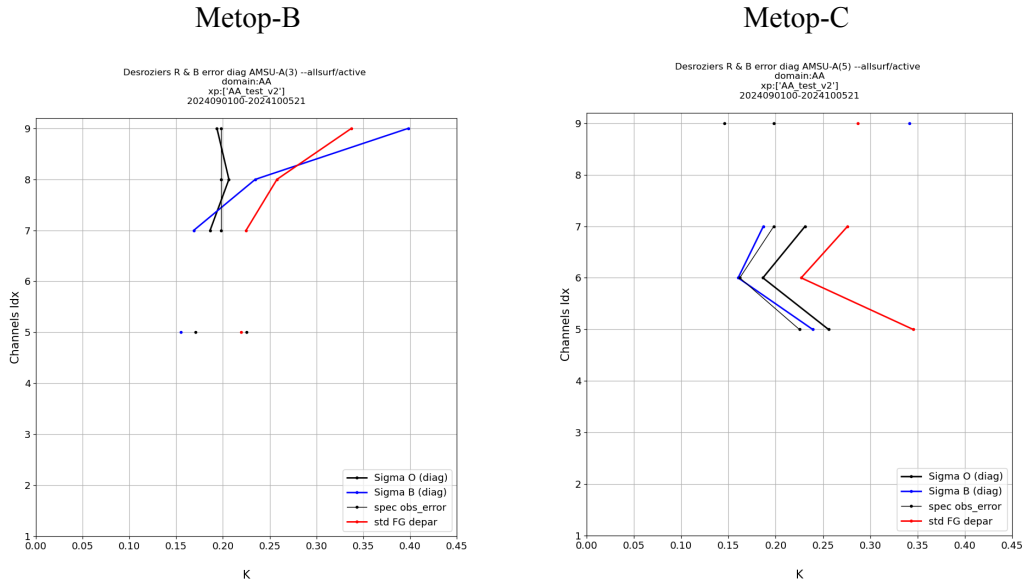
The Desroziers diagnostic has been used to tune the observation error in Arome Arctic (AA) for all available satellite instruments (AMSU-A, MHS, CrIS, IASI, ATMS and MWHS-2). Figure 6 is showing an example for AMSU-A of diagnosed sigma O and sigma B, together with the FGdepar (first guess departure) standard deviation obtained before and after tuning. Specified sigma O (ROERR\_RAD1C) has been increased by about 0.4K for channel 5 and 0.1K for other channels. Table 1 is summarizing the changes affecting the main harmonie\_namelist for all instruments. A further extension would be to extend the diagnosis to include also currently background errors in observation space for the various satellite instruments and to compare with results to be obtained for other domains (see section 2.2).

Table 1: Namelist updates of specified observation errors in Arome Arctic.

```
NAMCOSJO=>{
'ROERR_RAD1C (3,5)' => '0.44',
'ROERR_RAD1C (3,6)' => '0.275',
'ROERR_RAD1C (3,7)' => '0.33',
'ROERR_RAD1C (3,8)' => '0.33',
'ROERR_RAD1C (3,9)' => '0.495',
```

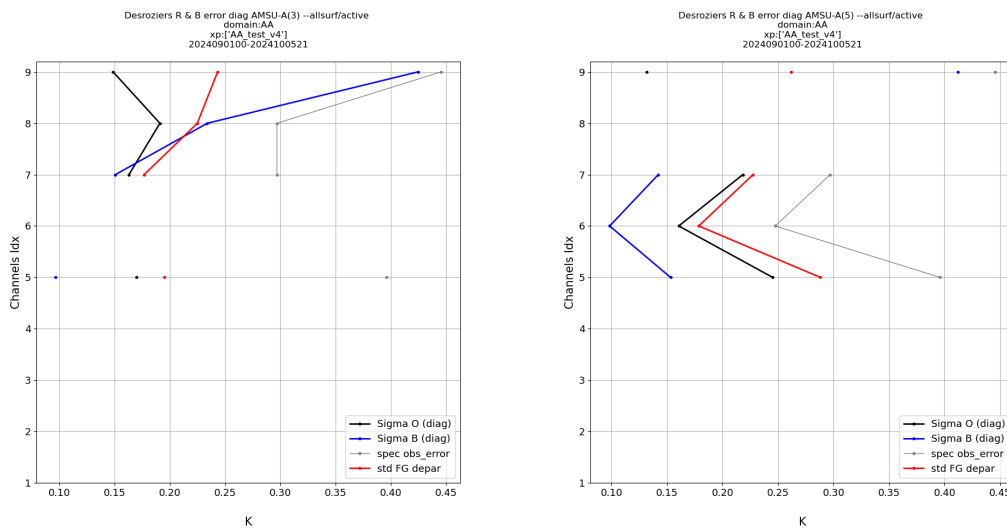


**before tuning**



```
ROERR_RAD1C(INST_ID_AMSUA,1:15)=(/30.0_JPRB,30.0_JPRB,30.0_JPRB,30.0_JPRB,0.25_JPRB,0.18_JPRB,
0.22_JPRB,0.22_JPRB,0.22_JPRB,0.26_JPRB,0.30_JPRB,0.44_JPRB,0.66_JPRB,1.40_JPRB,30.0_JPRB /)
```

**after tuning**



```
ROERR_RAD1C(INST_ID_AMSUA,1:15)=(/30.0_JPRB,30.0_JPRB,30.0_JPRB,30.0_JPRB,0.44_JPRB,0.275_JPRB,
0.33_JPRB,0.33_JPRB,0.495_JPRB,0.26_JPRB,0.30_JPRB,0.44_JPRB,0.66_JPRB,1.40_JPRB,30.0_JPRB /)
```

*Figure 6. Arome Arctic by Desroziers method derived error characteristics for AMSU-A as well as by that time currently used observation errors and also first guess departures (for channel 5-9).*

### 3. Tuning of observation errors for Iberian Peninsula, MetCop and UWC-W domains using the Desroziers diagnostics

Some statistics for the Iberian Peninsula and Metcoop (and later UWC-W) domains for both summer and winter periods have been done and added to the plots for conventional observations in order to complete the current Diagnostics paper that are being prepared with the aim to be published in

ACCORD newsletter in the first part of next year. Figure 7 is an Example of such plots for AMSU-A and MHS for Iberian domain and for winter and summer seasons.

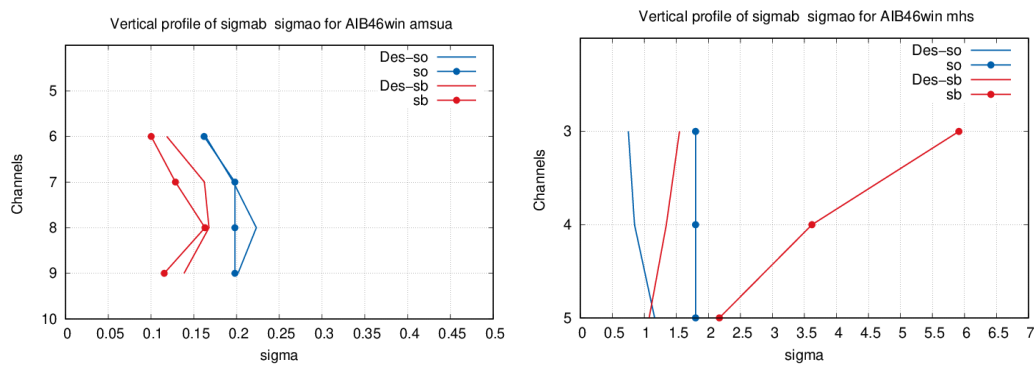


Figure 7:  $\sigma$  (blue lines) and  $\sigma_b$  (red lines) values used (line with points) and calculated by Desroziers method (lines) for AMSUA (left) and MHS (right) for the Iberian Peninsula domain and the winter period.

## 4. OBSTOOL software to see thinning distances

### 1. General

This software is to see the correlation and covariances of the observations and make plots with them, but it was just prepared to be used with the conventional observations and few satellites. During this WW Jana with the help of Stephanie has adapted it to all satellites and sensors assimilated in HARMONIE-AROME: amsua, mhs, iasi, mwsh2, atms, cris, and sevir.

Stephanie and Jana have been comparing plots produced from 3 experiments that Stephanie ran with different values of thinning distances for all the satellite data assimilated to see if the plots were consistent (amsua, mhs, iasi, mwsh2, atms, cris).

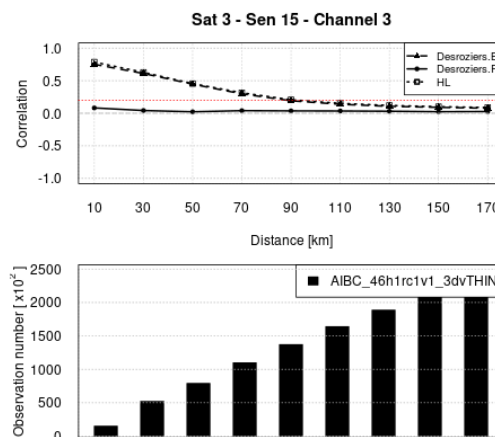


Figure 8. Spatial correlations of innovations, observation errors  $\mathbb{R}$ , background errors (B) for MHS channel 3 for one of the selected configurations.

Example of a plot made (still with R software) for the Iberian Peninsula is shown below as Figure 8, for mhs sat 3, channel 3. Several of these plots for various domains and derived with different

thinning distances applied in the data assimilation have been compared to check the sensitivity of results to domain and applied thinning distance. Ideally one would like to have less thinning when deriving the results, but then risk that the observation type studied get too much weight in the data assimilation and affect the separation in diagnostics between B and R part. Studies are still ongoing.

Idir has then translated part of the code to python and he has produced some first example plots and compared them with the ones we obtain by the current tool using R language. He will further clean the code and share it with all of us so we all can complete it introducing all the options we have in R to calculate and plot.

In order to test the new python version of Obstool ,only one observation type has been chosen (AIREP) for one cycle 20240105 at 00 UTC.

Hereafter , an example of observation correlation computed with Desroziers method and B, R (Desroziers ) and Hollingsworth/Lonnberg covariances

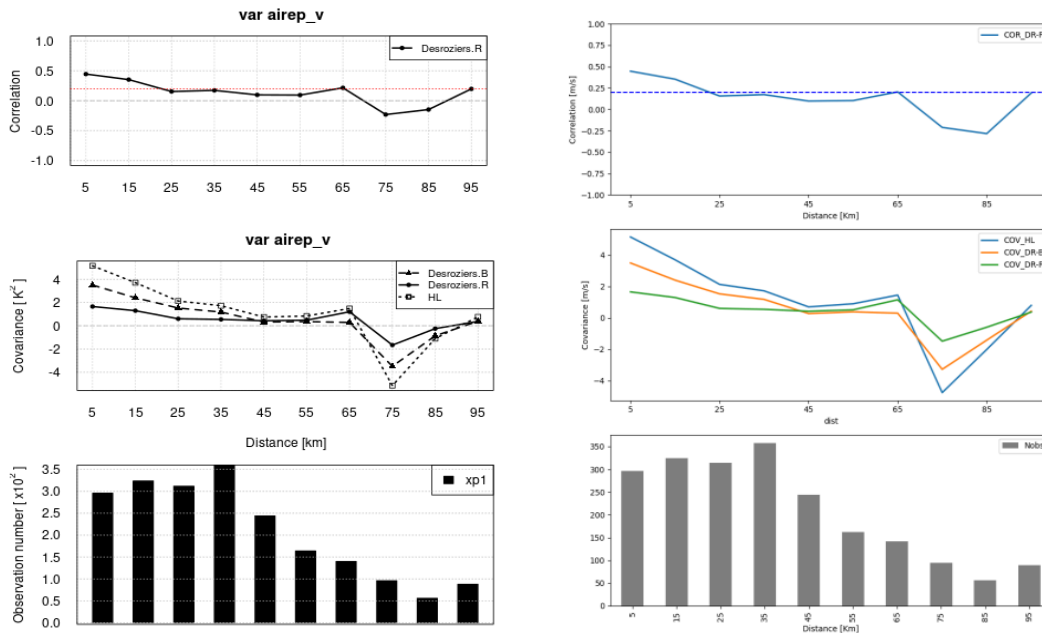


Figure 9. Spatial correlations of innovations, observation errors ( $R$  matrix), background errors ( $B$  matrix) for the  $V$  component of the AMDAR wind. Left panel is for the original R language version and the right panel for the Python version.

Idir has shared his version with other developers to get some input. New things is the Python language and also that reading is done from ODB1 directly instead of ascii files. The reading is a bit slow and Idir intends to optimise. One way to speed up is to use dcagen property. Idir also cleaned a bit in extraction of variables that are not needed for the diagnostics. Per pointed out that one can consider to use odb2, that has a lot of advantages, given that HIRLAM and ACCORD support this direction of odb2 generation. Another generalisation would be to introduce the possibility to not plot the diagnostics satellite by satellite but for all satellites using one particular sensor to get a larger sample. As an example, create an AMSU-A plot based not only on METOP1 but on all METOPS and NOAA19 and NOAA18.

## 2. Tuning of thinning distances for satellite data for Iberian, MetCoop and UWC-W domains

The tuning for conventional data for these three domains have been finished. And after some improvements in the software, some plots have been done for amsua and mhs for all the domains and

seasons (winter and summer) , and more will be done for atms, and mwhs2 and some conclusions will be written in the ongoing correspondent report.

### 3. Thinning distances for satellite diagnostics tool

Stephanie and Benjamin have been working on analysis of horizontal error correlations by Hollingsworth-Lonnberg and Desroziers method and to be implemented in a satellite diagnostics tool that they are implementing. The procedure and developments will be coordinated with Idir. Regarding the satellite diagnostics tool, see further details in section 4 below.

## 5. Satellite diagnostics tool

Åsmund and Stephanie are implementing a diagnostics tool mainly aimed for checking the performance and functionality of satellite data assimilation. Åsmund plans to extend as well to surface diagnostics. During the working week Benjamin started to take a look at how it can be optimally structured/designed. Also there was a discussion with Trygve Aspelien if/how it could be extended to possibly in future replace OBSMON. Magnus said that he will call for such design discussions of OBSMON. For now Stephanie and Åsmund would not like to do such generalisation. However it was found beneficial to put the tool on ACCORD Data assimilation Tool repository and share with others, despite still work in progress. Eoin Whelan was contacted to give agreement and permissions for such a procedure.

## 6. Interchannel correlation tool

A tool for deriving interchannel observation error correlations for various instruments was provided by Reima Eresmaa. We familiarized with it with the goal being a future implementation in the common ACCORD DA Tool box. An illustration is shown in the Figure below and it is only based on one single assimilation cycle and for IASI instrument channels, just to show that it is technically working. The tool can be applied to many different microwave and infrared instruments.

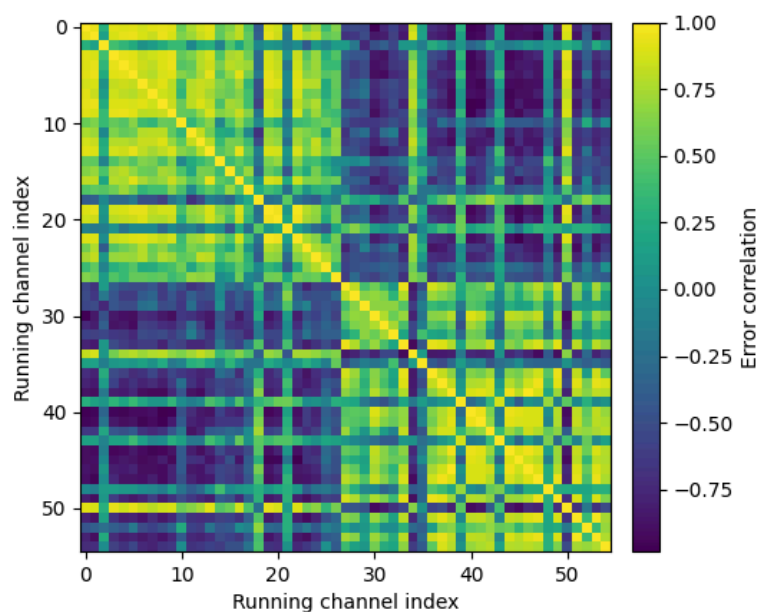


Figure 10. IASI interchannel observation error correlations based on one single case only.

## 7. ODB2 conversion tools and usage

---

Our NWP DA code uses ODB to store and access observation data. These files are designed for fast access in a HPC parallel environment and we are also using these ODB files to extract information for various DA diagnostics and monitoring. The ODB files, sometimes called ODB1 or native ODB, are tar files with directories and files in them. When the first Copernicus regional reanalysis systems were prepared it was a requirement to store the observation feedback in MARS at ECMWF and we were encouraged to convert the ODB files to a format called ODB2 which can be stored in MARS. It is also more flexible and effective to extract information from the ODB2 files.

A set of tools were developed for the regional reanalysis systems (CARRA and CERRA) which use an odb\_api installation with the tool odb\_migrator included. On ATOS you can load such an odb\_api installation by issuing the following commands:

```
module use /perm/hlam/apps/modulefiles/lmod
module load odb_api
```

To extract information from ODB one use SQL queries that can look like this:

```
odbsql -q "SELECT obstype,codetype,statid,obsvalue FROM hdr,body" -i
odbvar/ECMA.conv/ECMA.sch
```

This will dump the information to STDOUT. By adding the options “-o <filename> -f newodb” the output of the SQL query will be converted to ODB2 format and written to file.

The ODB2 file name conventions are that files with the ECMA information have suffix ofb and files with the CCMA information have suffix mfb:

```
<file>.mfb=odb_ccma
<file>.ofb=odbvar
```

Eoin Whelan has prepared a module on ATOS with the conversion tools:

```
module load odbcon/0.2.1
```

and Per has set up an experiment in which conversion to ODB2 is done in the model suite using Eoin's module. This experiment can be found here:

```
/home/fasg/hm_home/cy46_odb2con_showcase
```

In this working week Per also showed Magnus a script where the conversion is made offline, i.e. if you have already made an experiment then the ODB files have to be extracted from ECFS and converted to ODB2.

Per also made a demonstration of how to extract information from ODB2 using command line tools. Some points to be made is:

1: ODB2 files can be concatenated. In the example Per had all MW mfb files for one month concatenated into one file. An SQL command like this will then give a time-series of STDEV(O-B) and STDEV(O-A) for AMSU-A channel 7:

```
odc sql -q "SELECT andate,antime,STDEV(fg_depar),STDEV(an_Depar) WHERE sensor=3 AND
vertco_reference_1=7" -i atovs_tot.mfb
```

## 8. Summary

---

The working week was found by the participants very useful and resulted in significant progress and coordination in the field of diagnostics and tuning. It was very useful to be at MET in Norway and involve as well for shorter time participants not directly involved in the working week for discussions and assistance. Such persons involved include Roger Randriamampianina, Ole Vignes, Roohollah

Azad, Trygve Aspelien, Inger-lise Frogner. The cooperation with Idir remotely worked smoothly through dedicated daily online coordination meetings.

We acknowledge ACCORD for the financial support. The guests also acknowledged MET Norway for their hospitality having in mind nice restaurant lunches, Stephanie and Benjamin for ice-breaker organisation and Stephanie's preparations of evening dinner events with staff as well as winter-sauna and Oslo fjord trip and hiking events. Some parts of the work were not finalised but will be continued during the remaining part of the year.



*Figure 11. Five of working weeks participants during Oslo fjord tour event .*



*Figure 12. Two additional working week participants.*

## 9. References

---

El-Said, A., Brousseau, P., Ridal, M. & Randriamampianina, R. (2022). Towards Full Flow-Dependence: New Temporally Varying EDA Quotient Functionality to Estimate Background Errors in CERRA. *Journal of Advances in Modeling Earth Systems*, 14(2), Article ID e2021MS002637.



# Scientific visit on spatial methods with `harp` and `panelification` for `harp`

Polly Schmederer (GeoSphere Austria)  
 Carlos Peralta (DMI)  
 Fabrizio Baordo (DMI)

August 2024

## 1 Introduction

As part of the ACCORD visiting scientist (VS) program, Polly Schmederer from GeoSphere Austria visited DMI headquarters in Copenhagen in June 2024, with Fabrizio Baordo and Carlos Peralta being the hosts of the stay on DMI side. The VS stay was realised in accordance to the MQA working packages. The 4 weeks stay was used to implement the `panelification` tool [6] developed at GeoSphere in `harp` and to include additional scores and parameters to `harpSpatial`. Additionally, the benefit of using the `reticulate` package [1] was also explored. `reticulate` provides an interface between R, on which `harp` is built on, and the python language.

The software developments are shared in a github repository that includes installation instructions, example scripts and data sets [7]. Details on methods, developments, and data are presented below, along with application examples and future work.

## 2 Methods and software used

The `harp` package is a framework for NWP analysis, verification and visualisation of meteorological data developed by Andrew Singleton (Met Norway) and Alex Decknym (RMS) [8]. It is the official model verification tool within the ACCORD consortium. The `panelification` tool is a visualisation framework developed at GeoSphere Austria in order to give a quick summarising overview of the relative performance of several models derieved from their spatial verification scores and a couple of basic scores. `panelification` for `harp` is built on the `harpSpatial` part of the `harp` package [6]. Besides making the `panelification` tool in `harp` available, the VS stay was used to include new parameters (e.g. IR 10.8  $\mu\text{m}$ ) on which the `panelification` for `harp` tool is applied and to include the `reticulate` package in the `harp` process chain. `reticulate` provides an interface between R, the language in which `harp` is written, and the Python language. This allowed us to easily include some of the vast functionalities available in Python, for example through the library `xarray`. Being called from within the `harp` framework via `reticulate`, the reading and regridding of the input data from satellite in native format (`nat`) onto a regular grid happened in Python. Similarly, reading model data from different sources in `grib` and `netcdf` format was easily done with Python. Then, the data was returned to `harp` and converted to the expected format.

All the developments were carried out in a branch of the `oper-harp-verif` repository [3] and a pull request has been created and approved after the stay was finished. The package `renv` was used to create a local R environment where all the necessary libraries and dependencies can be installed and tracked.

### 3 Developments in panelification for harp and harpSpatial

---

The main developments achieved during the stay include:

- New functions to interface Python with R through the `reticulate` package.
- Including new parameters in `panelification` for `harp` .
- Including new scores in `harpSpatial` (e.g. FSS based on percentiles).
- Allow returning of fields in `harpSpatial` .
- Configuration files for each example presented in the repository, along with instructions on how to add new parameters.
- New functions to display the information in `panelification` for `harp` .
- Example scripts and data to test the application.
- Instruction on how to install the `harp` and `panelification` for `harp` packages along with all their dependencies using the `renv` (two options are given, but are only for the hpc cluster at ECMWF double checked ).

A comprehensive description of the developments and the functionalities can be found in the `README.md` file in the github repository [7].

### 4 Data used for spatial verification

---

As basis for the developments the following observation data was used in the examples provided in the repository.

1. Radar precipitation product from the DMI: Surface Quantitative Precipitation Estimation (SQPE) using both rain gauge and radar data.
2. EUMETSAT SEVIRI brightness temperatures [2]: High Rate SEVIRI Level 1.5 Image Data - MSG - 0 degree (native), e.g. MSG3-SEVI- MSG15-0100-NA-20240102235743.693000000Z-NA.nat
3. Cryo clim data

And the following model data was used.

1. Grib files output of the DEODE workflow running HARMONIE cy46h1 (total precipitation and FULL POS simulated radiances channels WV 062 and IR 08).
2. CARRA data from the Copernicus Data Service

A list of the different types of input data used in the examples can be found in table 1.

Table 1: Input data

Parameter	acc prec	brightness temperature	fraction of snow cover
Model	DINI, DEODE, IFS	DEODE	CARRA
Observation	DMI SQPE	SEVIRI (EUMETSAT)	Cryo Clim

## 5 Application examples

The evaluation using the panelification for harp visualisation displays the ranking of the models verified. The main table displays the ranking for all thresholds and windows sizes of the Fractional Skill Scores [5](FSS). FSS is a common spatial verification score used for total precipitation. Below some basic scores are displayed and highlighted according to the rank of the model. The background colour of the title summarises the ranking of the FSS scores and on the right the ranks of basic scores are summarised.

The figures show example outputs of panelification for harp . In Figure 1 the evaluation of two models over the Danish domain is shown using EUMETSAT SEVIRI and model data from the DEODE project [4]. Figure 2 displays an example for 3-hourly accumulated precipitation forecasts of three DEODE experiments verified against DMI's radar precipitation product SQPE also on the Danish domain. Figure 3 also displays an example plot over the Danish domain but uses data from the DINI model configuration of the Harmonie model [9] and the IFS model verified against DMI's radar precipitation product SQPE.

Note that all examples presented here are for illustrative purposes only and do not constitute a thorough evaluation of the models included.

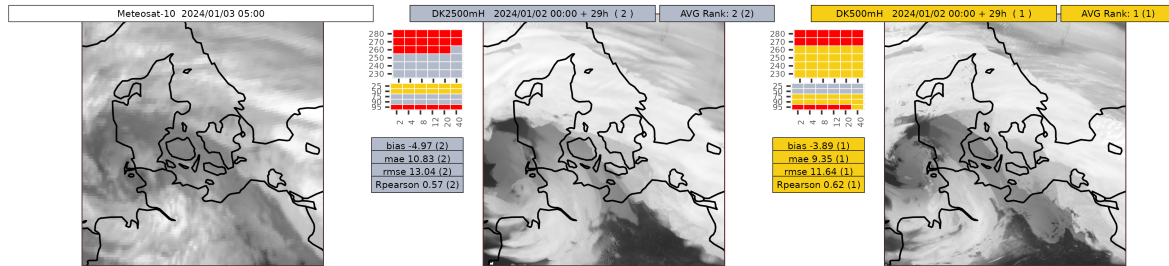


Figure 1: Example of FSS scores for a spatial verification of simulated brightness temperatures (at 2500m and 500m horizontal resolution) against the EUMETSAT SEVIRI observations (infrared channel 10.8 um).

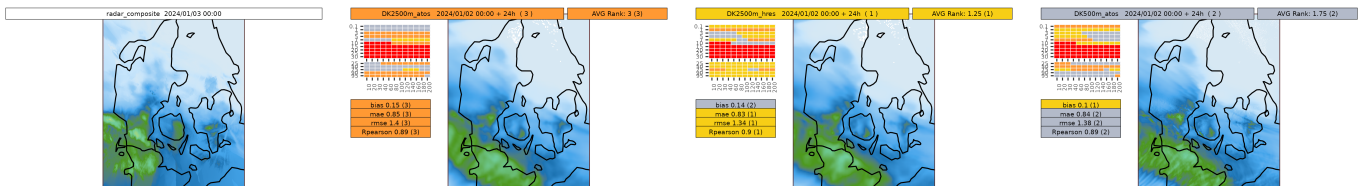


Figure 2: Example of FSS scores for a spatial verification of 3-hourly accumulated precipitation from two DEODE experiments (at 2500m and 500m horizontal resolution) against the DMI radar precipitation product SQPE.

The models are ranked according to their scores. The ranks of the models for each respective score are displayed in the plots on top of their respective forecast fields. The observations field is also plotted for comparison, allowing the viewer to understand the results better and to make their own judgment. The information on how to interpret a panelification for harp plot is listed in chapter 5.1.

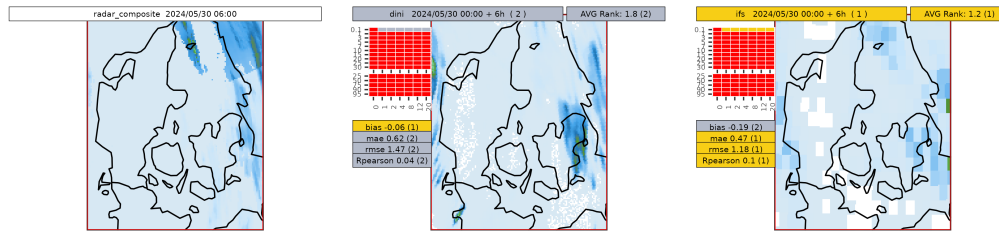


Figure 3: Example of FSS scores for a spatial verification of 3-hourly accumulated precipitation from the DINI and IFS models against the DMI radar precipitation product SQPE.

## 5.1 Information displayed on a panelification for harp plot

The first panel on the top left displays the observation field. Then there is one panel for each of the verified models. While the observation display follows the convention: name + valid observation time. The model display conventions are as follows:

model title:

- left: model name, initialisation time + lead time, (average FSS rank)
- right: average rank of basic scores (this is the average of all non-FSS scores that are passed in the definition file) and ranking of the models according to this average rank.

top box:

- ranks of FSS (using thresholds)
- ranks of FSS (using percentiles)

lower box:

- basic scores - displaying the actual values (rank according to the value)

The colour scheme of the ranks may be interpreted as follows:

- perfect scores (green)
- rank 1 (gold)
- rank 2 (silver)
- rank 3 (bronze)
- rank 4 and greater (white)
- no skill ( $< 0.5$ ) (red)
- NA (black)

When 2 or more models have the same rank, the next model with a higher rank will have a rank that is following up after the "missing" ranks. e.g. three models have rank 2.  $\rightarrow$  3 and 4 are the missing ranks and the next ranked model will have rank 5.

## 6 Future work

---

Further features are anticipated to improve the visibility and allow even better judgment of the performance and the inter-comparison of the models. Currently, `panelification` for `harp` includes only the Fraction Skill Score. Other spatial scores shall be assessed for their potential usage and to be incorporated in the near future.

The snow cover verification included in the examples of the repository cannot be displayed properly by the `panelification` for `harp` tool. This is due to the fact that the snow cover being processed is currently in a binary format (0 for no snow, 1 for snow) and the Fraction Skill Score display expects more than one threshold. This will be adapted in future versions.

## References

---

- [1] Reticulate package. <https://rstudio.github.io/reticulate/>.
- [2] EUMETSAT. Seviri data. <https://api.eumetsat.int/data/browse/collections>.
- [3] J. Fannon. `oper-harp-verif` scripts. <https://github.com/harphub/oper-harp-verif>.
- [4] DEODE project. Destination earth. <https://destination-earth.eu/>.
- [5] N. Roberts and H. Lean. Scale-selective verification of rainfall accumulations from high-resolution forecasts of convective events. *Mon. Wea. Rev.*, 136:78–97, 2008.
- [6] P. Scheffknecht. Panelification tool. <https://github.com/pscheffknecht-geosphere/panelification/tree/main>.
- [7] P. Schmederer, F. Baordo, and C. Peralta. Repository for the vs developments. [https://github.com/harphub/oper-harp-verif/tree/master/ACCORD\\_VS\\_202406](https://github.com/harphub/oper-harp-verif/tree/master/ACCORD_VS_202406).
- [8] A. Singleton and A. Decknyn. `harp`: a framework for meteorological data in r. <https://github.com/harphub/harp>.
- [9] United Weather Centers West. DINI configuration of the harmonie AROME model. [https://opendatadocs.dmi.govcloud.dk/Data/Forecast\\_Data\\_Weather\\_Model\\_HARMONIE\\_DINI\\_IG](https://opendatadocs.dmi.govcloud.dk/Data/Forecast_Data_Weather_Model_HARMONIE_DINI_IG).

# Evaluation of AROME-DUST-CY46 configuration over Southern Algeria

Ayoub Mehbali<sup>1</sup>, Mohamed Mokhtari<sup>1</sup>

<sup>(1)</sup>Numerical Weather Prediction Department, Office Nationale de la Météorologie, Algiers, ALGERIA

## 1 Introduction

The interest for studying desert dust lies in its significant effects on air quality, climate, and public health. Understanding and predicting dust events can help mitigate their adverse effects. However, modeling these phenomena presents challenges, including data scarcity and the complex interactions within the atmosphere.

Algeria is a vast country, with over 75% of its territory covered by desert. This makes us particularly vulnerable to sandstorms, which pose significant challenges for air safety by reducing visibility and disrupting flights.

The figure 1 illustrates the monthly distribution of dust phenomena occurrences over a 30-year period in southern Algeria. This analysis reveals a seasonal pattern in dust-related events, with notable peaks and lows across different types of dust phenomena. **Drifting sand** events, which dominate dust activity, reach their highest frequency in May with 479 days recorded, while December registers the lowest with only 169 days. **Sand haze** phenomena are most prevalent in August, with 257 days observed, and least frequent in December, with just 47 days. **Sandstorms**, although less common, show a peak occurrence in March with 30 days, whereas November and December record the lowest frequency at 2 days each.

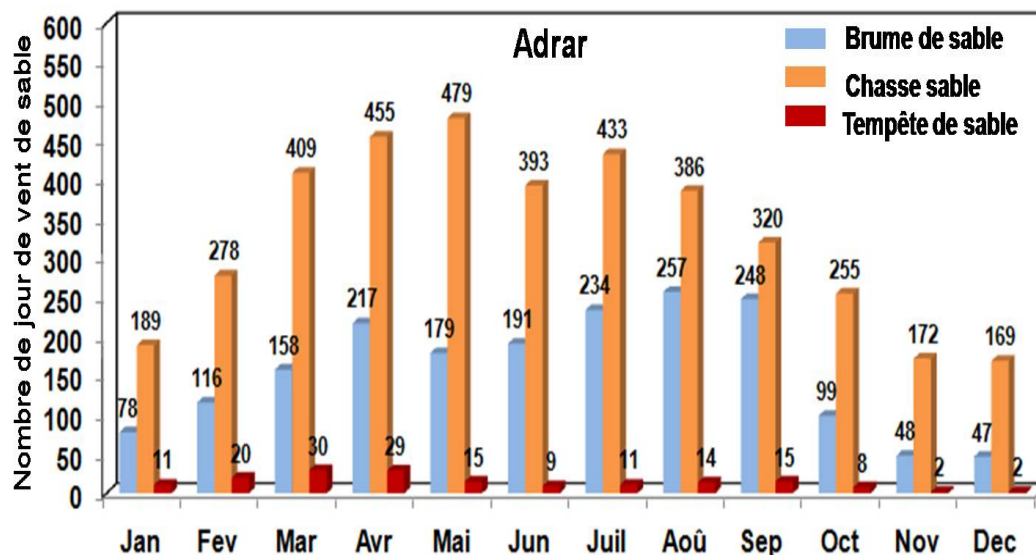


Figure 1: Monthly variation in the frequency of lithometeor occurrences by type for the Adrar station period 1984-2015. (Houari Benmoussa - DRM-SO Bechar)

### Overview of AROME/ALADIN Dust configurations:

The development of AROME and ALADIN dust configurations has evolved significantly over the years, starting in 2007, when the AROME\_DUST configuration was first employed in research and development settings (Kocha et al., 2011) [6]. Between 2008 and 2012, a comprehensive dust cycle was integrated into the ALADIN model, expanding its capabilities for dust forecasting (Mokhtari et al., 2012) [3]. In 2011, both AROME and ALADIN dust configurations were used operationally for the first time during the Fennec campaign in the Sahara, supporting flight operations by providing critical dust predictions (Chaboureau et al., 2016) [7]. By 2014, the ALADIN\_DUST configuration had become fully operational at the National Meteorological Office, marking a milestone in its implementation. Since 2016, a collaborative effort between ONM-Algeria and Météo-France has driven the ongoing development, maintenance, and updates of both ALADIN\_DUST and AROME-DUST configurations. Currently, the focus has shifted toward enhancing the AROME Dust framework, aiming to improve its accuracy, efficiency, and utility in dust forecasting across the region.

## 2 Algerian NWP current Dust system

### Operational Sand Forecasting Models at ONM

Since 2014, the National Meteorological Office has used the ALADIN Dust model, a limited-area version of the ARPEGE model, to simulate desert dust behavior. This spectral model operates within a defined region and shares coding and physical parameterizations with ARPEGE. Desert dust emissions are handled by the SURFEX module using the DEAD scheme (Zender et al., 2003) [8]. Within the atmosphere, the ALADIN/AROME model calculates optical properties, particle size distribution, as well as processes for dry deposition, turbulent fluxes, and wet deposition.

The Operational configuration of ALADIN DUST is shown at table 1.

Table 1: ALADIN DUST Operational configuration

Model	ALADIN DUST	
Horizontal resolution	14 x 14 km	
Vertical resolution	70 levels	
Grid points	250*250	
Initial conditions	ARPEGE	
Forecast range	72 h	
Time Step	420 s	
Area	Lat	18.5 – 46.5 N
	Lon	11 W – 17 E

### Feedback after 10 years of using Aladin\_Dust

After ten years of using the ALADIN\_Dust model, our forecasting team has consistently observed that the model tends to overestimate visibility in Tamanrasset, even during instances when dust phenomena are clearly present. This persistent discrepancy has raised concerns about the model's accuracy and its ability to reflect real atmospheric conditions in The Tamanrasset region.

To investigate this issue further, we decided to conduct a series of four sensitivity simulations using the AROME Dust model. Our goal is to determine whether the feedback provided by our meteorologists will yield similar results with AROME Dust as it has with ALADIN\_Dust.

When comparing the observed visibility values against the AROME\_Dust model predictions, the model consistently shows higher visibility (lower dust concentrations) in the Tamanrasset region, it indicates that the model fails to capture dust events originating from this area.



Dust emissions often depend on wind thresholds and soil properties. If Tamanrasset's local meteorological conditions and soil textures are not well represented, the model may not simulate dust emissions accurately.

The fact that AROME\_Dust doesn't identify Tamanrasset as a sand emission source highlights the need for further tuning and validation of the dust emission scheme.

In our analysis of AROME-DUST's performance over a span of four distinct days, each characterized by intense dust events with observed visibility falling below 2 km, we found consistent limitations in the model's ability to capture these dust conditions accurately.

The figure 2 illustrates the observed visibility versus model-predicted visibility over Tamanrasset, revealing a consistent gap where the model under-represents the dust concentration required to match observed conditions.

Across all four simulations, the AROME-DUST configuration failed to replicate the low-visibility conditions experienced in the region. Despite real-world observations indicating significantly reduced visibility due to dense dust, the model produced visibility estimates that were notably higher than the actual values, reflecting a substantial overestimation.

The objective of this study is to enhance the accuracy of the dust prediction model by implementing targeted modifications, specifically through adjustments to particle populations and constants that govern dust mobilization. These modifications aim to improve the model's ability to simulate visibility during dusty conditions more realistically.

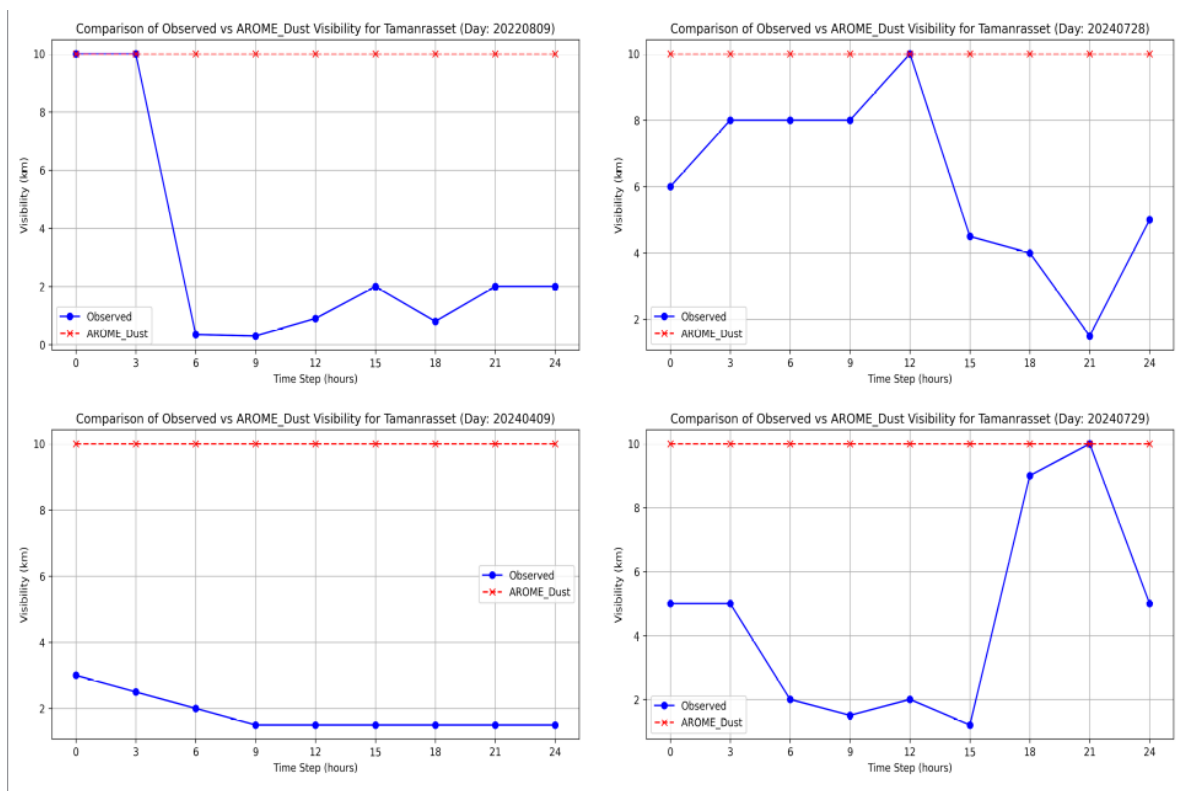


Figure 2: Observed visibility vs AROME\_Dust viability for Tamanrasset.

### 3 Modeling the Atmospheric Cycle of Desert Dust

#### Equation of the concentration

Three processes govern the life cycle of desert dust: the processes of lifting, transport, and deposition. The aerosol lifting process occurs in emitting areas when the frictional force of the wind acting on surface particles exceeds the forces that keep them grounded.

The transport of aerosols is primarily managed by wind speed and direction. These particles can traverse great distances over land surfaces and even over marine surfaces, reaching other regions.

The deposition process exists in two forms: dry deposition and wet deposition.

$$\frac{\partial C_k}{\partial t} = \underbrace{-u \frac{\partial C_k}{\partial x} - v \frac{\partial C_k}{\partial y}}_{\text{Horizontal advection}} - \underbrace{w \frac{\partial C_k}{\partial z}}_{\text{Vertical advection}} - \underbrace{\nabla(K_H \nabla C_k)}_{\text{Horizontal diffusion}} - \underbrace{\frac{\partial(K_Z \partial C_k / \partial z)}{\partial z}}_{\text{Vertical diffusion}} + \underbrace{\left(\frac{\partial C_k}{\partial t}\right)_{\text{source}}}_{\text{Source (emission)}} - \underbrace{\left(\frac{\partial C_k}{\partial t}\right)_{\text{puits}}}_{\text{Dry and wet deposition}}$$

Figure 3: Equation of the concentration.

In terms of environmental and meteorological impact, the rocky soil (cover005) type implies lower dust emission potential compared to smooth bare soils (cover004), as the rocky surface tends to reduce the availability of loose particles that could be lifted by wind. This characterization is crucial for dust modeling, as it can influence the accuracy of dust emission predictions, and might explain why dust concentration and visibility patterns differ in this region compared to others classified as smooth bare soils.

Figure 4 reveals that Tamanrasset is identified as a rocky soil zone according to the cover005 data, which indicates the presence of a significant rocky or stony surface in this region.

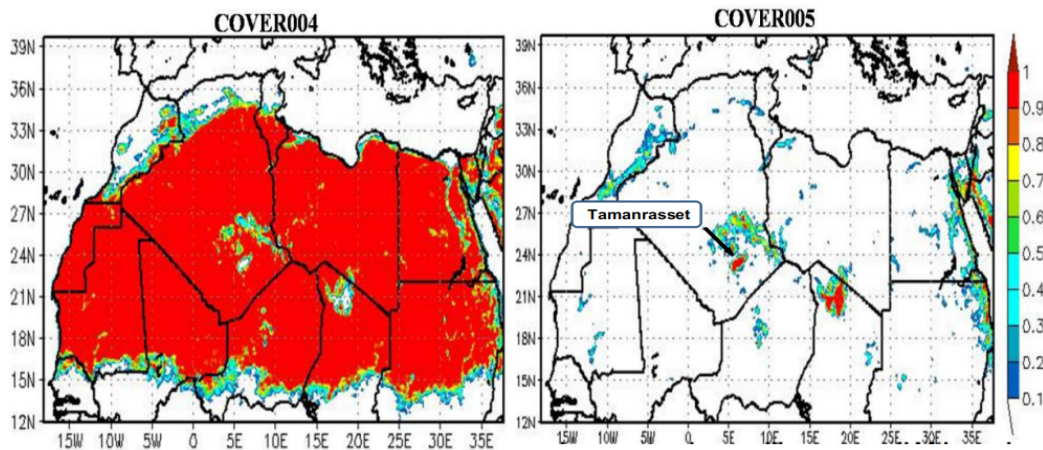


Figure 4: Maps of cover004 and cover005 related respectively to smooth bare soils (cover004) and rocky soils (cover005) over North Africa.

However, despite being surrounded by mountains, the Tamanrasset region contains significant dust deposition zones around these mountainous areas. These dust deposits can be reactivated by strong winds, making the area an active dust source during certain conditions. This discrepancy suggests that the model may underestimate the region's potential for dust emissions due to its rocky classification.

As for the total horizontal saltating mass flux  $G$  is calculated following MaB95 [5]:

$$G = a.E.c.\frac{\rho}{g}.u_*^3\left(1 + \frac{u_{*t}}{u_*}\right)\left(1 - \frac{u_{*t}^2}{u_*^2}\right)\int_{D_{bin}} dS_{rel}(D_{bin})dD_{bin}$$

Figure 5: The total horizontal saltating mass flux  $G$

As for the particles intensity factors ( $dS_{rel}$ ) they are represented in AROME\_DUST as shown in the table 2 :

Table 2: Default Particles intensity factors in AROME\_Dust

Default Particules intensity factors in AROME_Dust	
clay size $D_p < 2 \mu m$	0.005
small silt size $2 \mu m < D_p < 10 \mu m$	0.006
large silt size $10 \mu m < D_p < 60 \mu m$	0.1
sand size $D_p > 60 \mu m$	0.1

The relative surface area for each soil particle is based on a soil sample containing 1000 particles with diameters in the range of  $0.01 < D_p < 2000 \mu m$ . So, all soil particles that contribute to saltation and sandblasting processes are considered (Mokhtari et al. [3]).

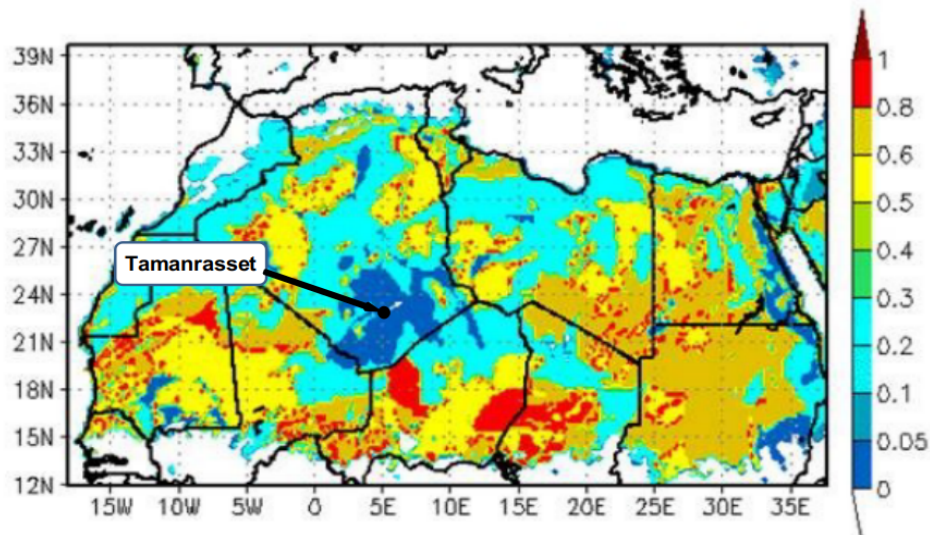


Figure 6: Total average relative surface for the four populations of particles over northern Africa (Mokhtari et al. [3])

## 4 Sensitivity Tests: The Tamanrasset Case

### Data Observation:

For this study, we focused on the dust event of July 29, 2024, which was characterized by intense dust uplift in southern Algeria, followed by transport towards the north and the Mediterranean. The resulting dust fields were compared with observational data. With a maximum AOD value reaching nearly 5. Visibility measurements during this period showed significant degradation, with Bechar reporting 4 km, Adrar 1 km, and Tamanrasset initially at 2 km, which later decreased to 1.2 km (Figure 7).

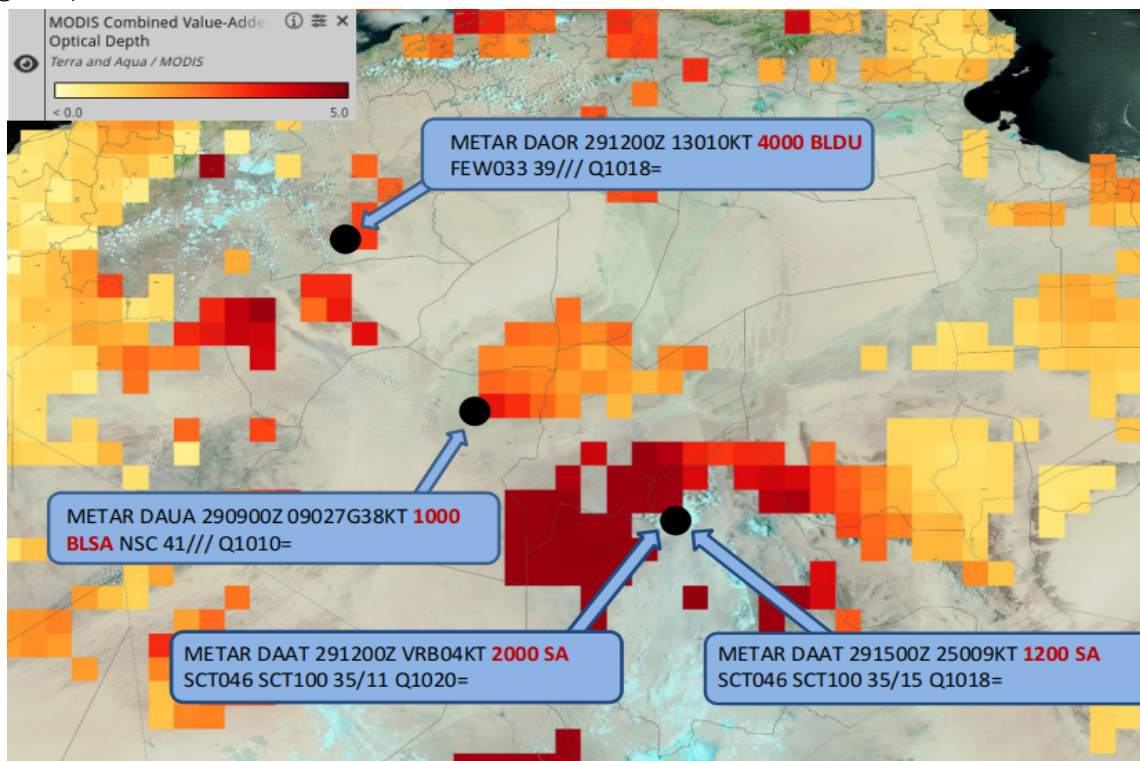


Figure 7: Satellite imagery MODIS/AQUA on July 29th, 2024 at 12h45 utc

### Simulations:

As shown in table 3 we performed four distinct sensitivity tests by varying the particles intensity factors randomly, as shown in the table. By altering these factors, we were able to observe how each test influenced the model's accuracy in predicting dust concentration/visibility.

Table 3: Modifications made in AROME\_DUST

Exp	Mod	Mod2	Mod3	Mod4
Particles intensity factors	Clay size	1	0.5	0.5
	Small silt size	1	0.6	0.5
	Large silt size	1	0.1	0.5
	Sand size	1	0.105	0.5



## 5 Results

### Dust concentration :

Particles factors directly influence how dust plumes are simulated in terms of their vertical distribution in the atmosphere, their lifetime, and their impact on regional and global climate systems.

The figure compares the dust concentration predicted by three configurations of the AROME\_Dust model: Default, **Mod**, and **Mod2**. The analysis shows that the **Mod** and **Mod2** configurations successfully predicted dust events in Tamanrasset. This improvement is due to increased percentages of finer particles (clay and silt) in the modified configurations, allowing the model to recognize dust potential even in rocky areas. Additionally, the regions surrounding Tamanrasset were also affected by these modifications, showing increased dust concentration. The **Mod** configuration had the highest dust intensity, while **Mod2** showed slightly reduced but still effective dust predictions.

the **Mod3** and **Mod4** configurations successfully predicted dust events in Tamanrasset but in term of intensity it's lower than **Mod** and **Mod2**. The **Mod** configuration had the highest dust intensity, while **Mod4** showed lower dust intensity but still effective dust predictions.

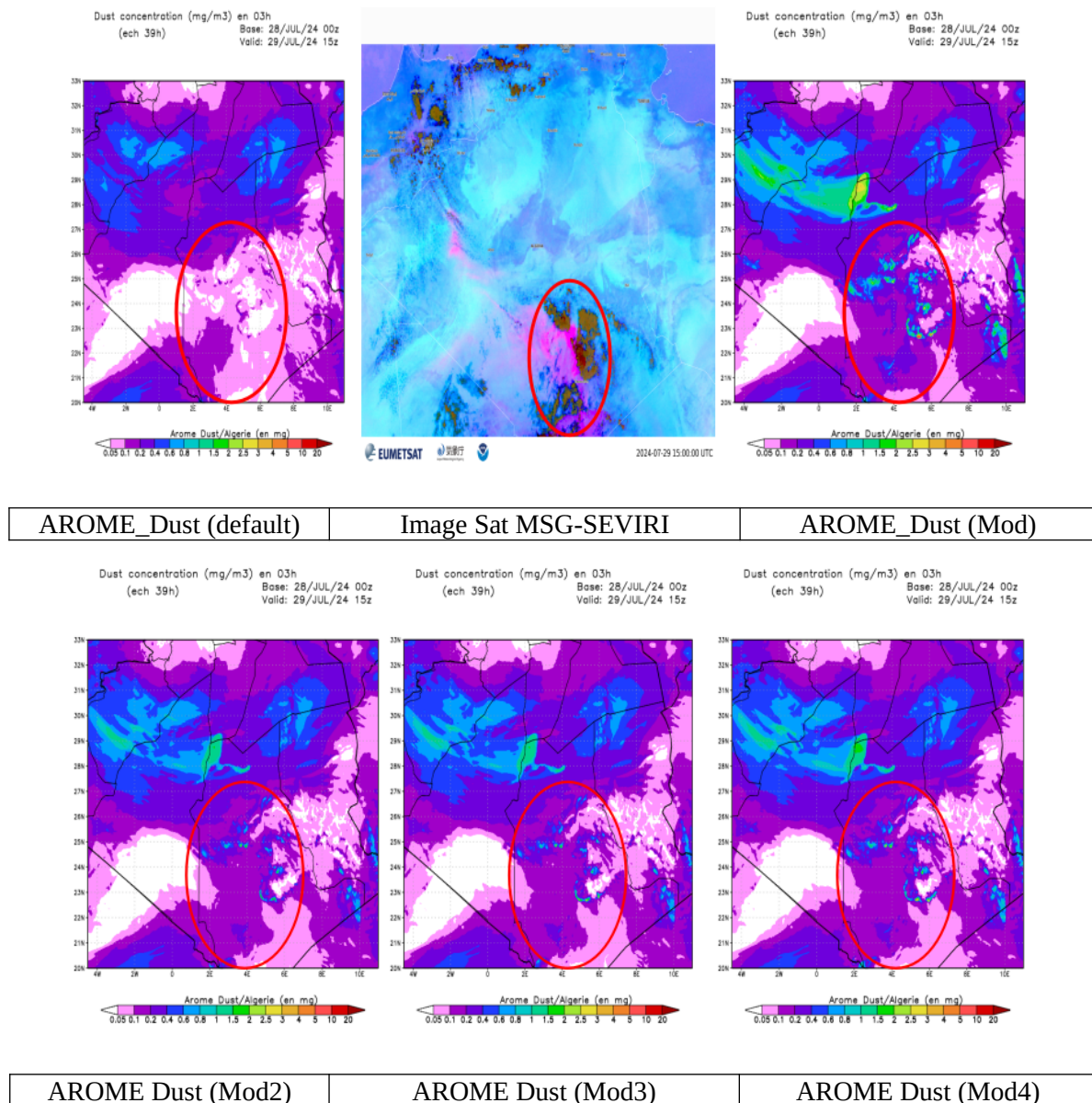


Figure 8: Dust concentration comparison for all Simulation

### Visibility :

The visibility comparison plot for Tamanrasset on July 29, 2024, reveals a substantial improvement in the accuracy of dust predictions following the modifications made to the AROME\_Dust model. The original Dust model, which was based on the standard configuration, consistently overestimated visibility even during periods of significant dust events. This overestimation was evident across the entire simulation, where the model failed to capture the observed fluctuations and variations in visibility caused by the dust.

In contrast, the modified models—**Mod**, **Mod2**, **Mod3**, and **Mod4**—showed a much closer alignment with the observed visibility data as shown in figure 9. These modifications allowed the model to better represent the real-time fluctuations in visibility as dust concentrations varied. For instance, during the dust event on July 29, the observed visibility was slightly below 2 km, with some variations observed throughout the day. While the **Mod** simulation slightly underestimated visibility during this period, both the **Mod2** and **Mod3** simulations showed a slight overestimation, which was still within reasonable bounds given the uncertainties inherent in the measurements.

The most significant finding is that the original Dust model, despite predicting visibility values in all cases, consistently overestimated visibility, even during peak dust events. This behavior suggests that the original configuration lacked the necessary sensitivity to accurately represent the impact of dust on visibility. On the other hand, the modified models, by incorporating targeted adjustments to dust mobilization parameters and particle population characteristics, were able to adapt more effectively to the dynamic nature of dust events, showing a marked improvement in sensitivity to variations in dust emissions and their effect on visibility.

These results underscore the effectiveness of the proposed model modifications in improving the representation of dust events in the AROME\_Dust model. The enhanced accuracy suggests that the adjustments made to the model help capture both the intensity and temporal variations of dust concentrations more realistically, thereby providing a more accurate prediction of visibility under dusty conditions. This improvement is crucial for better forecasting of visibility in regions affected by frequent dust events, leading to more reliable predictions for both meteorological monitoring and operational applications.

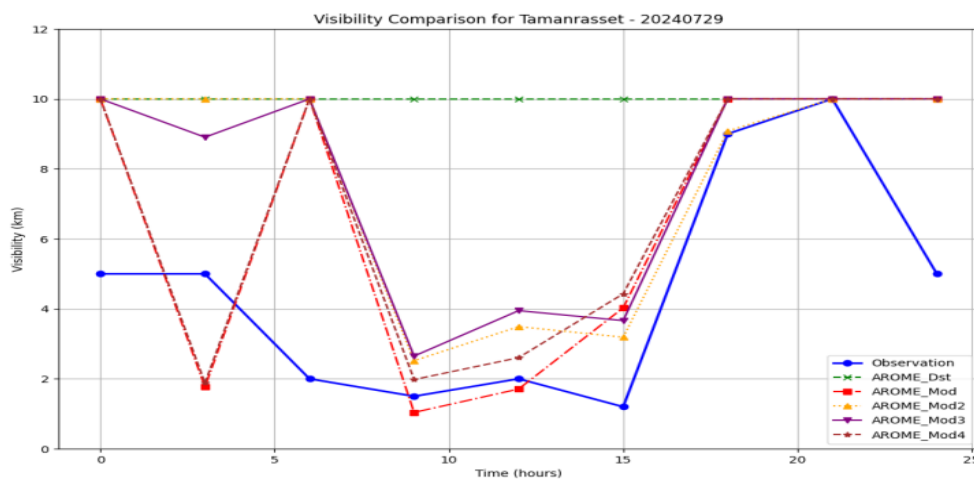


Figure 9: Comparison plot between observed and simulated visibility

## 6 Perspectives

### Future perspective :

In the current AROME\_Dust model, the **DEAD** scheme is executed for two land cover types: **Cover004** (bare soils) and **Cover005** (rocky soils). The process involves looping over each time step to calculate dust source intensity based on particle sizes and soil textures. This loop-based approach computes the dust mobilization repeatedly for each time step, making the process computationally intensive and memory-consuming, especially for large-scale simulations. However, the current loop-based methodology, while effective, results in a computationally intensive process. As the model must calculate dust source intensity for every time step, it demands substantial memory resources, particularly in large-scale simulations that cover extensive geographical areas. This repeated computation for each time step not only increases processing time but also poses challenges for memory management and optimization.

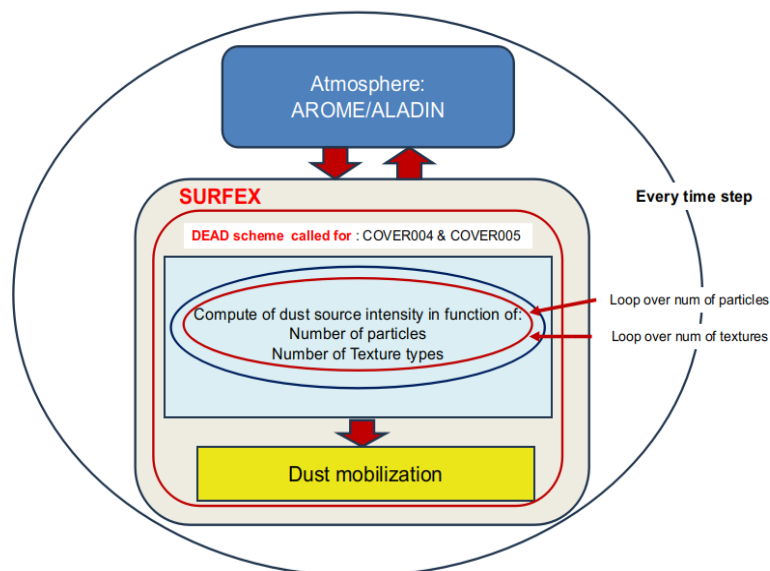


Figure 10: **DEAD** actual working processes

To enhance the model's efficiency, We propose introducing a new cover type, **COVERXXX**, to optimize the AROME\_Dust model. Instead of repeatedly calling the DEAD (Dust Entrainment And Deposition) scheme for bare (**Cover004**) and rocky soils (**Cover005**) at every time step, **COVERXXX** will handle dust source intensity based on detailed soil and surface characteristics, calculated just once. This change will significantly reduce computation time and memory usage,

enhancing the model's efficiency. Additionally, **COVERXXX** allows for more accurate dust emission predictions by incorporating finer soil properties, making the model more adaptable and precise for different dust-producing regions. This optimization balances high-resolution accuracy with improved performance, leading to faster and more reliable dust forecasts.



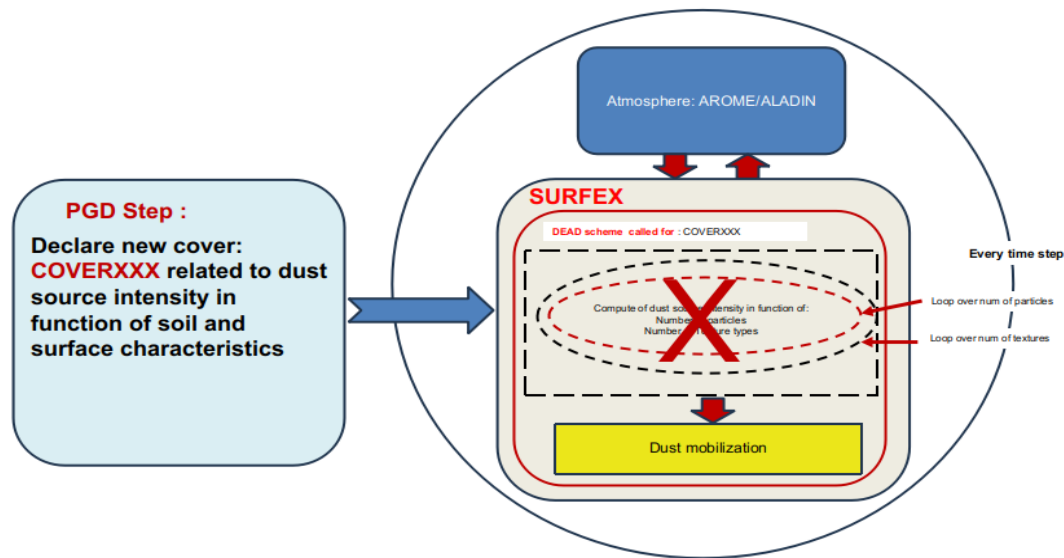


Figure 11: *CoverXXX* working processes

## 7 References

- [1] M. Mokhtari (2009) Modélisation des émissions et du transport des poussières désertiques dans Aladin.
- [2] M. Mokhtari (2011) ALADIN-DUST USER'S GUIDE ([https://www.umr-cnrm.fr/gmapdoc/IMG/pdf/Rapport-Mokhtari\\_2011.pdf](https://www.umr-cnrm.fr/gmapdoc/IMG/pdf/Rapport-Mokhtari_2011.pdf))
- [3] M. Mokhtari, L. Gomes, P. Tulet and T. Rezoug (2012) Importance of the surface size distribution of erodible material: an improvement on the Dust Entrainment And Deposition (DEAD) Model.
- [4] M. Mokhtari and A. Ambar (2016) Updating and validation of Arome\_dust. (stay report) ([http://www.umr-cnrm.fr/aladin/IMG/pdf/stay\\_report\\_mokhtari\\_ambar\\_2016.pdf](http://www.umr-cnrm.fr/aladin/IMG/pdf/stay_report_mokhtari_ambar_2016.pdf))
- [5] Marticorena, B., and G. Bergametti, Modeling the atmospheric dust cycle: 1. Design of a soil derived dust emission scheme, *J. Geo-phys. Res.*, 100(D8), doi:10.1029/95JD00,690, 16,415–16,430, 1995.
- [6] Kocha, C., J.-P. Lafore, P. Tulet and Y. Seity, 2011. High-resolution simulation of a major West African dust-storm: comparison with observations and investigation of dust impact, *Quarterly Journal of the Royal Meteorological Society*, vol. 138, issue 663, pp. 455-470.
- [7] Chaboureaud, J.-P., Flamant, C., Dauhut, T., Kocha, C., Lafore, J.-P., Lavaysse, C., Marnas, F., Mokhtari, M., Pelon, J., Reinares Martínez, I., Schepanski, K., and Tulet, P.: Fennec dust forecast intercomparison over the Sahara in June 2011, *Atmos. Chem. Phys.*, 16, 6977–6995, <https://doi.org/10.5194/acp-16-6977-2016>, 2016.
- [8] Zender, C. S., H. Bian, and D. Newman, Mineral Dust Entrainment and Deposition (DEAD) model: Description and 1990s dust climatology, *J. Geophys. Res.*, 108(D14), 4416, doi:10.1029/2002JD002775, 2003.

# The use of ECOCLIMAP Second Generation in AROME and its impact on urban simulation over Algiers

Nour El Isslam Kerroumi<sup>1</sup>, Rafiq Hamdi<sup>2</sup>

<sup>(1)</sup> Numerical Weather Prediction Department, Office Nationale de la Météorologie, Algiers, ALGERIA

<sup>(2)</sup> Climate modeling and impact studies Unit, Royal Meteorological Institute, Brussels, BELGIUM.

## 1 Introduction

---

This report builds on earlier research showing that ECOCLIMAP Second Generation, which includes Local Climate Zone (LCZ) data, significantly improves urban land cover representation. During my earlier research, the focus was on evaluating SURFEX Offline version 8.1 with the Town Energy Balance (TEB) scheme over Algiers city. That study revealed promising improvements in 2-meter temperature simulations in urban areas, particularly through the integration of ECOCLIMAP Second Generation, which significantly enhanced the representation of urban land cover compared to ECOCLIMAP v1.6. The results, based on Kouba station observations, highlighted the urban heat island effect and demonstrated that SURFEX Offline, under certain configurations, performed slightly better than SURFEX Online [1].

Building on these insights, our current research was motivated by the goal of implementing ECOCLIMAP Second Generation LCZ covers in the AROME model to assess its impact on urban simulations over Algiers city. However, due to AROME's CY43, used operationally at Météo-Algeria, incompatibility with ECOCLIMAP Second Generation when coupled with SURFEX v8.0, an alternative approach was necessary. This led to the development of a practical back phasing methodology to incorporate Local Climate Zone (LCZ) data from ECOCLIMAP Second Generation into ECOCLIMAP v1.6, while also adding external files such as building height, building fraction, and vegetation fraction. Additionally, we modified thermal parameters, including the albedo and thermal conductivity of Algiers' walls and roofs, to better represent the city's urban characteristics.

These modifications were integrated into AROME simulations in different setups to evaluate their impact on urban heat island phenomena, with the goal of improving the model's accuracy in representing urban weather dynamics.

## 2 Methodology

---

The AROME model, which is coupled with SURFEX v8.0, cannot directly read the land cover data from ECOCLIMAP Second Generation. To overcome this, we developed a method to transfer the Local Climate Zone (LCZ) data from ECOCLIMAP Second Generation into ECOCLIMAP v1.6, which is compatible with AROME.

The aim of this study was to evaluate the impact of using updated urban data from ECOCLIMAP Second Generation within the AROME model, and the effects of adding specific urban parameters like building height, building fraction, vegetation fraction, and thermal properties (albedo and thermal conductivity) on the Urban Heat Island (UHI) effect. Below are the detailed steps followed during the study:

# Step 1: Replacing Urban Covers in ECOCLIMAP v1.6 with LCZ Data from ECOCLIMAP Second Generation:

The first task involved replacing the urban cover data of ECOCLIMAP v1.6 with Local Climate Zone (LCZ) data from ECOCLIMAP Second Generation, to make it readable by AROME:

- PGD Creation with SURFEX v8.1:** We created an offline PGD file using SURFEX v8.1 in NetCDF format, which could then be read in MATLAB. This file included the Local Climate Zone (LCZ) covers present in the Algiers domain, as represented in Table 1 below.
- Data Replacement:** The urban covers in ECOCLIMAP v1.6 present in the Algiers domain were replaced with the corresponding LCZ data from ECOCLIMAP Second Generation. Specifically, the table below shows how each urban cover from ECOCLIMAP v1.6 was systematically replaced with the corresponding Local Climate Zone (LCZ) data from ECOCLIMAP Second Generation:

Table 1: Replacement of Urban Covers from ECOCLIMAP v1.6 with LCZ Data from ECOCLIMAP Second Generation.

ECOCLIMAP v1.6 Urban Covers	Replaced with LCZ Data from Ecoclimap Second Generation
COVER151	COVER024 (LCZ1)
COVER152	COVER025 (LCZ2)
COVER153	COVER026 (LCZ3)
COVER154	COVER028 (LCZ5)
COVER155	COVER029 (LCZ6)
COVER156	COVER031 (LCZ8)
COVER157	COVER032 (LCZ9)

After successfully replacing all the urban covers, the new version of ECOCLIMAP v1.6 was saved as "ecoclimap\_v1.6\_LCZ.dir." We then used the LandPrepSurf (LPS) tools developed by **Nicolas Ghilain** (From IRM) to visualize the cover maps of both the original and modified ECOCLIMAP versions.

The figure 1 illustrates the original ECOCLIMAP v1.6 urban cover map, while **Figure 2** displays the modified ECOCLIMAP v1.6 with LCZ-data urban cover map:

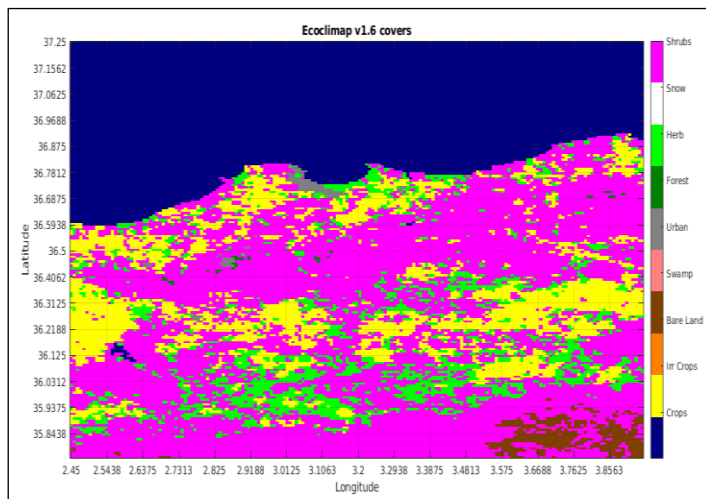


Figure1: Original ECOCLIMAP v1.6 Urban Cover Map.

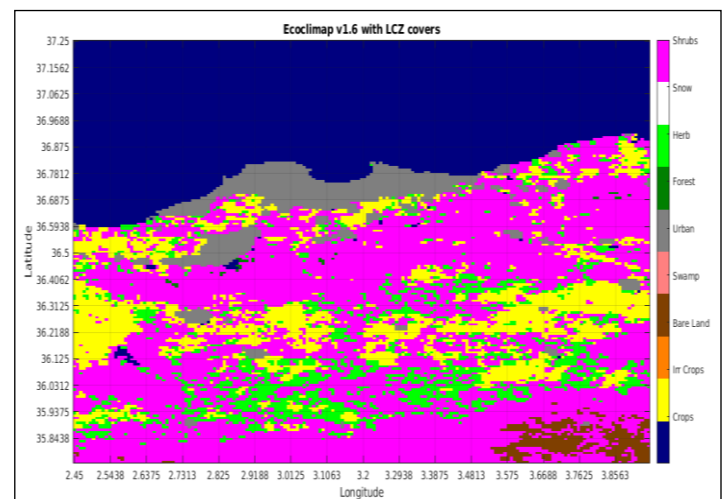


Figure2: Modified ECOCLIMAP v1.6 with LCZ Data Urban Cover Map.

The figure 3 and 4 shows more details about the representation of LCZ cover in Algiers domain plotted by Qgis and Rfa R-package respectively:

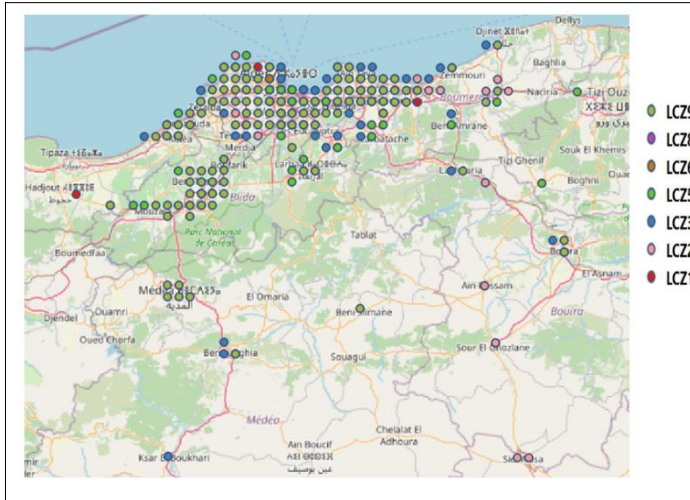


Figure 3: Local climate zone urban cover representation on Algiers domain.

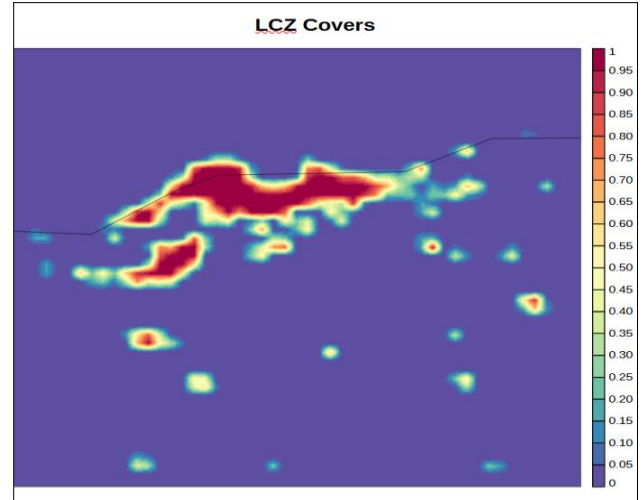


Figure 4: the sum of local climate zone Urban Cover from PGD file.

## Step 2: Creating 3D Geometry ( Building Height and Building Fraction Files)

To enhance the urban simulation, we added additional parameters like building height and building fraction:

- **QGIS for Data Processing:** Using QGIS, we created the building height and building fraction files for the AROME domain with a resolution of 3 km. These files were based on urban maps and building data from the Geoservice of the Earth Observation Center (EOC) of the German Aerospace Center (DLR). We downloaded the height and building fraction maps in TIFF format from their website (<https://geoservice.dlr.de/web/maps/eoc:wsf3d#>), which are available at a resolution of 90 m. After importing them into QGIS, we clipped the maps to fit our AROME 3 km domain and then reprojected them to 3 km using the mean method.
- **Conversion to Text Files:** The maps generated in QGIS were exported and converted into text files. These files captured the spatial distribution of building heights and building fractions, which were subsequently used as input for the creation of the PGD file.
- **Creating PGD with external ascii height and fraction building files:** It's important to have an equal or higher resolution than the resolution of your PGD, and to have the entire PGD domain included in your ascii file.

Next, your ascii file must be organized in 3 columns corresponding to LAT, LON and VALUE, with just one space separating the columns.

After creating the two ASCII files, we named the height building file "H\_bld.txt" and the building fraction file "bld\_frac.txt". These files were then added to the *OPTIONS.nam* configuration to generate the PGD file.

After creating the PGD with the updated files, Figure 5 and Figure 6 show the building height and building fraction data files at 3km of resolution, respectively:

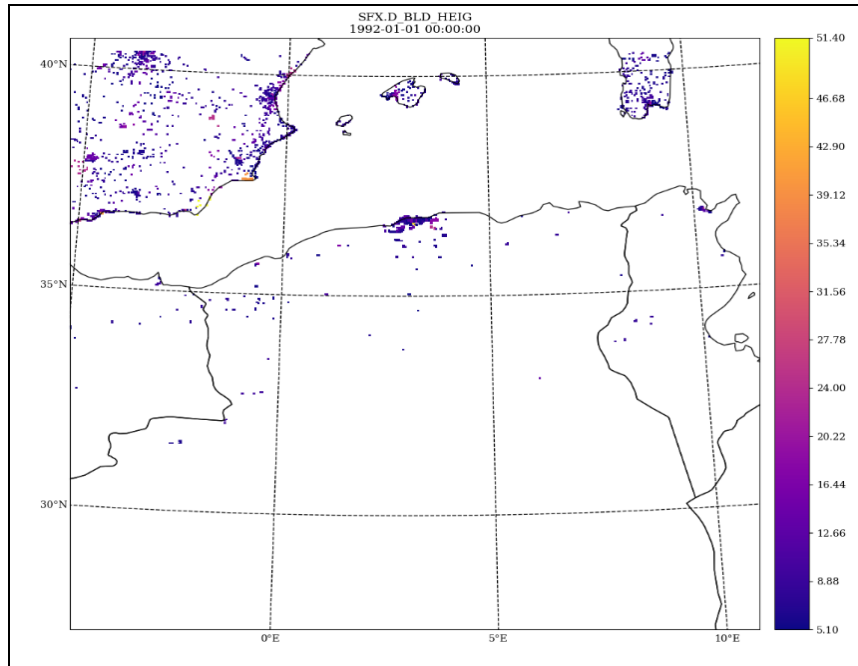


Figure 5: Height building input data file

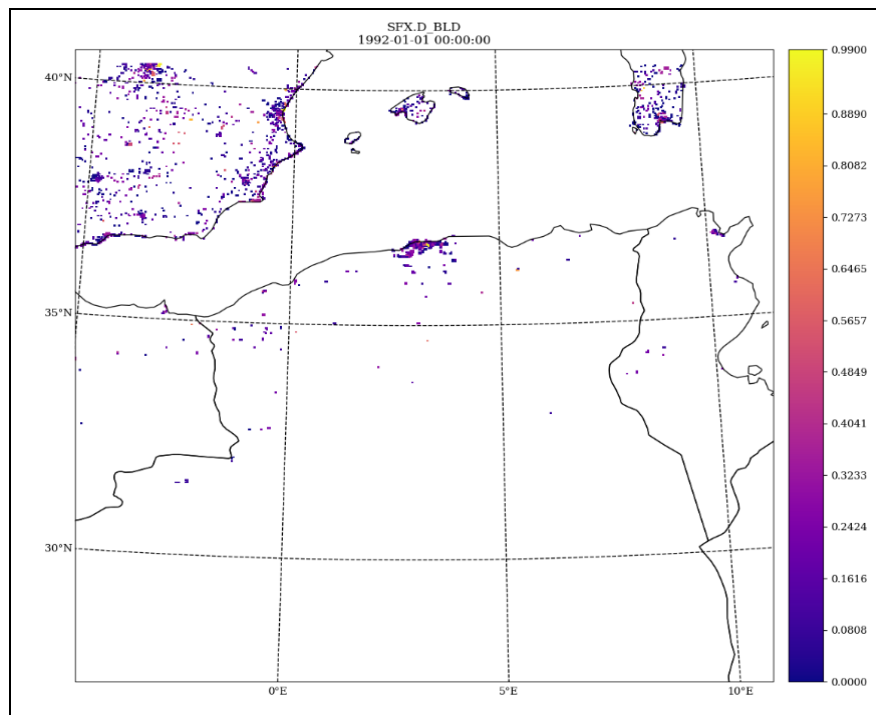


Figure 6: Building fraction input data file

### Step 3: Creating Vegetation Fraction File

The vegetation fraction file was essential for enhancing urban simulations. Using ECOCLIMAP Second Generation data, we generated an offline PGD file with SURFEX v8.1 to capture the vegetation covers across the domain. Multiple cover types were summed to create a total vegetation fraction file. Specifically, we used the PINUTS package (edf) to extract vegetation data into an ASCII format with longitude, latitude, and cover values. Then, a Python script combined these values to produce a final ASCII file, “veg\_frac.txt,” containing the total vegetation fraction. This file was included in the OPTIONS.nam to generate the PGD file.

After creating the PGD with the updated file, Figure 7 shows the vegetation fraction data file:

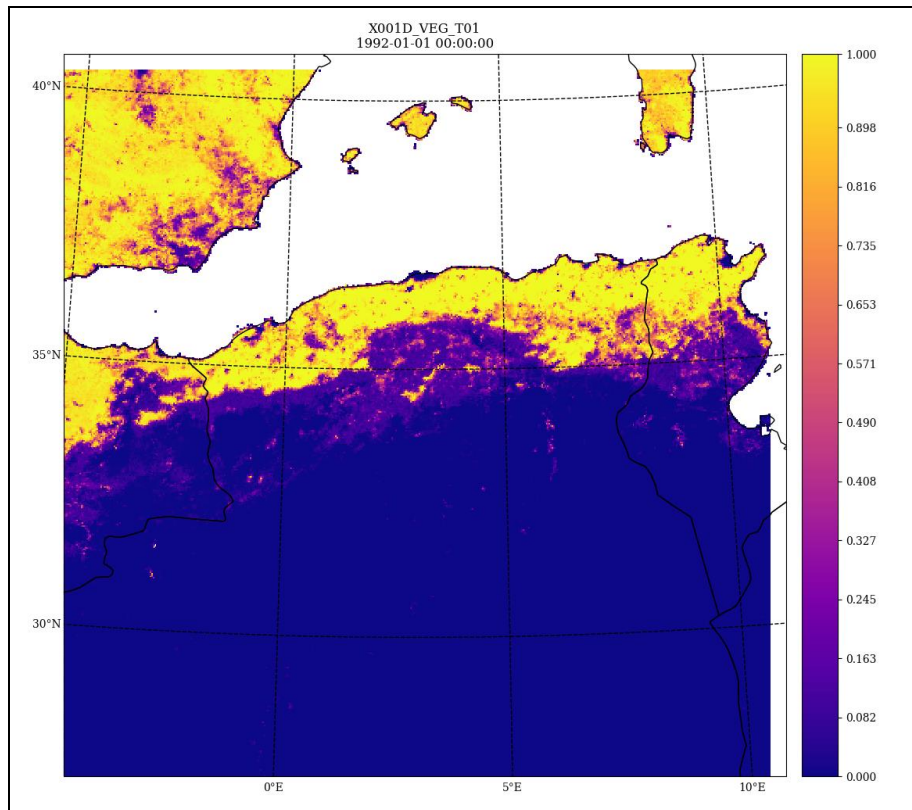


Figure 7: Vegetation fraction input data file.

### Step 4: Thermal Parameters (Albedo and Thermal Conductivity)

Urban surfaces have distinct thermal properties, which can influence heat dynamics:

- **Albedo:** we obtained value for the albedo of Algiers' walls and roofs from published research articles (Atik Tarik [2]):

	Default value	New value
Albedo of wall	0.25	0.5
Albedo of roof	0.15	0.08

These values were read by LPS tools of Nicolas Ghilain. And the new values were added on the OPTIONS.nam to generate the PGD file.



- **Thermal Conductivity (TC) Values:** we calculate the value for the thermal conductivity of Algiers' walls and roofs from published research article (Hicham Kadraoui and al [3]) in function of the thermal transmittance value  $U$  ( $Wm^{-2}K^{-1}$ ) and the layer thickness (m) of each of the wall and the roof. The table 2 shows the values of  $U$  and the layer thickness:

Table 2: Layer thickness, walls composition and thermal transmittance values of building elements [3].

System Element	Material and wall composition	Layer Thickness (m)	Thermal transmittance $U$ ( $Wm^{-2}K^{-1}$ )
Exterior walls	Mortar cement	0.015	2.6096
	Stone	0.400	
	Mortar cement	0.015	
	Plaster	0.010	
Roof	Tiling	0.025	3.6955
	Mortar cement	0.015	
	Concrete	0.120	
	Plaster	0.015	

To calculate the effective thermal conductivity  $TC_{wall}$  of the entire wall, we use the following formula based on the overall thermal resistance  $R_{total}$  and the total thickness of the wall:

$$TC_{wall} = \frac{\text{Total thickness}}{R_{total}}$$

Where the total thermal resistance  $R_{total}$  is calculated:

$$R_{total} = \frac{1}{U} \cong 0.38$$

And Total Thickness of the Wall:

$$\text{Total thickness}_{wall} = 0.015 + 0.4 + 0.015 + 0.010 = 0.44 \text{ m}$$

Then, the thermal conductivity  $TC_{wall}$ :

$$TC_{wall} = \frac{0.44}{0.38} \cong 1.15 \text{ Wm}^{-1}K^{-1}$$

With the same method, we calculate  $TC_{roof}$ :

$$TC_{roof} \cong 0.648 \text{ Wm}^{-1}K^{-1}$$

After the calculation of the wall and roof thermal conductivity, we have used LPS tools to modify their value in the urban cover and create a new ecoclimap binary file named *ecoclimap\_I\_covers\_TC.bin*.



### Step 5: AROME Simulation Setups

We set up an AROME configuration with 3 km of resolution and 41 vertical levels (Sara Chikhi and al [4]):

*Table 3: AROME configurations characteristics.*

Characteristics	AROME
Cycle	CY43T2.bf.03
Initial Conditions	Coupling (ALADIN 6Km)
Coupling frequency	1h
Horizontal resolution	3 km x 3 km
Vertical resolution	41 Levels
Time-step	180 s
First level from ground	17 meters
Grid	400x 400
Lead Time	24 Hours
Domain	Center : 3°E – 34°N Latitude : 28°N – 40°N Longitude: 3°W – 9°E

To evaluate the impact of the modified ECOCLIMAP v1.6 and additional external data on urban heat island (UHI) simulation, we performed four AROME simulations. Each setup is outlined below and summarized in Table 3.

1. **Setup 1:** The operational AROME simulation at 3 km resolution was run using the original ECOCLIMAP v1.6 with no modifications. This serves as the baseline for comparison.
2. **Setup 2:** The second simulation used the modified ECOCLIMAP v1.6 with LCZ data covers replacing the original urban covers. Additionally, an external vegetation fraction file “veg\_frac.txt” was included to improve vegetation representation.
3. **Setup 3:** In this setup, along with the modified ECOCLIMAP v1.6 (with LCZ data covers) and the external vegetation fraction file, we introduced height building and building fraction files (H\_bld.txt and bld\_frac.txt) to represent more accurate urban geometry.
4. **Setup 4:** The final setup built on Setup 3 by further modifying thermal parameters, specifically the albedo and thermal conductivity (TC) for walls and roofs, using values from published studies. This setup aimed to simulate the impact of these parameters on UHI phenomena.

This setup structure allows us to systematically assess the contributions of LCZ data, external files (vegetation fraction, building height, building fraction), and thermal parameters to the accuracy of UHI simulations.

### Step 6: Evaluating the Urban Heat Island (UHI) Effect

The Urban Heat Island (UHI) effect was evaluated by comparing the results of the four setups:

- **Urban heat Island Data Comparison:** The simulations were compared to operational AROME simulations, particularly from the Urban Meteorological station “kouba” and the rural Meteorological station “mehalma”, to assess the temperature differences and the extent of the UHI effect.
- **Analysis of Different Setups:** The goal was to evaluate how each of the modifications (LCZ data, external files, and thermal parameters) impacted the representation of urban heat island phenomena in the simulations.

## 3 Results

### 1. Simulation Setup

Four different AROME simulations were conducted with various urban parameter configurations to evaluate the Urban Heat Island (UHI) effect. The four setups are as follows:

- **Setup 1:** *UHI\_oper* – Operational simulation of AROME at 3km resolution using the standard ECOCLIMAP v1.6.
- **Setup 2:** *UHI\_lcz-veg* – Simulation of AROME at 3km resolution with LCZ data from ECOCLIMAP Second Generation and external vegetation fraction file.
- **Setup 3:** *UHI\_lcz-veg-bld* – Simulation of AROME at 3km resolution with LCZ data, external vegetation fraction file, height building, and building fraction files.
- **Setup 4:** *UHI\_lcz-veg-bld-albedo-tc* – Simulation of AROME at 3km resolution with LCZ data, external vegetation fraction file, height building, building fraction files, and modified thermal properties for walls and roofs (albedo and thermal conductivity).

### 2. UHI Temporal Analysis

The UHI was evaluated by calculating the temperature difference between the urban site (Kouba) and the rural site (Mehalma). Figure 8 and 9 presents the mean UHI values for the month of January and of July 2023 respectively:

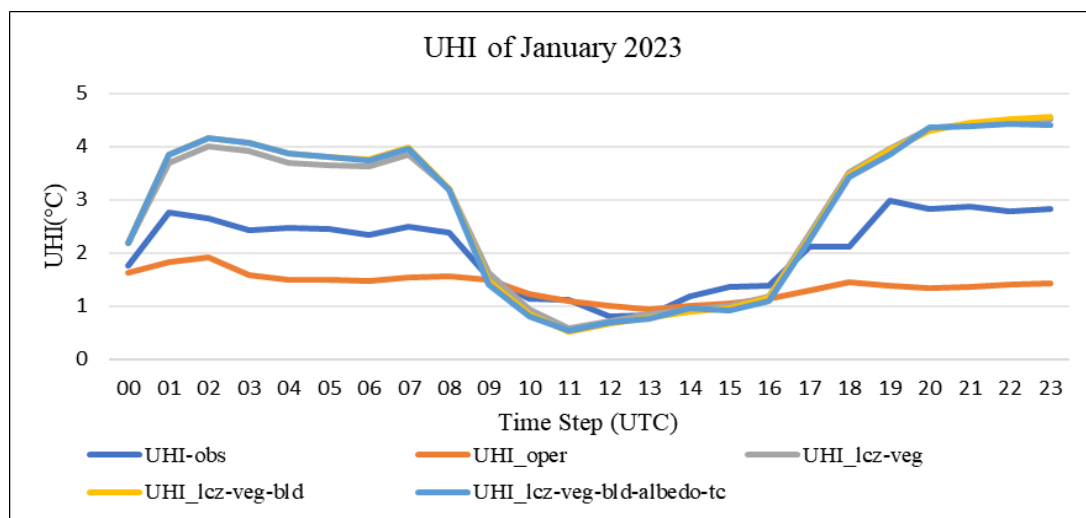


Figure8: UHI Simulation Result: Comparison of Different Setups (January 2023)

In January, the observed Urban Heat Island (UHI) effect shows a typical pattern with high nighttime values (2.7–2.9 °C) and lower midday values (around 0.8 °C). The operational model underestimates UHI, especially during the night, due to limited urban representation. Enhanced models incorporating Local Climate Zone (LCZ) data, with added vegetation, building parameters, albedo, and thermal conductivity, show improved accuracy, particularly during nighttime. These results highlight the importance of detailed urban characteristics in accurately capturing UHI dynamics, as models with urban-specific data better reflect the observed UHI patterns.

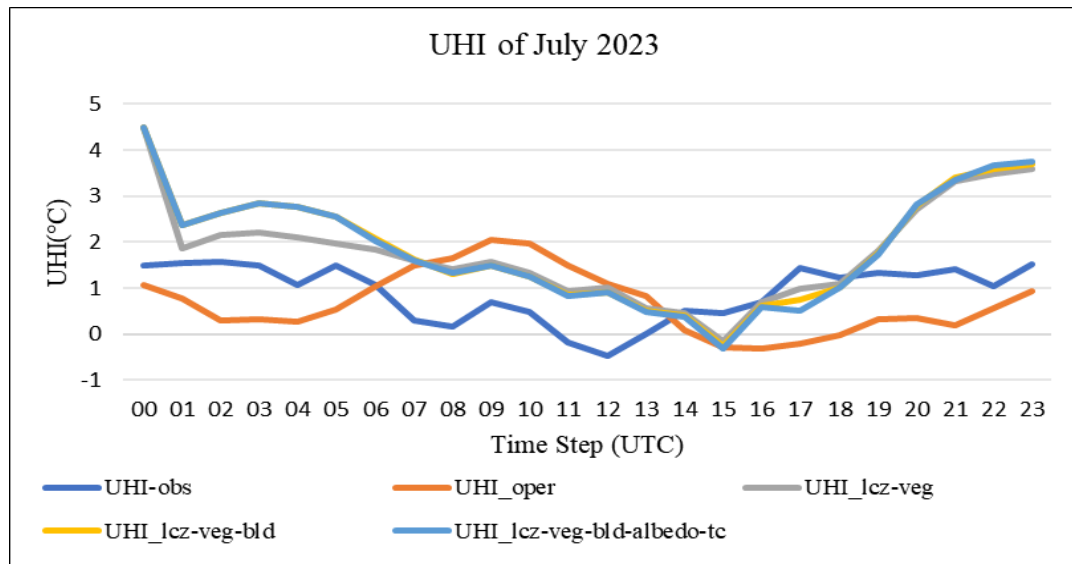


Figure9: UHI Simulation Result: Comparison of Different Setups (July 2023)

In July 2023, the observed Urban Heat Island (UHI) effect exhibits distinct nighttime peaks around 1.5 °C, while daytime values fluctuate between zero and slightly negative, indicating reduced urban heat retention. Notably, during the period from July 15th to 21st, forest fires near Mehalma station contributed to negative UHI values at night, reflecting an unusual cooling effect. The operational model significantly underestimates UHI, particularly during nighttime hours, whereas models enhanced with Local Climate Zone (LCZ) data more accurately capture observed conditions. Specifically, models incorporating additional urban characteristics—such as vegetation, building parameters, albedo, and thermal conductivity adjustments—reveal UHI values exceeding 4 °C at night. These results emphasize the importance of incorporating detailed urban features in modeling efforts to accurately represent UHI dynamics during warmer periods.

### 3. UHI Spatial Aspect:

To complement the temporal analysis, we also evaluated the spatial distribution of the UHI effect. We generated maps of the difference between the temperature at 2 meters (T2M) and the mean temperature of rural points in the domain (3km grid resolution). These maps were plotted for midday(12h) and night (21h). For each time point, the spatial analysis was conducted across the four setups, followed by a zoom into the Algiers domain to better visualize the urban heat island within the Algiers city:

**Spatial UHI at 12:00 on July 18th, 2023:**

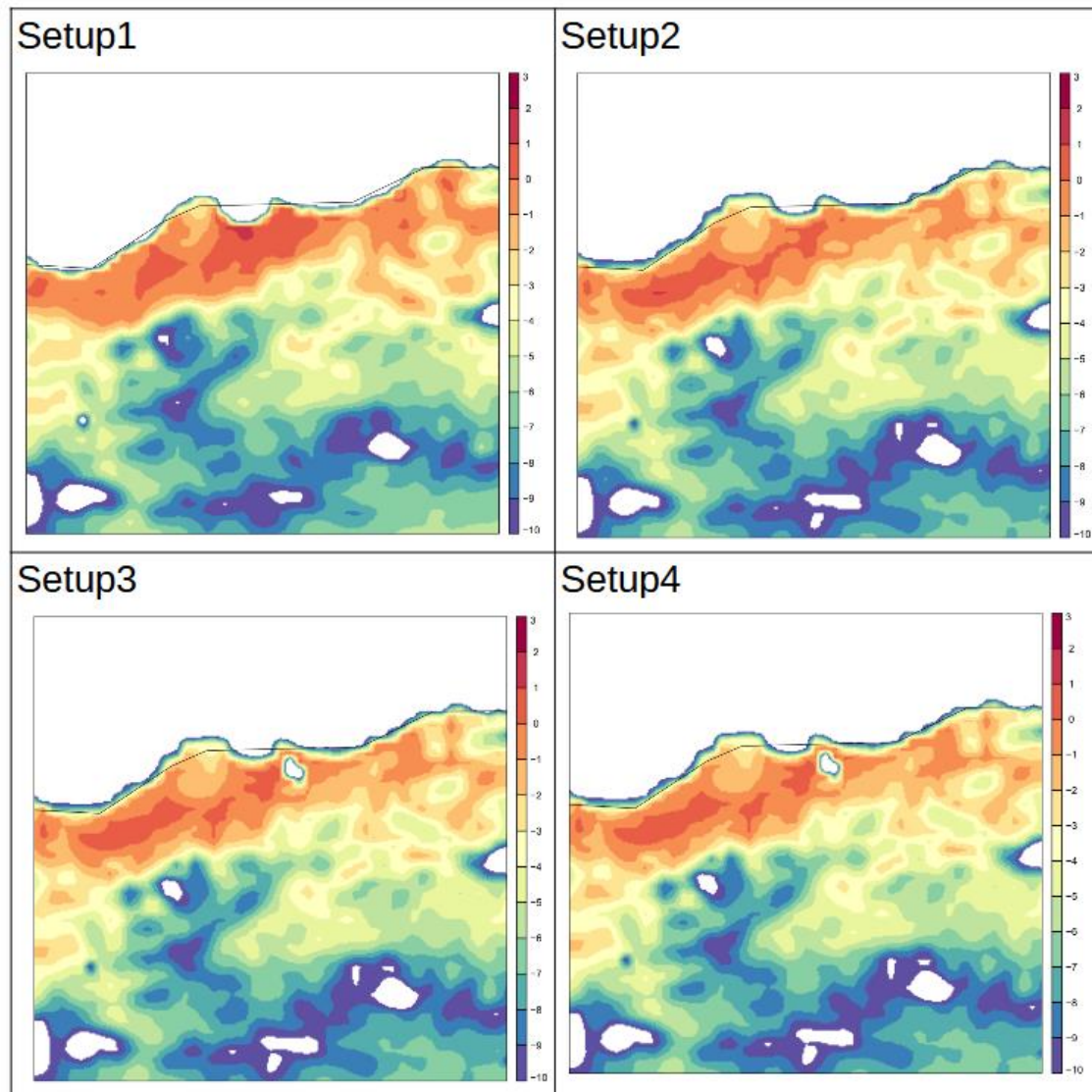


*Figure 10: Spatial UHI at 12h on July 18<sup>th</sup>, 2023 for the different Setups.*

**Spatial UHI at 21:00 on July 18th, 2023:**

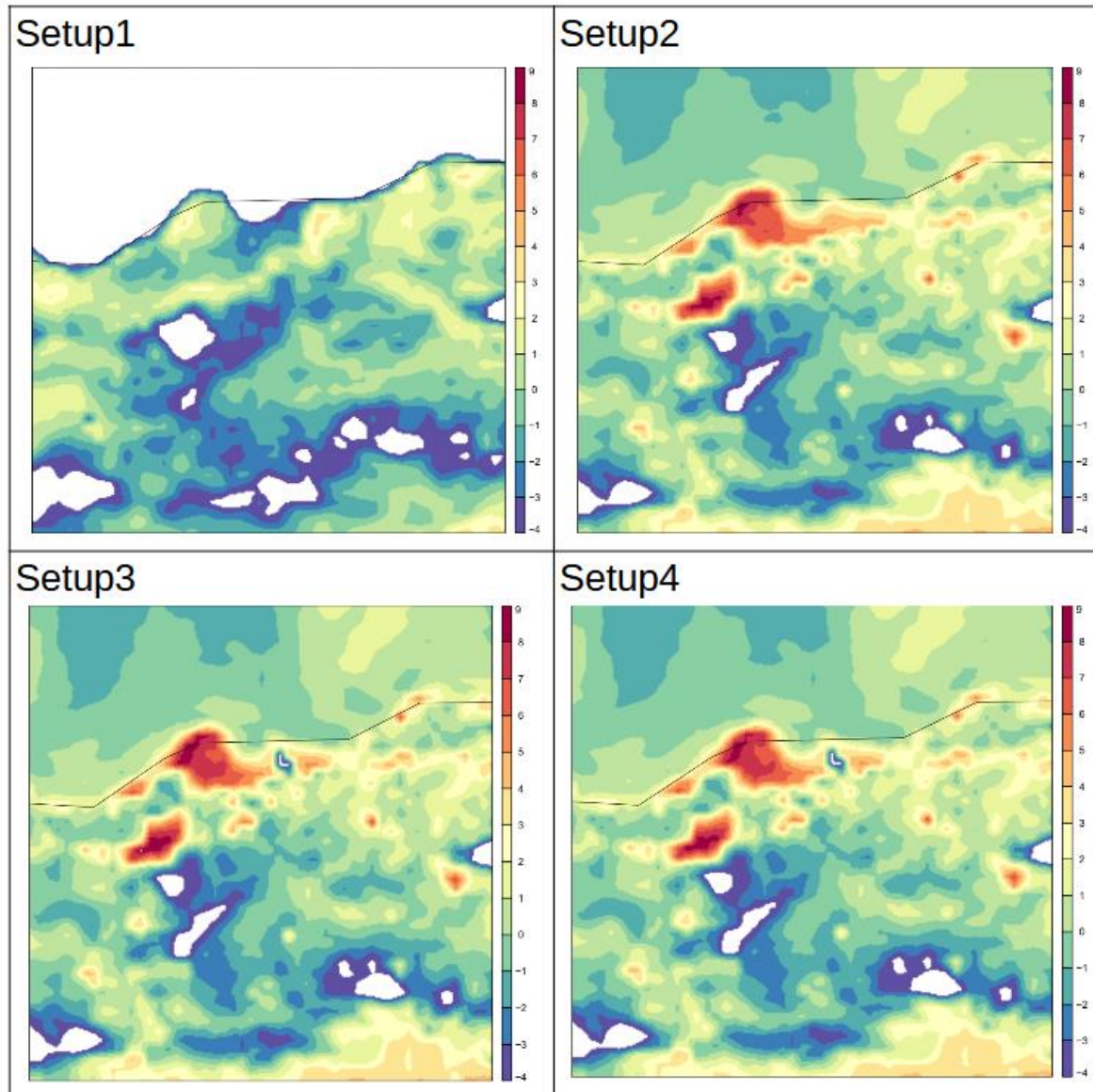


*Figure 11: Spatial UHI at 21h on July 18<sup>th</sup>, 2023 for the different Setups.*

The spatial analysis of the UHI effect across the four setups at midday (12:00) and evening (21:00) on July 18th, 2023 (Figure 10 and 11), reveals consistent trends. During the day, the UHI effect intensifies in urban areas, with higher temperatures observed in the city compared to rural surroundings. This effect becomes more pronounced with the inclusion of LCZ data, building height, and building fraction. At night, the UHI remains significant, with urban areas retaining heat, especially where buildings are taller and denser. Modifying thermal properties such as albedo and thermal conductivity slightly reduces the nighttime heat retention, offering a potential strategy for mitigating the UHI effect.

## 4 Conclusion and Perspectives

During my research stay at the Royal Meteorological Institute of Belgium (RMI), the results demonstrated that including Local Climate Zones (LCZ), vegetation fractions, spatial variation in building characteristics, and localized thermal properties substantially influences UHI simulations at 3km operational resolution, particularly during the evening hours when the urban heat retention is most pronounced.

Looking ahead to next year, we plan to build upon these findings by testing these new setups at a higher resolution of 500 meters for both inline (operational run) and offline runs using SURFEX V8.1. This will allow for a more detailed assessment of urban heat dynamics in Algiers, enabling us to evaluate the model's performance against observed data and to test the impact of including the urban effect on operational scores with both the inline/offline setup and on two extreme events including heat wave and extreme precipitation over Algiers.

## 5 References

- [1] Nour El Isslam Kerroumi, Rafik Hamdi, "Evaluation of Surfex/TEB offline over the city of Algiers: a first step toward high-resolution operational forecast", ACCORD NL5, pages 21-31, 27 March 2024.
- [2] Tarik Atik, "Les Toitures végétalisées à Alger, pour une contribution à l'amélioration du microclimat urbain méditerranéen", Thèse de Magister, page 127, May 2011.
- [3] Hicham Kadraoui, Sidi Mohammed El Amine Bekkouche and Abdelhak Chikhaoui, "Analysis of energy consumption for Algerian building in extreme North-African climates", International Journal of Sustainable Energy Planning and Management Vol. 19, pages 45–58, 2019.
- [4] Sara Chikhi, Mohamed Mokhtari, Abdenour Ambar, Islam Bousri, Mohamed Arab Benamara "Operational Numerical Weather Prediction Models Verification at Météo Algérie", ACCORD NL1, pages 25-35, October 2021.

# AROME-500m operational configurations at Météo-France

Salomé Antoine, Yann Seity, Eric Bazile, Ludovic Auger,  
Rachel Honnert, Patrick Le Moigne, Valéry Masson, Adrien Napoly, Jean Wurtz

## 1 Introduction

One topic of Météo-France's 2022-2026 COP (Objectives and Performances Plan) was to provide two AROME configurations at 500 m for the Paris Olympics Game, one over Paris and one for the Mediterranean-Alps domain. The Paris zone was to cover high-stakes areas and airports, while the Alps zone was to include sailing competitions in Marseilles. These configurations were constrained by the supercomputer dedicated computing resources to deliver the product at forecasters on time.

## 2 Description of configurations and settings

Hectometric forecasts with AROME are carried out on two domains. They are shown in figure 1:

- **AROME-Paris**, 250km x 250km, around Paris. It covers the two Paris airports and should better forecast fog and urban heat islands.
- **AROME-Medalp**, 480km x 576km, covering the Alps and the Mediterranean sea. It should better forecast Mediterranean episodes and mountain weather.

The forecasts are deterministic, with one run per day for a 36-hour forecast for AROME-Paris and a 24-hour forecast for AROME-Medalp. For both domains, there are also nowcasting forecasts (up to 6 hours), 24 times a day with outputs every 15 minutes. We do not detail these configurations here. Forecasts are made with a horizontal resolution of 500 m, without data assimilation. Initial and lateral boundary conditions are provided by AROME-France analysis and forecasts.

The AROME-500m configurations are based on the AROME-France configuration (Seity et al. 2011, Brousseau et al. 2016), with some adaptations. The changes are detailed below summarized in table 1.

### 2.1 Vertical grid

The first change is related to the **vertical grid**. In AROME-France, the vertical grid has 90 vertical levels, 9 levels below 200 m and a first level at 5 m (AROME-L90 on figure 1). In AROME-500m, the vertical grid comprises 120 vertical levels, with 17 levels below 200 m and a first level at 2.5 m (AROME-L120 on figure 1). In comparison, ARPEGE has 105 vertical levels, 7 levels below 200 m and a first level at 10 m (ARPEGE on figure 1).

The height of the lowest model level and the higher density of vertical levels near the surface are important to improve the fog forecasts (Antoine et al., 2023) and the minimum temperature in the mountains especially unstable boundary layer.



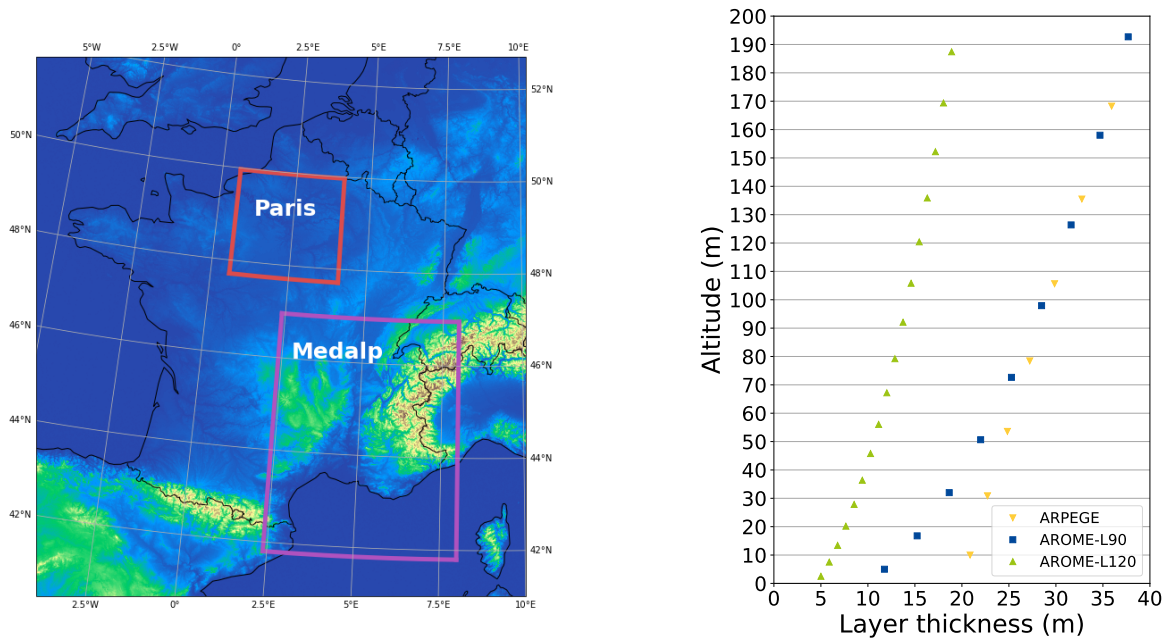


Figure 1: On the left, the two hectometric domains of AROME, in red AROME-Paris and in violet AROME-Medalp. On the right, the vertical grids of ARPEGE, AROME-L90 and AROME-L120 over the first 200 meters above ground.

## 2.2 Surface description

### 2.2.1 Orography database - SRTM

In AROME-France, the surface database used is GMTED with a resolution of 250 m. In AROME-500m, the database has been replaced by SRTM database with an horizontal resolution of 30 m.

The use of this more detailed database provides more realistic sub-grid parameters, and small scale valleys (Fig. 2). Mountain heights also seem more realistic. For example, the maximum altitude of the Alps in the model, corresponding to Mont-Blanc, is 4300 m in AROME-France versus 4650 m in AROME-Medalp (4810 m in reality).

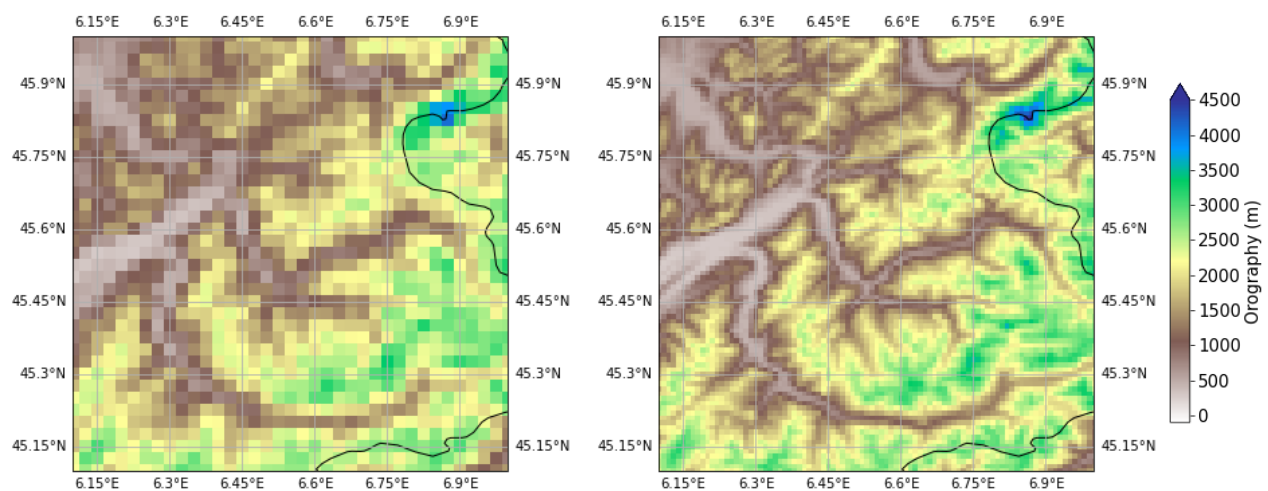


Figure 2: Alpine valley in AROME-France on the left and in AROME-Medalp on the right.

### 2.2.2 Physiography database - ECOCLIMAP-SG

Physiography database used in AROME-500m for nature parameters is ECOCLIMAP-SG. The number of land-covers has been reduced compared with ECOCLIMAP-1 used in AROME-France: 33 cover versus 256. The albedo database is more recent, computed from 2008-2012 CGLS data (Carrer et al. 2014). The annual LAI (Leaf Area Index) cycle is more realistic and is calculated from 2014-2016 CGLS LAI data (Munier et al. 2018).

### 2.2.3 Open Street Map

Open Street Map (OSM) open-access database has been processed using Geoclimate tool (Geoclimate) generating vector data. This vector dataset has been finely rasterized to 100 m resolution for use by SURFEX. It modifies the tile fractions and urban characteristics: town, nature and water fractions, building height, road fractions, etc.

With this database, there are more urban and water areas and less nature in the surface description (Fig. 3). The path of the Seine river is much more visible with the OSM database. It also plays an important role in describing the city.

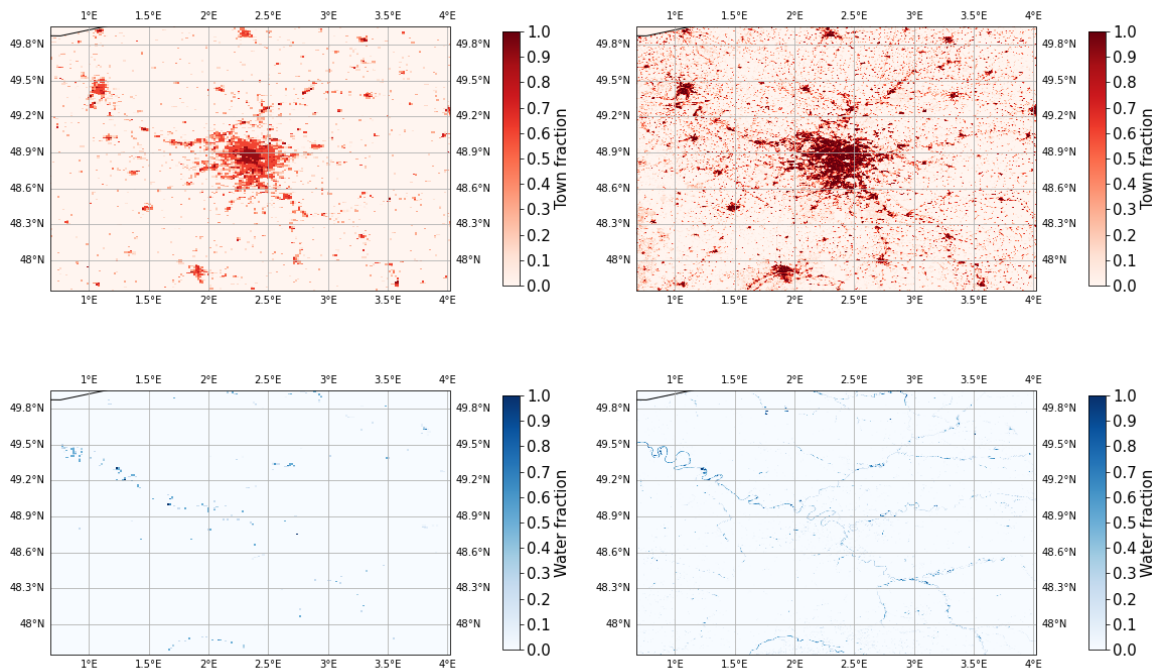


Figure 3: Town (on top) and water (on bottom) fractions in AROME-France (left) and AROME-Paris (right).

### 2.2.4 Soil type database - Soilgrid

The soil type database used in AROME-500m is the Soilgrid database at 250 m resolution (Hangl et al. 2017). This database provides presumably a more detailed and up-to-date description of the soil types compared to the HWSD database used in AROME-France. This has a particular impact on the sand and clay fractions in the soil.

### 2.2.5 GARDEN option in TEB

With the GARDEN option (Lemonsu et al. 2012), vegetation is included in the TEB scheme (Masson 2000). This option has been activated in the AROME-500m configurations. This explains also why the urban fractions in Paris are much higher in AROME-500m, as NATURE tiles within the city are now within the urban canyon in TEB. This cools temperature inside the city (Fig. 4) and makes it easier to estimate minimum temperatures in Paris.

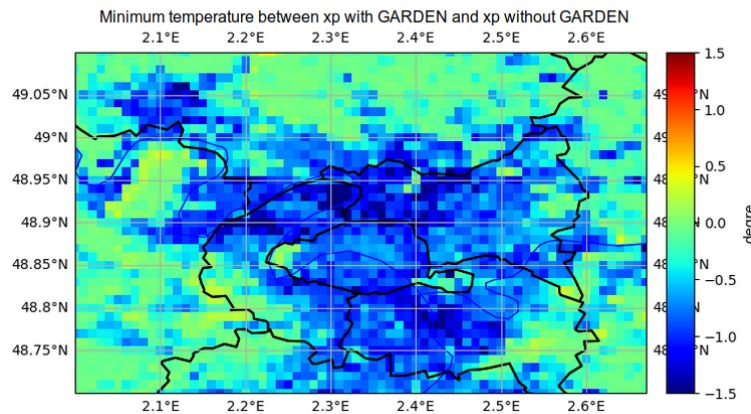


Figure 4: Minimum temperature difference, calculated between 1800 and 0600 UTC, averaged over 1 month (July 2022), between an AROME-Paris experiment with GARDEN and one without.

### 2.2.6 Surface file preparation

Suspicious snow contents in surface appeared after interpolations during the preparation of the surface initial file, especially in mountain areas. Activating the LSNOW\_IDEAL keys in the so called 'prep' task removes this suspicious snow content.

Indeed, when the key is deactivated, interpolating the snowfield from a looser to a finer grid can produce strange results. When the altitude of the final point is higher than the altitude of the initial point, snow is added. Conversely, when the altitude of the final point is lower than the altitude of the initial point, snow is deleted. This brings out the valleys and peaks with unrealistic snow contents. When the key is activated, the difference between the initial and finish relief is not taken into account when interpolating the snowfield.

### 2.2.7 Vegetation thermal capacities

Initial experiments with AROME-Paris have shown a warm bias in the forecasts, particularly during summer nights. In order to reduce this bias, the vegetation thermal capacities parameters ( $C_v$ ) has been tuned. In AROME-France, the settings are as follows:  $2 \cdot 10^{-5} \text{ K m}^2 \text{ J}^{-1}$  for low vegetation and  $1 \cdot 10^{-5} \text{ K m}^2 \text{ J}^{-1}$  for high vegetation.

Increasing the vegetation heat capacity coefficient helps in reducing the night-time heat bias around Paris. The impact was fairly low in winter and in the Medalp area. The setting used in AROME-500m is  $5 \cdot 10^{-5} \text{ K m}^2 \text{ J}^{-1}$  for low vegetation and  $2.5 \cdot 10^{-5} \text{ K m}^2 \text{ J}^{-1}$  for high vegetation.

## 2.3 Dynamical settings

The initial **time step** chosen for the AROME-500m simulations was 30s. However, unrealistic waves in the rain, temperature and wind fields appeared in some particular situations. None acceptable solution was found with a time step of 30s and the solution was to reduce the time step to 20s.

Figure 5 shows one of the cases where there were waves in the rain fields with a time step of 30s. These waves are greatly reduced with a time step of 20s.

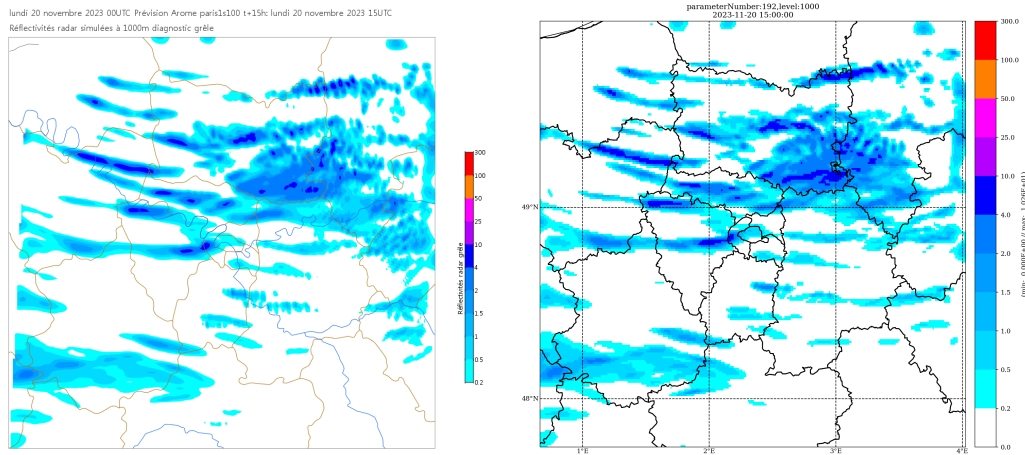


Figure 5: Radar reflectivities simulated with AROME-Paris forecasts with a 30s time step on the left and a 20s time step on the right.

For numerical stability reasons, **horizontal temperature** diffusion was activated. The other prognostic fields were already diffused. The model stability is very sensitive to this choice and scores are little impacted.

Initial forecast tests revealed unrealistic precipitation rates, particularly in shower cases, highlighting the need for **more frequent updated lateral boundary conditions**. In this way, AROME-500m is coupled with AROME-France every 15 minutes.

Figure 6 shows the cumulative precipitation over 3h for a rainy event in the Paris region on September 1, 2023, and the impact of a 15 min coupling. With hourly coupling, the maximum cumulative precipitation is very high (34mm) compared with observation (20mm) and the AROME-France forecast (12mm). With a 15-minute coupling, the maximum is reduced to a more realistic amount of 13mm.

## 2.4 Physical settings

One of the objectives of AROME-500m, particularly over Paris region, is to improve fog forecasts. However, one of the model's shortcomings is that it produces too thick fogs with high water content, especially in the lower layers. Taking **droplet deposition on vegetation** into account reduces this problem (Antoine et al. 2023, Mazoyer et al. 2017).

Droplet deposition on vegetation was activated in AROME-500m, with a constant deposition rate of  $0.2 \text{ cm.s}^{-1}$  (like in Antoine et al. 2023 or Mazoyer et al. 2017).

In relation to the lowering of the first model level above ground level, the **Richardson critical number** was also adjusted from 0.2 in AROME-France to 0.05 in AROME-500m. In addition, this modification reduces the bias of warm night-time temperatures during the summer in Paris.

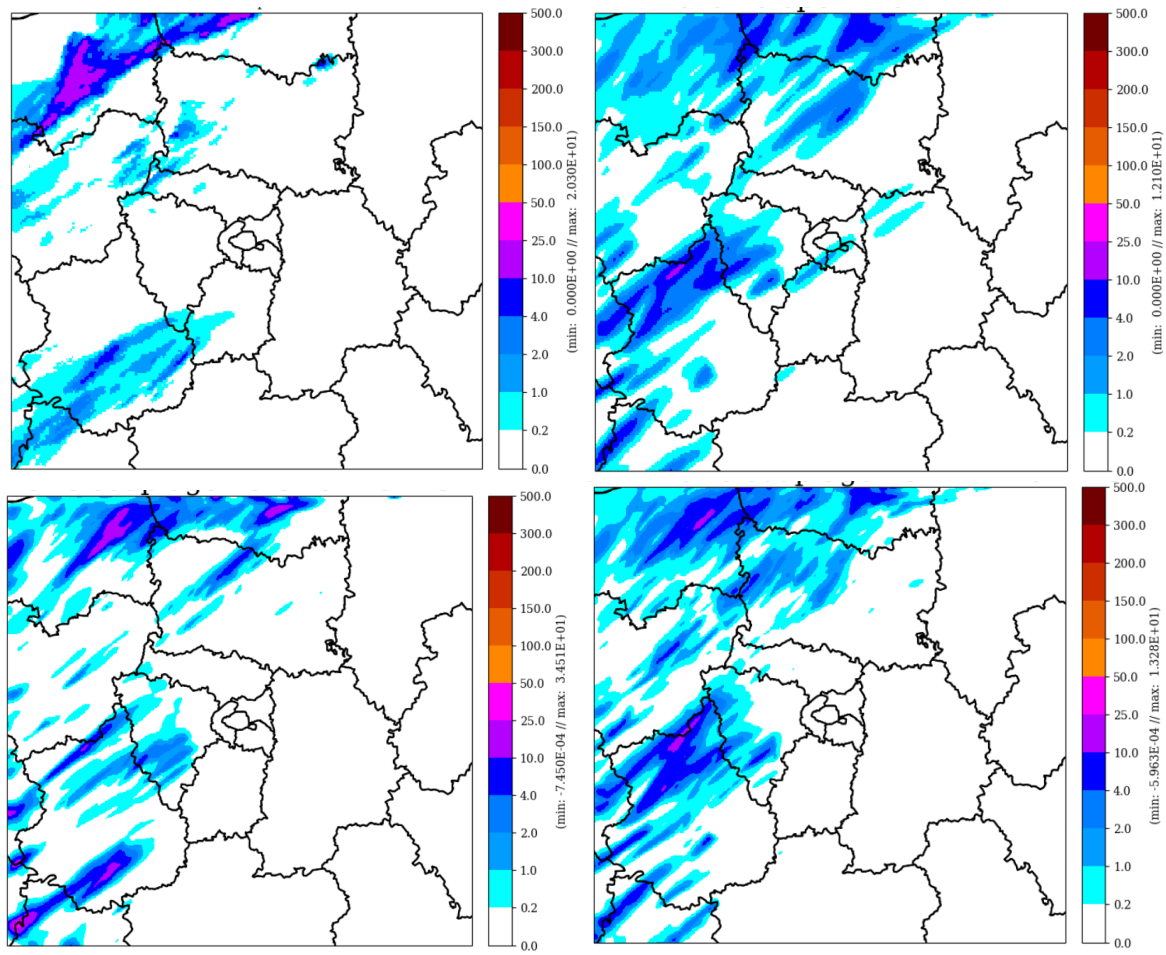


Figure 6: Three-hour cumulative rainfall on September 1, 2023 in the Paris region for different model configurations and observations: top left, Antilope observations; top right, AROME-France forecast; bottom left, AROME-500m forecast with hourly coupling; bottom right, AROME-500m forecast with 15min coupling.

## 2.5 Settings summary

Table 1: Summary table of settings in AROME-500m versus settings in AROME-France.

	AROME-France	AROME-500m
Coupling frequency	1h	15min
Time step	50s	20s
Vertical grid	L90	L120
First level height	5m	2.5m
Temperature diffusion (&NAMDYN RDAMPT=20.,)	No	Yes
Richardson parameter	0.2	0.05
Droplet deposition	No	Yes ( $0.2 \text{ cm.s}^{-1}$ )
Orography database	GMTED 250m	SRTM 30m
Soiltype database	HWSD 1km	Soilgrid 250m
Physiography database	ECOCLIMAP-1	ECOCLIMAP-SG
Tile characteristics	ECOCLIMAP-1	OSM
Garden	No	Yes
Cv for low vegetation	$2 \cdot 10^{-5} \text{ K m}^2 \text{ J}^{-1}$	$1 \cdot 10^{-5} \text{ K m}^2 \text{ J}^{-1}$
Cv for hight vegetation	$5 \cdot 10^{-5} \text{ K m}^2 \text{ J}^{-1}$	$2.5 \cdot 10^{-5} \text{ K m}^2 \text{ J}^{-1}$



### 3 Evaluation

#### 3.1 Orography comparison

To assess the impact of the change in resolution and the use of the SRTM database on the realism of model orography, elevation errors was computed. The evaluation is done by using the altitude of observation points (used for the T2m evaluation) with the altitude of the nearest model point. The results for ARPEGE, AROME-France and AROME-Medalp are shown in figure 7.

There is a clear improvement in the realism of AROME-Medalp orography. The average bias is divided by ten between AROME-France and AROME-Medalp. For AROME-Medalp, almost all measurement points are less than 50m height above the nearest model point.

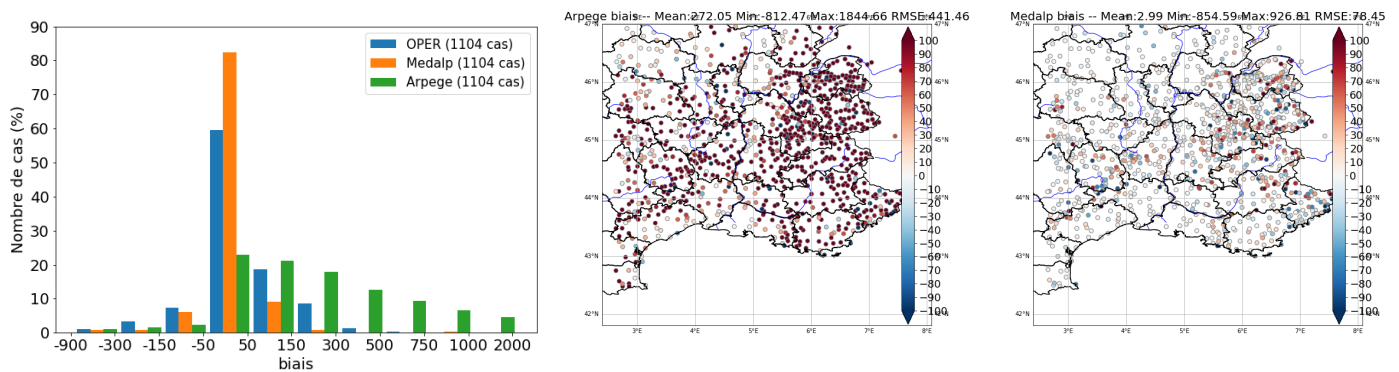


Figure 7: Orography errors: distribution of errors for different models (left), map of errors for Arpege (middle) and Medalp (right).

#### 3.2 Temperature scores

Temperature scores, bias and RMSE, were calculated for AROME-500m against AROME-France and ARPEGE between mid-May and mid-September 2024. The results are shown in figure 8.

In the AROME-Medalp domain, the improvement of AROME over ARPEGE is obvious. The differences between AROME-France and AROME-Medalp are smaller, but the bias is reduced with AROME-Medalp: temperatures are warmer during the day and colder at night. The cold bias in mountain areas is also reduced with AROME-Medalp. The differences between AROME-France and AROME-Medalp are linked to a finer vertical resolution, a first level close to the surface and the modification of the Richardson number.

In the AROME-Paris domain, the differences are less significant. The cold bias is reduced with AROME-Paris during the day, as is the warm bias during night. The impact of the various surface modifications has been quantified. ECOCLIMAP-SG and OSM increase the temperature in the city and tend to increase the warm bias at night over Paris. Activating the GARDEN option in the TEB scheme and increasing the thermal capacity of vegetation tends to lower the temperature in the city and reduce the warm bias at night.

#### 3.3 Wind scores

Wind scores at ten meters were calculated over the same period as temperature scores and are presented in figure 9. There is no improvement with AROME-Paris as far as wind is concerned. On the AROME-Medalp

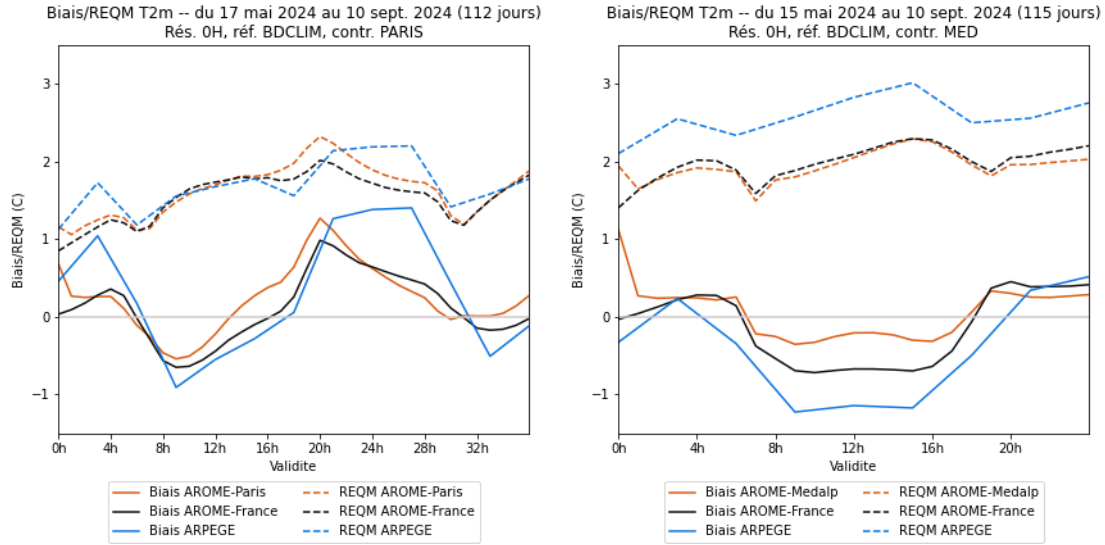


Figure 8: T2m scores computed between May 17, 2024 and September 10, 2024 on AROME-Paris domain (on left) and AROME-Medalp domain (on right) for ARPEGE (blue), AROME-France (black) and AROME-500m (orange).

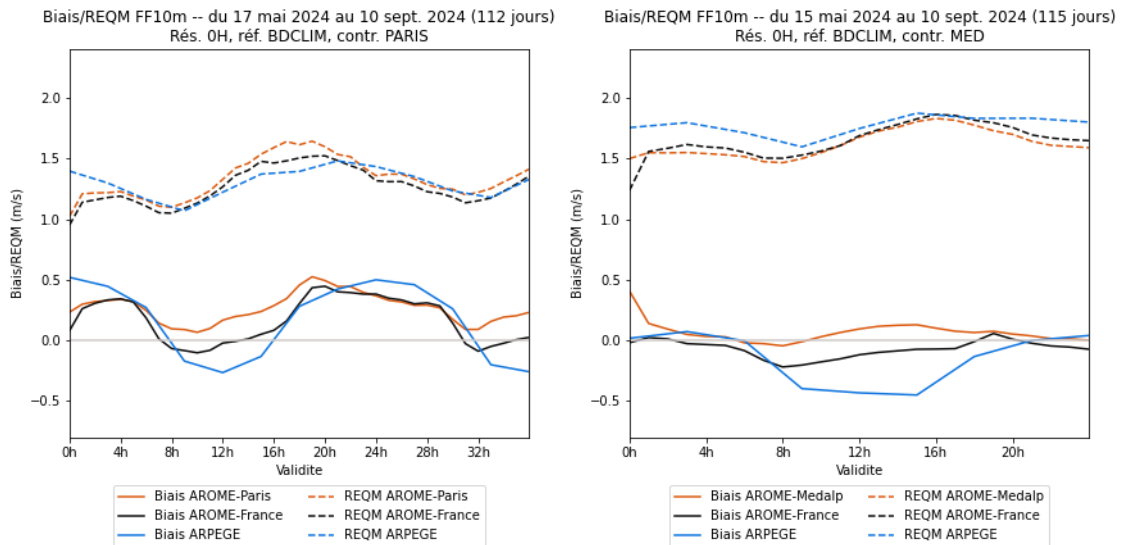


Figure 9: FF10m scores computed between May 17, 2024 and September 10, 2024 on AROME-Paris domain (on left) and AROME-Medalp domain (on right) for ARPEGE (blue), AROME-France (black) and AROME-500m (orange).

domain, wind scores are better with AROME-Medalp than with AROME-France for all lead times. This improvement may be linked to the better representation of orography in AROME-Medalp.

### 3.4 Convective rain scores

Figure 10 shows scores over the AROME-Medalp domain of the size, number and mean rainfall of convective cells. The AROME-500m cells are too small and too numerous compared to observations and compared to AROME-France forecasts. Mean rainfall are relatively unchanged between AROME-France and AROME-500m and are fairly close to observations.



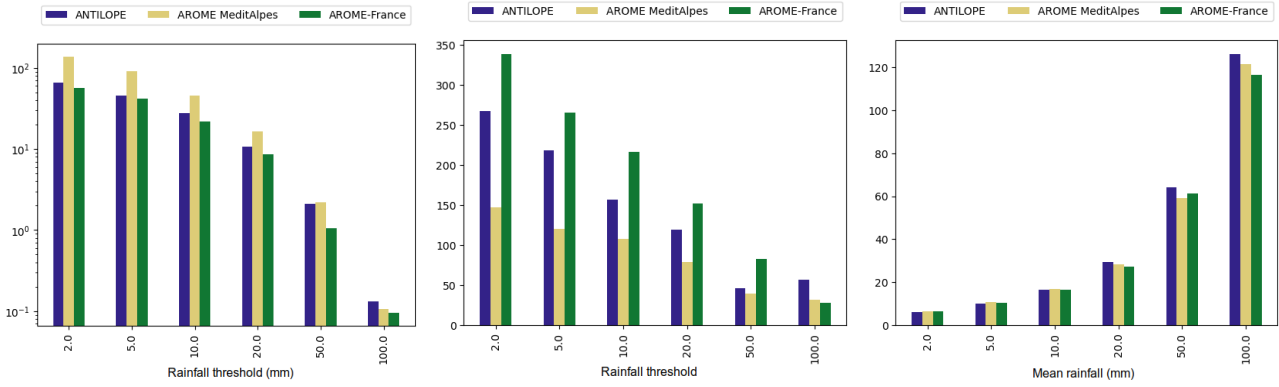


Figure 10: Number of convective cells (on left), size of convective cells (on center) and mean 3h cumulative rainfall below convective cells (on right), Antilope observations in blue, AROME-MeditAlpes in yellow and AROME-France in green.

## 4 Case studies

### 4.1 October 17, 2024 - High precipitation on south east of France

The 17<sup>th</sup> October 2024 is a case of heavy rainfalls with a red alarm for "heavy rain and flooding" in the south east of France. Finally, it rained more than 400mm locally. Daily cumulative rainfalls forecast by AROME-France, AROME-MeditAlpes and observed are shown on figure 11. AROME-France well forecast the situation, but maximum precipitation for the day was a little too low (285 mm). AROME-MeditAlpes also had a good forecast, the maximum was at a good location and the maximum cumulative precipitation is greater (344mm).

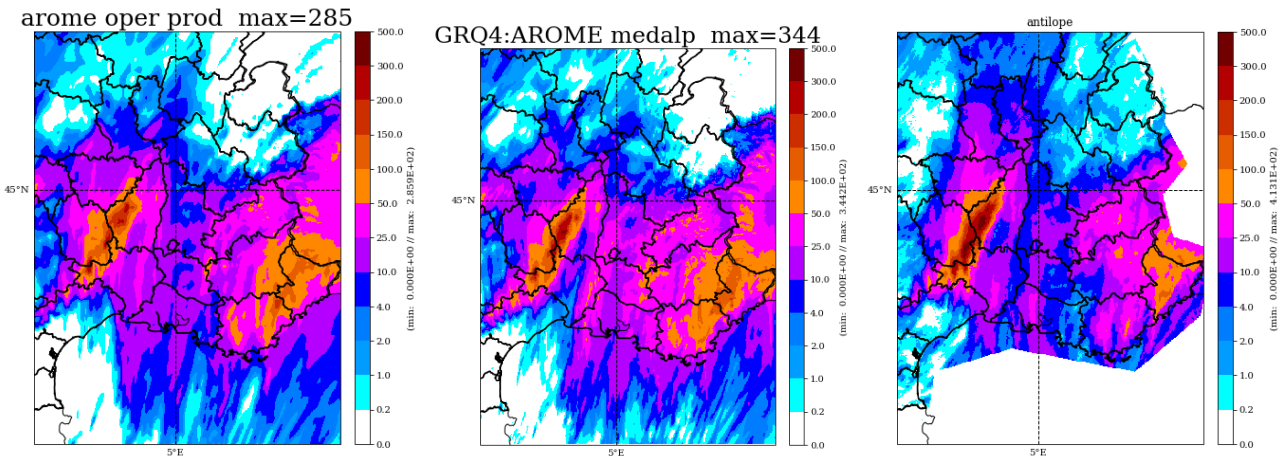


Figure 11: Daily cumulative rainfall the 17<sup>th</sup> October 2024 for AROME-France (on left), AROME-MeditAlpes (on center) and Antilope observations (on right).

### 4.2 August 25, 2024: strong urban heat island in Paris

For this study, we used observations collected during the 2024 summer in the city of Paris, during the PANAME measurement campaign (Lemonsu et al., to be submitted).

The August 25 is a classic summer day with little wind and a few cumulus clouds. The air mass is relatively

cool, with maximum temperatures in central Paris not exceeding 25 °C. At night, a strong Urban Heat Island (UHI) develops. The UHI is calculated by taking the difference in temperature between a station in the town (Place Vendome) and a station in the countryside (Melun station).

The UHI at 5h UTC observed and forecast by AROME-France and AROME-Paris is given in table 2. AROME-Paris gives a very good view of the UHI, with a gradient close to that observed, even if forecast temperatures are cooler than those observed. In AROME-France, the gradient is too low. The town temperature is close to AROME-Paris, but countryside temperature is too hot.

Table 2: Observed and forecast temperatures by AROME-France and AROME-Paris for August 24, 2024 0000 UTC for August 25, 2024 at 0500 UTC.

	T(Place Vendome)	T(Melun)	UHI
Observations	16.78 °C	9.27 °C	7.51 °C
AROME-Paris	15.40 °C	8.59 °C	6.81 °C
AROME-France	15.47 °C	10.83 °C	4.64 °C

Figure 12 shows the temperature at two meters in AROME-France and AROME-Paris, around Paris area, a little earlier in the night, on August 24, 2024 at 23h UTC. Warmer zones in the north-western part of the domain are visible in AROME-Paris. They correspond to urban areas along the Seine river. These areas do not appear in the AROME-France forecasts, which are much more homogeneous. The parks also stand out clearly in the AROME-Paris forecasts, even small parks.

The AROME-500m forecasts seem more realistic, but there are not enough observations to compare with the AROME-Paris forecasts and validate or not these heterogeneities.

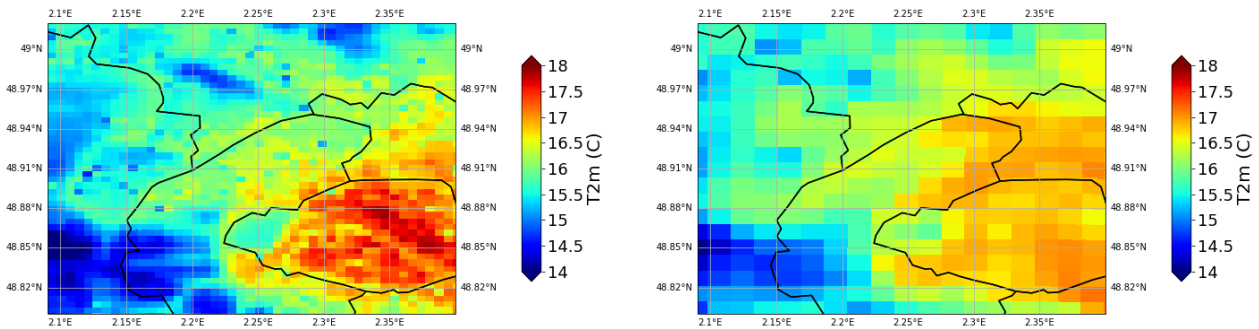


Figure 12: Temperature at two meters around Paris for August 24, 2024 23h UTC forecast by AROME-Paris on the left and AROME-France on the right of August 24, 2024 R00 UTC.

### 4.3 August 1, 2024 and August 30, 2024 - Convective cases

The 1<sup>st</sup> and the 30<sup>th</sup> August 2024 are two convective cases. The first is a free convective case, the second is a convective case with synoptic forcing. Hourly convective rainfall associated to these cases are shown on figure 13.

In the free convective case, AROME-Paris tends to forecast a lot a little cells, more numerous than in AROME-France. This result is consistent with the convective rain scores shown previously: AROME-500m tends to forecast more numerous and smaller cells than AROME-France.

In the forcing case, rainfall forecast by AROME-Paris are really close to those forecast by AROME-France. It is true in all type of forcing situation (convective like here, frontal, etc.).

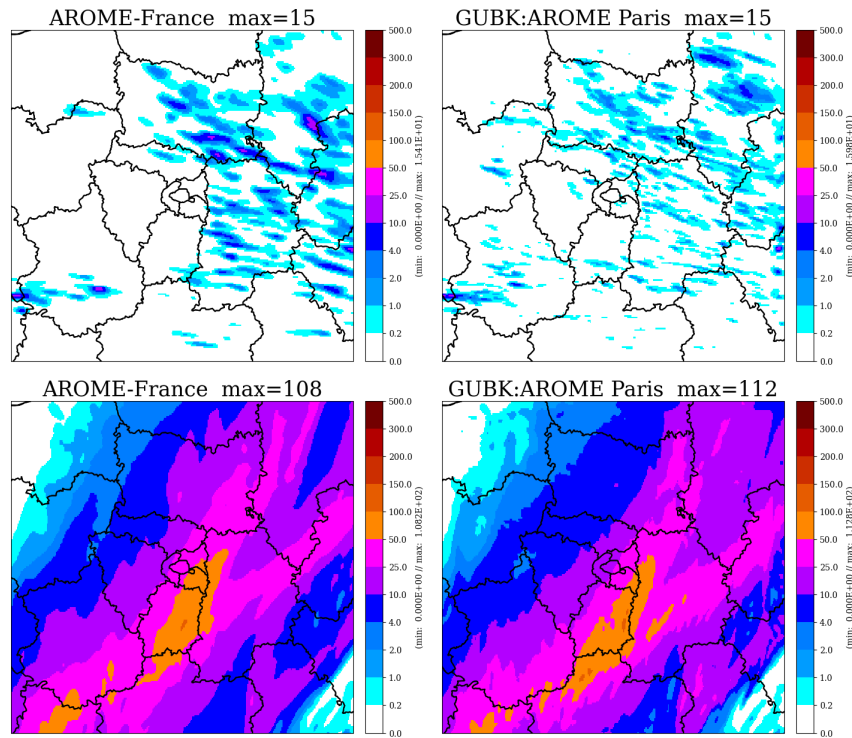


Figure 13: One hour cumulative rainfall the 1<sup>st</sup> August 2024 between 16h and 15h UTC (on top) and 24h cumulative rainfall the 30<sup>th</sup> August 2024 (on bottom), forecast by AROME-France (on left) and AROME-Paris (on right) from 0h UTC run of the day.

## 5 Conclusions

AROME-Paris and AROME-Medalp, two new Météo-France AROME configurations, were presented. They cover two domains, one around Paris and one around the South East of France and the Alps. This configurations are based on AROME-France operational configuration with some specific settings on the surface, dynamics and physics. Surface databases used are finer and more recent, vertical grid is finer mainly in the first levels above the ground and fog droplet deposition was activated.

Case studies show differences between AROME-France and AROME-500m forecasts:

- The fields are more heterogeneous, with greater detail. Urban areas and parks stand out clearly. These details, which seem more realistic, are however difficult to verify with the observation network available.
- The precipitation fields in the forced situations are very close to the precipitation fields in the coupling model.
- In a convection situation without synoptic forcing, the cells formed in AROME-500m are smaller and more numerous.
- In the event of heavy precipitation, maximum values are generally higher in AROME-500m.

However, it is difficult to demonstrate the added value of increased horizontal resolution on average. Scores are often neutral or weakly positive. It seems that increasing horizontal resolution does not automatically improve the model. The contribution of AROME-500m compared to AROME-France is more pronounced in the Medalp domain, but this is due to the improved relief. For the Paris domain, the question of domain size arises: perhaps a larger domain would improve results.

There is also the question of a cycling surface analysis. Here, forecasts are initialized from the AROME-France surface analysis, although many modifications have been made to the surface databases for the AROME-500m configuration. A specific surface analysis at AROME-500m would certainly be beneficial and would allow us to take full advantage of these new surface options.

## 6 Acknowledgments

Thanks to everyone involved in the AROME-500m working group for all their work on these new configurations. Thanks also to COMPAS/COM for the scores calculated on AROME-Paris and AROME-Medalp.

## 7 References

- Antoine, S., R. Honnert, Y. Seity, B. Vié, F. Burnet, and P. Martinet, 2023: Evaluation of an improved AROME configuration for fog forecasts during the SOFOG3D campaign. *Weather and Forecasting*, <https://doi.org/10.1175/WAF-D-22-0215.1>.
- Brousseau, P., Y. Seity, D. Ricard, and J. Léger, 2016: Improvement of the forecast of convective activity from the AROME-France system. *Quarterly Journal of the Royal Meteorological Society*, 142 (699), 2231–2243, <https://doi.org/10.1002/qj.2822>.
- Carrer, D., Meurey, C., Ceamanos, X., Roujean, J.L., Calvet, J.C., Liu, S., 2014 : Dynamic mapping of snow-free vegetation and bare soil albedos at global 1km scale from 10-year analysis of MODIS satellite products. *Remote Sensing of Environment*, <https://doi.org/10.1016/j.rse.2013.08.041>.
- Geoclimate, <https://joss.theoj.org/papers/10.21105/joss.03541>.
- Hengl, T., et al., 2017 : SoilGrids250m: Global gridded soil information based on machine learning. *PLoS one*, <https://doi.org/10.1371/journal.pone.0169748>.
- Lemonsu, A., Masson, V., Shashua-Bar, L., Erell, E., and Pearlmutter, D., 2012: Inclusion of vegetation in the Town Energy Balance model for modelling urban green areas, *Geosci. Model Dev.*, 5, 1377–1393, <https://doi.org/10.5194/gmd-5-1377-2012>.
- Lemonsu A., S. Barrau, J. Capo, J. Céspedes, S. Dahech, C. de Munck, J-C. Dupont, V. Dupuis, J-C. Etienne, O. Garrouste, M. Goret, M. Haeffelin, P. Keravec, S. Kotthaus, M. Madelin, P. Martinet, V. Masson, T. Nagel, J. Price, J-F. Ribaud, M. Rivollet, G. Roberts, A. Roy, V. Unger, S. Wallois, R. Wilson, J. Wurtz. Multi-scale study of urban-atmosphere interactions in the Paris region (France) in the framework of the PANAME experiment, *Bulletin of the American Meteorological Society*, to be submitted.
- Masson, V, 2000: A Physically-Based Scheme For The Urban Energy Budget In Atmospheric Models. *Boundary-Layer Meteorology* 94, 357–397. <https://doi.org/10.1023/A:1002463829265>.
- Mazoyer, M., C. Lac, O. Thouron, T. Bergot, V. Masson, and L. Musson-Genon, 2017: Large eddy simulation of radiation fog: impact of dynamics on the fog life cycle. *Atmospheric Chemistry and Physics*, 17 (21), 13 017 – 13 035, <https://doi.org/10.5194/acp-17-13017-2017>.
- Munier, S., et al., 2018 : Satellite leaf area index: Global scale analysis of the tendencies per vegetation type over the last 17 years. *Remote Sensing*, <https://doi.org/10.3390/rs10030424>.
- Seity, Y., P. Brousseau, S. Malardel, G. Hello, P. Bénard, F. Bouttier, C. Lac, and V. Masson, 2011: The AROME-France Convective-Scale Operational Model. *Monthly Weather Review*, 139 (3), 976–991, <https://doi.org/10.1175/2010MWR3425.1>.

# Towards 3D turbulence modelling in AROME at hectometric resolution : Sensitivity in stable regime and complex terrain

Léo Rogel, Fabrice Voitus, Eric Bazile, Rachel Honnert

December 2, 2024

## 1 Context

It is now well established that increasing the spatial resolution of numerical weather prediction models requires to revisit the physical parameterizations used and the validity of their constitutive assumptions below the kilometer scale. This need stems from the fact that, among other elements, the effective resolution of operational models is closer to that of the "grey zone" of convective boundary layer phenomena (Honnert et al. 2020; Wyngaard 2004). Until now, these parameterizations have generally been calibrated and validated at kilometer, if not lower, resolutions. The requirement to revisit parameterizations of subgrid fluxes includes more specifically the parameterization of turbulent fluxes. Here, by turbulent fluxes we mean the subgrid fluxes representing transfer of kinetic energy from large to small dissipative scales by the non-linear cascade mechanism. This flux is traditionally associated with the concept of local turbulent mixing<sup>1</sup>, usually modeled by eddy-diffusivity schemes (also termed "K-gradient" modeling).

In AROME, the turbulence scheme used is the same than the 1D scheme implemented in the Meso-NH research model (Cuxart et al. 2000, hereafter CBR). A full description of the scheme can be found in the physics package documentation of the Meso-NH model. The scheme diagnoses turbulent fluxes using a prognostic equation for turbulent kinetic energy (TKE) and a diagnostic mixing length. The non-local mixing length formulation of Bougeault and Lacarrere (1989, hereafter BL89) is used in operations. In the 1D version of the scheme, horizontal homogeneity is assumed for the turbulence closure, which neglects horizontal gradients in the expressions of turbulent fluxes, in the TKE prognostic equation, as well as the horizontal divergence of fluxes in other prognostic variables evolution equations. This modeling is consistent with the paradigm of single column physics which is commonly used to parameterize physical processes in atmospheric models at mesoscale resolutions.

Conversely, a 3D turbulence formulation simply consists in retaining the terms neglected in the 1D approach. Such a 3D formulation is already implemented in the CBR scheme, with the aim to target LESs involving explicit representation of the developed turbulence on the numerical grid. As mentioned, recent increases in horizontal resolutions of NWP models lead to reconsider horizontal homogeneity which is assumed in 1D turbulence schemes. For intermediate "grey zone" resolutions that the new hectometric AROME systems start to reach, the need for turbulent horizontal diffusion has been established using Meso-NH simulations, particularly concerning the representation of shallow convection Honnert and Masson (2014) and deep convection regimes at 500m grid resolution (Verrelle et al. 2015).

However, implementing a 3D turbulence scheme in AROME is challenging in a variety of ways. One of the key issue is that the single column representation of turbulence parameterization, like that of other physical

<sup>1</sup>A complementary approach to parameterizing turbulence in the gray zone of convection, developed for example in Moeng (2014), belonging to the category of non-local mixing, is considered very important, but is not discussed here, out of a desire to circumscribe the discussion to 3D effects impacting local mixing.

parameterizations, is highly beneficial in terms of computation time. Firstly, independent columns enable a high level of horizontal parallelism within the code, which is exploited at various levels (MPI tasks, OpenMP threads, vector instructions), which does not require knowledge of the horizontal grid. On the contrary, computing horizontal gradients requires information related to the horizontal grid topology, which is not directly available from AROME physics. This was addressed in recent works by Honnert and El Khatib (2021), allowing the use of these quantities in the AROME physics package. Secondly, and more importantly, single-column turbulence physics allow the use of a stable numerical method, through the direct implicit solution of a tridiagonal system of relatively small size (equal to the number of vertical levels). Implementing horizontal turbulent diffusion in an operational model using large time steps, such as AROME, would open up new research questions concerning the numerical stability of horizontal diffusion terms, especially in complex terrain (Baldauf and Brdar 2016). We can therefore anticipate that new lines of research will open up regarding the implementation of such 3D parameterization within a model consisting of the same dynamics and code structure of AROME (large time step, optimized “cache-blocking” data-structures, ...), and subject to the same NWP operational constraints. The associated software developments can also be carried out in conjunction with other 3D effects under consideration for the physics parameterizations.

Therefore, a preliminary question to any attempt at implementation is what benefits can be expected from 3D turbulence modeling. This question is particularly relevant to the target scales of hectometric AROME configurations, regarding meteorological situations of high interest. In what follows, we present the progress of this work, which has focused on the pseudo-3D approach (presented below) and whose impact is studied on a stable case of a cold air pool in an Alpine valley. This case has been chosen in order to reproduce clearly identified defects of the model in mountainous regions, namely warm biases at the valley floor and poor representation of small scale circulations. A comparison is made on the same case with Meso-NH by activating the available 3D parameterization and varying the mixing length formulation. In conclusion, we outline the prospects informed by these sensitivity tests, particularly as regards the treatment of the boundary condition by the turbulence scheme.

## 2 Presentation of "pseudo-3D" parameterization

As a first approach to the study of 3D effects in the turbulence scheme used by AROME, an intermediate-complexity parameterization has been implemented in the model. This approach is based on Goger et al. (2018) as well as on Goecke and Machulskaya (2021). It consists in parameterizing the dynamic production term accounting for horizontal wind shear. This new horizontal shear production term (HSP) is then added to the dynamic production term derived from the 1D parameterization. In the following, this added term is referred to as "pseudo-3D" when it is used in conjunction with the 1D scheme, to distinguish it from the complete 3D parameterization that will also be used in section 3.

### 2.1 Pseudo-3D parameterization of the dynamic turbulent production

We are interested in the parameterization of the horizontal part of the dynamic production term  $P_h$  in the TKE equation, denoted:

$$P_h = \sum_{i,j \in [1,2]} -\overline{u'_i u'_j} \frac{\partial U_i}{\partial x_j} \quad (1)$$

where  $U_i$  for  $i \in [1, 2]$  are the horizontal wind component and  $\overline{u'_i u'_j}$  for  $(i, j) \in [1, 2]$  are the horizontal turbulent stress components, expressed in the cartesian basis. Following Goecke and Machulskaya (2021), a first approximation is made by assuming that the  $P_h$  term represents turbulence forcing from a two-dimensional plane flow, where the horizontal part is considered independently separated from the vertical part. Following this hypothesis, horizontal analogues of the turbulent wind fluxes  $\overline{u'_i u'_j}$  are expressed as:



$$\left(\overline{u'_i u'_j}\right)_h = e_h \delta_{ij} - \frac{2C_h}{C_{pv}} e_h^{1/2} L_h \left( S_{ij} - \frac{1}{2} \delta_{ij} S_{kk} \right) \quad (i, j \in [1, 2]) \quad (2)$$

Where  $e_h = 0.5(\overline{u'^2} + \overline{v'^2})$  is a new unknown and represents the horizontal analogue of the TKE,  $L_h$  is a horizontal length scale, and  $S_{ij}$  is the strain rate tensor. The coefficients  $C_h$  and  $C_{pv}$  are determined according to the closure of presso-correlations, so as to be consistent with the two-dimensional flow assumption. The production term  $P_h$  is obtained by multiplying (2) with  $\partial_{x_j} U_i$ . A second hypothesis is made by assuming equilibrium between HSP and an horizontal analogue for the dissipation:  $P_h = C_\varepsilon e_h^{3/2} / L_h$ , leading to the solution of a quadratic equation for the quantity  $\sqrt{e_h}$ . After discarding the negative solution, the solution is fed back into the equilibrium expression for horizontal production:

$$P_h = C_\varepsilon \frac{e_h^{3/2}}{L_h} = L_h^2 \sqrt{C_{mh}^3 / C_\varepsilon} \left( \sqrt{\text{DEF}^2 + C_1^2 \text{DIV}^2} - C_1 \text{DIV} \right)^3 \quad (3)$$

With DIV representing the horizontal wind divergence, and DEF representing the horizontal deformation of the flow, respectively defined by:

$$\text{DIV} = \frac{\partial U_1}{\partial x_1} + \frac{\partial U_2}{\partial x_2} \quad \text{and} \quad \text{DEF}^2 = \left( \frac{\partial U_1}{\partial x_1} - \frac{\partial U_2}{\partial x_2} \right)^2 + \left( \frac{\partial U_2}{\partial x_1} + \frac{\partial U_1}{\partial x_2} \right)^2 \quad (4)$$

The coefficients  $C_{mh}$  and  $C_1$  depend on  $C_h$ ,  $C_{pv}$  and  $C_\varepsilon$ . From a practical standpoint, this formulation guarantees the positivity of the horizontal production term, which is not necessarily verified for the full 3D term in the CBR scheme. This derivation is performed without assumptions on the expression of the horizontal length scale.

## 2.2 Horizontal length scale formulation

Various horizontal scale formulations can be found in the literature. In a first approach, following Goger et al. (2018), the length scale of Smagorinsky (1963) was used:

$$L_S^{(0)} = c_S \sqrt{\Delta x \Delta y} \quad (5)$$

with  $c_S = 0.2$ . However, preliminary tests have shown that this length scale formulation leads to strong HSP values. It can even lead to numerical instabilities in AROME linked to the explicit HSP formulation within the TKE scheme. This suggests to limit this length scale. Firstly, a minimisation relative to the orography is used, depending on the slope at the point considered by the orography gradient  $z_s$ :

$$L_S^{(1)} = c_S \sqrt{\Delta x \cos \alpha_x \Delta y \cos \alpha_y} \quad (6)$$

with  $\alpha_x = \arctan \partial_x z_s$  and  $\alpha_y = \arctan \partial_y z_s$ . Equation (6) stems from the intuition that the orography slope at the grid scale reduces the horizontal length of turbulent eddies that the pseudo-3D parameterization aims to represent. As a further step, a dependence of the length scale on the flow is included. The formulation of Wang et al. (2021) has been adopted, which depends on horizontal wind gradients and resolved wind:

$$L_W = \left( \frac{\Delta_0}{\sqrt{\Delta x \Delta y}} \right)^\alpha \frac{\sqrt{U^2 + V^2}}{[(\partial_x V)^2 + (\partial_y U)^2]^{1/4} [(\partial_x U)^2 + (\partial_y V)^2]^{1/4}} \quad (7)$$

where  $U$  and  $V$  are the horizontal wind components, and with  $\alpha = 1.5$  and  $\Delta_0 = 500\text{m}$ . The direct dependence of this length scale formulation on wind magnitude should be of interest for stable flow regimes with weak

wind, such as the one presented below, where more mixing is expected in locations where wind circulations are represented. On the contrary the reduction of the length scale with respect to horizontal wind shear can intuitively be linked to the deformation of horizontal eddies by horizontal shear. The final expression of the retained horizontal length scale is obtained as a minimization of the two previously defined scales:

$$L_h = \min [L_W, L_S^{(1)}] \quad (8)$$

In order to ensure numerical stability, the pseudo-3D parameterized HSP is limited. In future work, we plan to specify a better method for this limiter, in association with improved horizontal length scales formulations compared to the one presented here. For now, as a first approach, this new term is limited directly<sup>2</sup> with  $P_h < \varepsilon$ .

### 3 Case study : Cold Air Pool

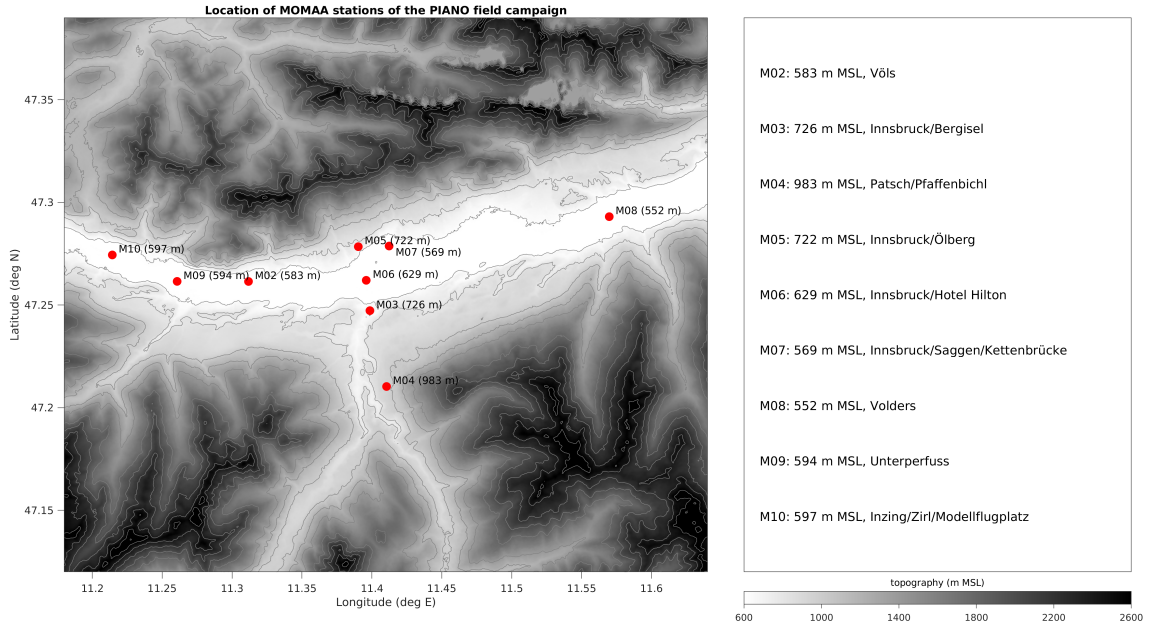


Figure 1: Inn valley orography and localisation of in-situ 2m temperature mobile station observations. Figure and data from the PIANO reasearch project can be found at <https://zenodo.org/records/4745957>.

In order to analyze the impact of this new term, and more generally the expected impact of using the 3D scheme at hectometric resolutions, an experiment in complex terrain was carried out on a cold air pool stable case in the Inn valley for which in-situ data from the PIANO observation campaign (Haid et al. 2020) are available.

#### 3.1 Case presentation

The case of cold air pool on the night of 15 to 16 October 2017 between 0000 and 0600 UTC was reproduced with the AROME model as well as the Meso-NH model, both used at an horizontal grid resolution of  $\Delta x = 500\text{m}$ .

<sup>2</sup>A limiter in the form  $P_h < \frac{L_v}{L_h} \varepsilon$ , where  $L_v$  is the mixing length diagnosed from the 1D scheme, would be both less restrictive and more consistent with the horizontal equilibrium assumption. However, we think that the approach used here does not change the qualitative discussion of the results which will be carried out in section 3.

The observations used to evaluate the models originate from the PIANO measurement campaign, with 9 mobile temperature stations providing time evolution of temperature at 2m above ground, and at a sampling frequency of 1 minute. The location of these stations is shown in Figure 1. They are all situated on the valley floor, except for station M04 which is located at higher altitudes. Station M06 was excluded from the observation dataset because it is located on a building at an altitude of 50m AGL, unlike the other observations which are actually 2m above ground level. In addition to stations data, a radiosounding launched at 0215 UTC from the Innsbrück airport (roughly located to the east of station M02) is also used. This radiosounding shows a low layer jet with a core located between 500m and 800m AGL, as well as a temperature inversion layer located at an altitude of 1000m AGL. This radiosounding is used to evaluate the vertical structure of the wind and temperature fields obtained by the models within the valley.

Two experiments were carried out with the AROME model: the first with the BL89 mixing length and the 1D scheme configuration (hereafter 1D BL89), as in operations, and the second including the pseudo-3D parameterization presented in the previous section. The Meso-NH experiments also include a sensitivity test on 1D/3D scheme, and another test on the use of the Deardorff (1973) formulation for the mixing length. For both models, the reference configuration is 1D BL89. Both models share the same vertical grid resolution, which is that of the current operational configuration and consisting of 90 levels with 40 levels below 3000m AGL, the first level being 5m above ground level.

The two models are coupled to an AROME experiment with an horizontal resolution of 1.3km, which in turn is coupled to the ARPEGE forecast. All experiments are initialized on October 15 at 1200 UTC and produce a 24-hour forecast, up to 1200 UTC the following day. For AROME we have  $\Delta t = 30s$  and for Meso-NH  $\Delta t = 2s$ . The explicit horizontal numerical diffusion in Meso-NH has been calibrated in order to have the same intensity as that used in the AROME semi-implicit solver. Also, accounting for sensitivity to the dynamics of the model seems relevant in this study, insofar as we are examining two models with very different dynamical cores. Without being able to control in detail the differences linked to numerical treatments, we expect to observe the same impact of the pseudo-3D in both models. The parameterization of shallow convection calibration has been modified (taking XCMF=0.03 instead of 0.06) in line with the increased horizontal resolution, although in this particular stable case, sensitivity tests indicate that this modification has a negligible impact.

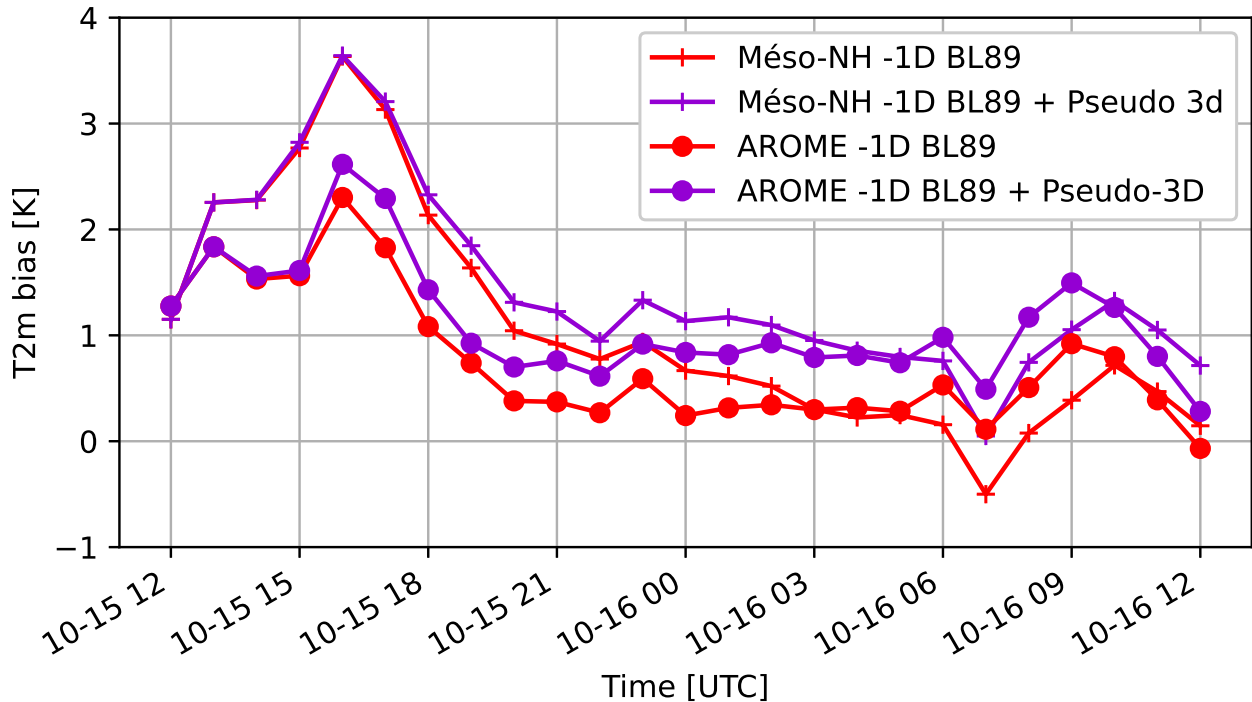


Figure 2: Mean T2m bias for AROME and Meso-NH sensitivity experiments on pseudo-3D parameterization

### 3.2 Forecast scores

Scores have been used to compare the different AROME and Meso-NH experiments with observations. Two evaluation scores are computed: the average bias and the root mean square error (RMSE), calculated between observations and the closest model point at each time interval. When using these data, and especially in complex terrain for the 2m temperature comparison between model and observations, a classical height correction is applied by reducing temperatures at sea level, following the adiabatic gradient of  $-6.5/\text{km}$  of the standard atmosphere.

### 3.3 Results

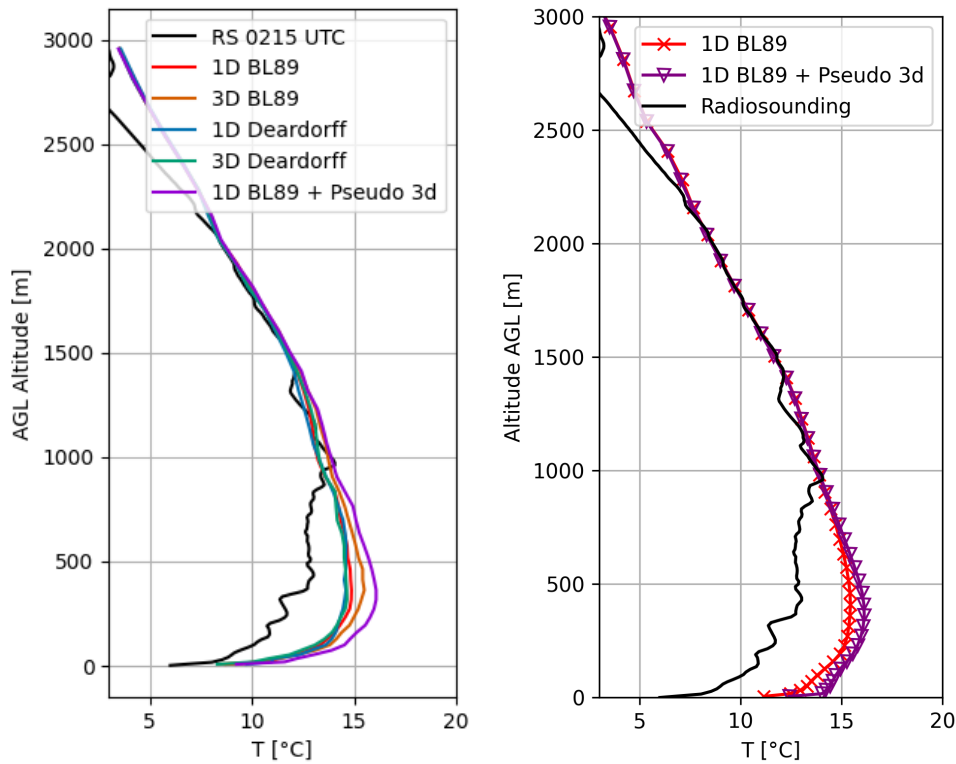


Figure 3: Temperature profiles comparison of radiosounding data and nearest point model temperature profile. Left : Meso-NH. Right : AROME

In general, the two models correctly capture the temperature evolution recorded by the stations (not shown here). Figure 2 shows 2m temperatures mean biases between stations and the nearest model points, for AROME and Meso-NH. Both models show a warm bias on average over the whole night period. There is less bias in AROME relative to the observations, except in the period of transition to the diurnal regime after 0500 UTC. Initial temperatures for both models remain inconsistent with those measured, for reasons that were not yet clearly identified. In both models, a significant error is also observed from 1500 - 1600 UTC, which corresponds to the period of transition to the night-time regime, with a rapid decrease in temperature during this period. This may be linked to a slower cooling rate in the models during this period, by examining the time series at each of the stations. The pseudo-3D parameterization leads to a significant increase in the mean warm bias from 2100 UTC, of the same behaviour and magnitude in both models. These results confirm that despite the residual differences in the dynamics between AROME and Meso-NH, the pseudo 3D parameterization has the same impact in both models.

The comparison of temperature and wind profiles (Figures 3 and 4 respectively) from the two models with

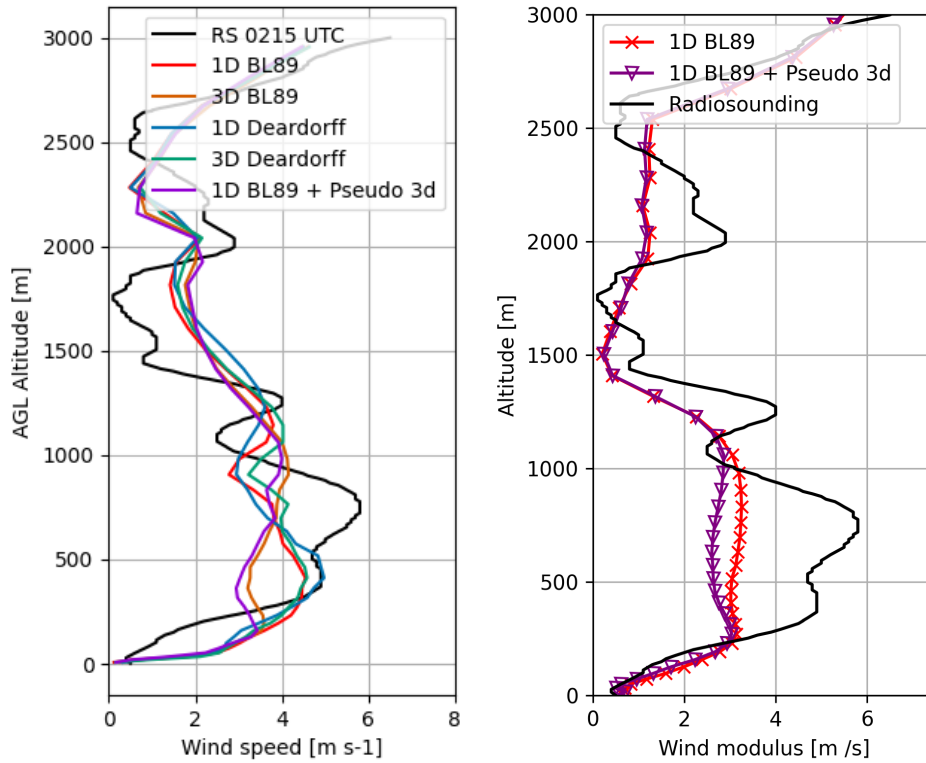


Figure 4: Same as Figure 3, but for wind magnitude.

those from the radiosounding provides more insight into the sensitivity of the cold air pool event on turbulence parameterization. These profiles are also computed from the model closest point to the observation site. Firstly, the temperature profiles (Figure 3) show that the inversion layer located at 1km AGL is not captured, neither by AROME nor by Meso-NH. Below this altitude, both models display a marked warm bias over the entire layer between the ground and the inversion. The two models also differ on the first levels near the ground, with higher temperatures in AROME than in Meso-NH.

Regarding the wind profiles represented in Figure 4, the core of the jet does not seem to be represented by AROME, unlike Meso-NH with the 1D BL89 reference configuration. On the other hand, in Meso-NH, we note that the model overestimates the wind intensity in the first levels close to the ground. More particularly, the wind profiles represented in Meso-NH show a relatively large variability depending on the turbulence scheme parameters used in this sensitivity study. For example, the use of the Deardorff length in the 1D scheme gives an intensity in the core of the jet that seems most consistent with the observation. Still on the wind profiles, the use of the 3D parameterization of Meso-NH has the effect of reducing the intensity of the low-level jet, almost to the point of entirely smoothing the wind over the vertical when looking at the 3D BL89 experiment. On the other hand, if we look at the sensitivity of the temperature profiles to the use of the 3D scheme, we see that it has a different impact depending on the mixing length formulation used. In the case where BL89 is used, the 3D scheme leads to a warming whereas this leads to a slight cooling when using the Deardorff (1973) scale. This difference in behaviour remains to be explained in more detail, but a first inspection of the heat flux balances in Meso-NH (not shown) suggests that BL89 leads to an increase in vertical mixing with the 3D scheme in this case, whereas the 3D scheme with Deardorff leads to a decrease in vertical mixing.

As noticed above on Figure 2, the impact of the pseudo-3D term is invariably the same in both models, leading to a marked warming of the temperature profile and a reduction in wind intensity. This behaviour is consistent with the design of this term, at it can only increase TKE, and hence vertical mixing. Furthermore, the wind intensity obtained in Meso-NH with 3D BL89 and pseudo-3D is remarkably similar to the intensity of the profile obtained in AROME. This suggests that the wind deficit in the forecast model may be due to excess vertical

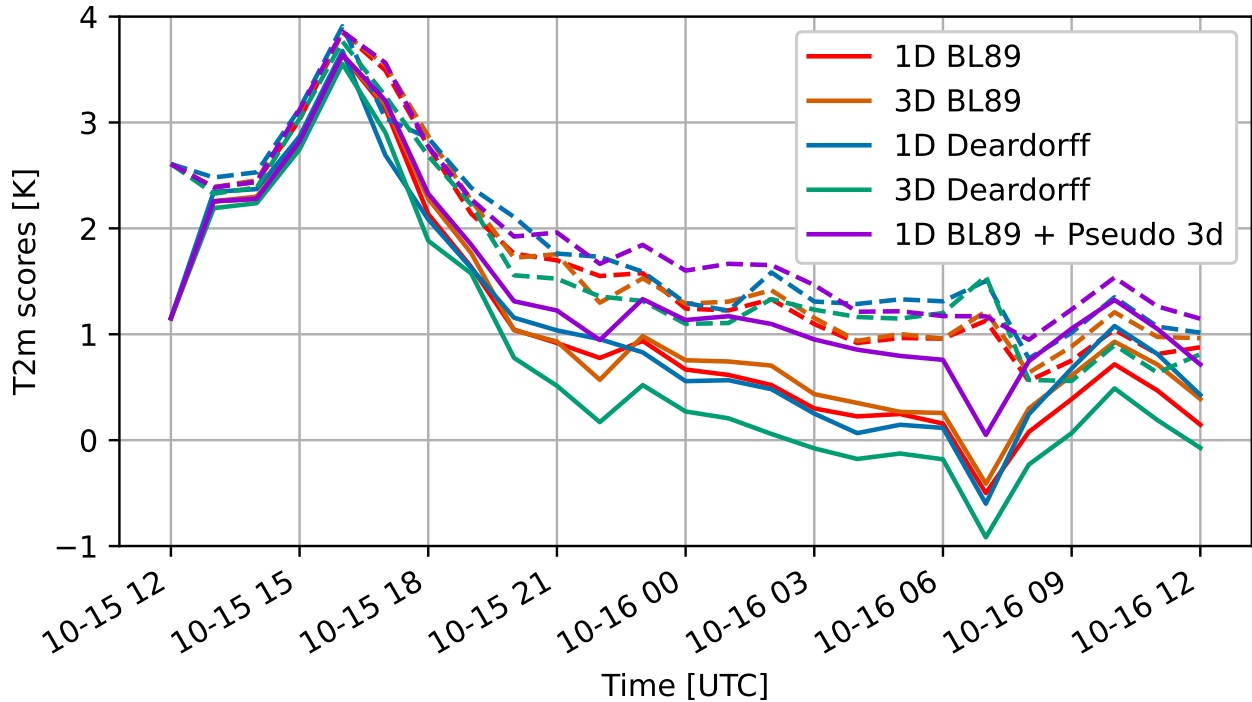


Figure 5: 2m temperature scores for Meso-NH experiments. Solid lines : mean bias ; dashed lines : RMSE.

mixing. Put in another way, we can ask ourselves whether reducing the vertical mixing on this case in AROME would improve the representation of the wind. This last point is crucial for high-resolution forecasting systems such as hectometric AROME, as it is well established that better accounting of wind and small scale circulations, especially in complex terrain, would also improve the representation of temperature fields through more realistic fine-scale circulations and transport phenomena. This will therefore be subjected to particular attention in the future.

Figure 5 shows mean bias and RMSE, for all the Meso-NH experiments. Once again, we see the large model errors around 1700 UTC in the transition regime to the night-time situation. We also note the clear sensitivity of these experiments to the settings of the turbulence scheme from 2000 UTC onwards. The use of the 3D scheme with the Deardorff mixing length leads to a stronger cooling of T2m, which explains the reduction of the warm bias. Conversely, using the 3D scheme with the BL89 length does not correct this mean warm bias. We again notice the dependence of the 3D scheme impact on the formulation of the mixing length. Finally, the RMSE scores do not show a significant improvement in the simulation with respect to the tested scheme options.

## 4 Conclusions and perspectives

Sensitivity experiments were conducted on a cold air pool case using the AROME and Meso-NH models. In these experiments, we highlighted the sensitivity of the jet representation and low-level temperatures to the parameters of the turbulence scheme, with an increase in turbulence mixing leading to a deterioration in the wind jet vertical structure and 2m temperature forecasts. The comparison between the two models suggests that AROME overestimates vertical mixing, associated with a too much damped jet core. The sensitivity tests carried out in Meso-NH also highlight the strong dependence of vertical mixing on the mixing length formulation. This is not surprising since the diagnostic formulation of the length scale is central to the design of the scheme. These results therefore suggest that the BL89 formulation is not suitable when including, generally speaking, 3D effects in high-resolution stable cases. This is in line with its non-local formulation, which is not necessarily suitable



as fine-scale circulations begin to be explicitly represented on the numerical grid (Honnert et al. 2011). The finding of excess mixing parameterized by the BL89 length scale also seems to be reinforced by the difference in behaviour of the full 3D scheme between BL89 and Deardorff. These tests also make it possible to distinguish between the impacts of a 3D scheme and pseudo-3D parameterization, the latter leading, as expected, to an increase in vertical mixing which is here detrimental to the representation of this cold air pool case. More improvements concerning this term are thus needed, specifically regarding the diagnosed horizontal length scale formulation, so that it does not degrade stable cases representation such as the one discussed here, and improves other flow regimes where vertical mixing is diagnosed to be too low.

The tests carried out show a potential improvement in the representation of the vertical structure of the jet and the temperature at 2m in the Meso-NH experiments, by adopting the 3D turbulence scheme with the Deardorff length. However, the intensity of the initial cooling between 1800 UTC and 2100 UTC is poorly represented by the models. This poor representation during the transition from the diurnal to the nocturnal regime, as well as its impact on the remainder of the cold air pool event, remains to be explained. Preliminary leads for this investigation could include the representation of surface parameters and their related impact on the soil thermal capacity.

Finally, a deeper analysis of the code differences between AROME and Meso-NH for the coupling between surface and the turbulence scheme has shown a different treatment for the slope. In AROME, all turbulent fluxes parameterized by the surface package are applied in the vertical direction of the model. In Meso-NH, this surface flux is first expressed in a basis normal to the surface, before being reprojected within the turbulence scheme along the vertical and horizontal directions. The approach used by Meso-NH, close to that proposed by Epifanio (2007), potentially has a non-negligible impact in the representation of wind in complex terrain, through a better representation of katabatic circulations, and therefore a more realistic transport of cold air from altitude to the valley. In order to better identify the deficiencies in the representation of these processes, we plan to use datasets with finer spatial coverage (Muschinski et al. 2021), which hopefully will allow to improve model evaluation and validation through the accounting of spatial variability in surface parameters and orography. However, the implementation needs to be adapted to AROME. Current developments now focus on the implementation and evaluation of this modification on slope winds and will be the object of the future work.

## References

- Baldauf, M. and S. Brdar (2016). “3D Diffusion in Terrain-Following Coordinates: Testing and Stability of Horizontally Explicit, Vertically Implicit Discretizations”. In: *Quarterly Journal of the Royal Meteorological Society* 142.698, pages 2087–2101. DOI: 10.1002/qj.2805.
- Bougeault, P. and P. Lacarrere (1989). “Parameterization of Orography-Induced Turbulence in a Mesobeta-Scale Model”. In: *Monthly Weather Review* 117.8, pages 1872–1890. DOI: 10.1175/1520-0493(1989)117<1872:POOITI>2.0.CO;2.
- Cuxart, J., P. Bougeault, and J.-L. Redelsperger (2000). “A turbulence scheme allowing for mesoscale and large-eddy simulations”. In: *Quarterly Journal of the Royal Meteorological Society* 126.562, pages 1–30. DOI: 10.1002/qj.49712656202.
- Deardorff, J. W. (1973). “Three-Dimensional Numerical Modeling of the Planetary Boundary Layer”. In: *Workshop on Micrometeorology, 1973*. Am. Meteorol. Soc.
- Epifanio, C. C. (2007). “A Method for Imposing Surface Stress and Heat Flux Conditions in Finite-Difference Models with Steep Terrain”. In: *Monthly Weather Review* 135.3, pages 906–917. DOI: 10.1175/MWR3297.1.
- Goecke, T. and E. Machulskaya (2021). “Aviation Turbulence Forecasting at DWD with ICON: Methodology, Case Studies, and Verification”. In: *Monthly Weather Review* 149.7, pages 2115–2130. DOI: 10.1175/MWR-D-19-0383.1.

- Goger, B., M. W. Rotach, A. Gohm, O. Fuhrer, I. Stiperski, and A. A. M. Holtslag (2018). “The Impact of Three-Dimensional Effects on the Simulation of Turbulence Kinetic Energy in a Major Alpine Valley”. In: *Boundary-Layer Meteorology* 168.1, pages 1–27. DOI: 10.1007/s10546-018-0341-y.
- Haid, M., A. Gohm, L. Umek, H. C. Ward, T. Muschinski, L. Lehner, and M. W. Rotach (2020). “Foehn–Cold Pool Interactions in the Inn Valley during PIANO IOP2”. In: *Quarterly Journal of the Royal Meteorological Society* 146.728, pages 1232–1263. DOI: 10.1002/qj.3735.
- Honnert, R., G. A. Efstathiou, R. J. Beare, J. Ito, A. Lock, R. Neggers, R. S. Plant, H. H. Shin, L. Tomassini, and B. Zhou (2020). “The Atmospheric Boundary Layer and the “Gray Zone” of Turbulence: A Critical Review”. In: *Journal of Geophysical Research: Atmospheres* 125.13, e2019JD030317. DOI: 10.1029/2019JD030317.
- Honnert, R. and R. El Khatib (2021). *First and Second Derivatives for Future Use in AROME Physics*. Research activities in Earth system modelling.
- Honnert, R. and V. Masson (2014). “What Is the Smallest Physically Acceptable Scale for 1D Turbulence Schemes?” In: *Frontiers in Earth Science* 2. DOI: 10.3389/feart.2014.00027.
- Honnert, R., V. Masson, and F. Couvreur (2011). “A Diagnostic for Evaluating the Representation of Turbulence in Atmospheric Models at the Kilometric Scale”. In: *Journal of the Atmospheric Sciences* 68.12, pages 3112–3131. DOI: 10.1175/JAS-D-11-061.1.
- Moeng, C.-H. (2014). “A Closure for Updraft–Downdraft Representation of Subgrid-Scale Fluxes in Cloud-Resolving Models”. In: *Monthly Weather Review* 142.2, pages 703–715. DOI: 10.1175/MWR-D-13-00166.1.
- Muschinski, T., A. Gohm, M. Haid, L. Umek, and H. C. Ward (2021). “Spatial Heterogeneity of the Inn Valley Cold Air Pool during South Foehn: Observations from an Array of Temperature Loggers during PIANO”. In: *Meteorologische Zeitschrift*, pages 153–168. DOI: 10.1127/metz/2020/1043.
- Smagorinsky, J. (1963). “General Circulation Experiments with the Primitive Equations : I. The Basic Experiment”. In: *Monthly Weather Review* 91.3, pages 99–164. DOI: 10/bhd6ks.
- Verrelle, A., D. Ricard, and C. Lac (2015). “Sensitivity of High-Resolution Idealized Simulations of Thunderstorms to Horizontal Resolution and Turbulence Parametrization”. In: *Quarterly Journal of the Royal Meteorological Society* 141.687, pages 433–448. DOI: 10.1002/qj.2363.
- Wang, W., B. Liu, L. Zhu, Z. Zhang, A. Mehra, and V. Tallapragada (2021). “A New Horizontal Mixing-Length Formulation for Numerical Simulations of Tropical Cyclones”. In: *Weather and Forecasting* 36.2, pages 679–695. DOI: 10.1175/WAF-D-20-0134.1.
- Wyngaard, J. C. (2004). “Toward Numerical Modeling in the “Terra Incognita””. In: *Journal of the Atmospheric Sciences* 61.14, pages 1816–1826. DOI: 10.1175/1520-0469(2004)061<1816:TNMITT>2.0.CO;2.

# Reducing the Nocturnal Warm Bias in C-LAEF 1k Simulations for Alpine Valleys

Daniel Deacu, Clemens Wastl and Christoph Wittmann

## 1 Introduction

C-LAEF 1k is a pre-operational, convection-permitting limited-area ensemble forecasting system developed by GeoSphere Austria. It employs the AROME model (version cy46t1) with a grid spacing of 1 km, an improvement over the 2.5-km grid spacing of the current operational C-LAEF system (Wastl et al. 2021). Another important change is the deactivation of the surface boundary layer scheme of Masson and Seity (2009) over the nature tile, where the ISBA land-surface model operates in force-restore mode. The scheme remains inactive over the sea, lake and urban tiles. However, despite these changes and additional adjustments to dynamics and physics parameters for increased resolution, a nocturnal warm bias persists in near-surface air temperature forecasts, particularly in Alpine valleys during winter. This note highlights several potential changes for upgrading C-LAEF 1k to reduce this bias. The experiments presented herein were conducted without applying the 2-m temperature correction from Meier et al. (2021), which is currently used in the pre-operational C-LAEF 1k.

## 2 Effect of enhancing the surface turbulent fluxes in stable conditions

Experiments with the control member of C-LAEF 1k, applying various adjustments to reduce the aforementioned warm bias, have indicated that increasing the surface turbulent heat flux in stable conditions has a beneficial effect in the Inn Valley (Austria). This can be achieved by lowering the maximum allowable value of the bulk Richardson number ( $Ri_b$ ) used in the calculation of the surface turbulent fluxes, which is controlled by the XRIMAX parameter in the model. XRIMAX is set to 0.2 in the current C-LAEF 1k configuration, whereas many AROME-based NWP systems within the ACCORD Consortium have used  $XRIMAX = 0$ . The latter setting corresponds to calculating the surface transfer coefficients for neutral stability conditions, characterised by  $Ri_b = 0$ , regardless of the bulk Richardson number value calculated under stable conditions. Most of these systems employed the surface boundary layer (SBL) scheme of Masson and Seity (2009), which introduces several additional levels below the model's lowest level. When the SBL scheme is activated, the surface turbulent fluxes are calculated using the atmospheric variables at the lowest SBL level, typically positioned approximately 0.5 meters above the surface. The  $XRIMAX = 0$  setting could then be justified by the assumption that stable conditions are near-neutral within the model's 0.5-m-thick surface layer (Masson and Seity, 2009).

The SBL scheme has been deactivated in C-LAEF 1k, where the lowest of the 90 model levels is approximately 5 m above the surface. Consequently, setting  $XRIMAX = 0$  can no longer be justified based on assumptions of near-neutral stability in the model's surface layer. However, this adjustment produced the greatest positive impact on the valley atmosphere under stable conditions with weak synoptic forcing in our experiments. The effect is an increase in surface transfer coefficients and, as a result, in surface turbulent fluxes. This results in a more accurate simulation of the stable boundary layer in the Inn Valley, producing a cooling effect that, in some cases, extends from the surface up to nearly the full depth of the valley, as confirmed by comparisons with observational data (not shown). It should be noted that capping the Richardson number at 0 is not ideal, as it may lead to unrealistically high surface fluxes under certain conditions and in specific regions. Nevertheless,

this approach seems to help compensate for processes that are either missing or inadequately represented at the grid scale, which are essential for accurate modelling of the stable boundary layer in Alpine valleys.

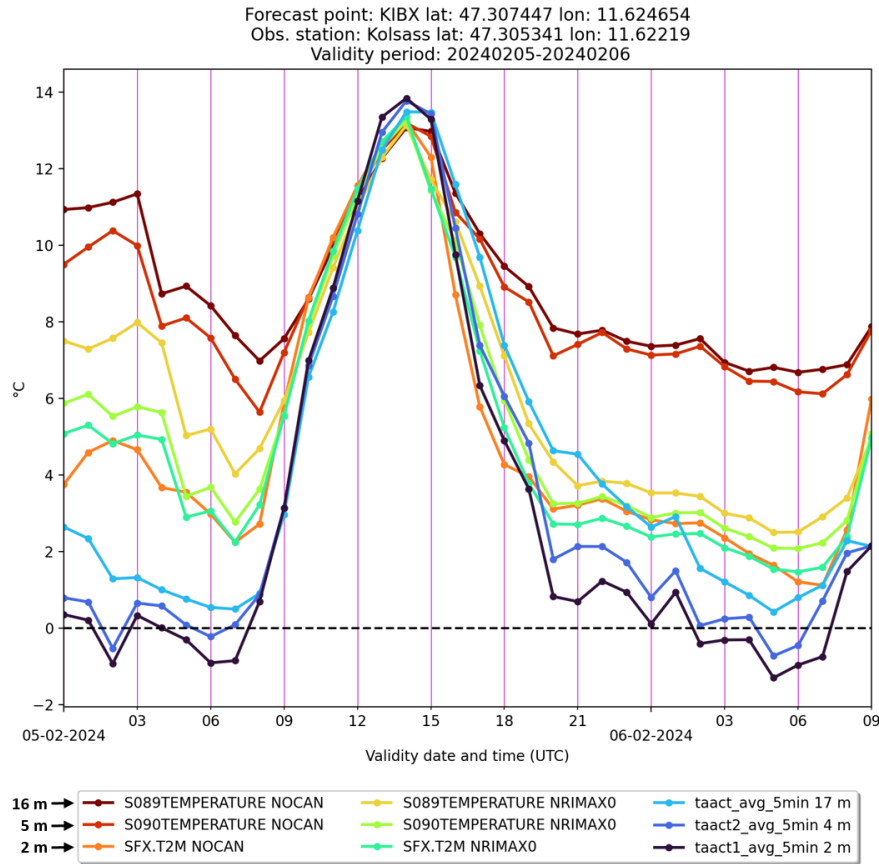


*Figure 1: Hourly air temperatures observed at the i-Box Kolsass station (located approximately 20 km east of Innsbruck) and simulated at the nearest grid point at different heights. The observation heights are 2, 4, and 17 m and the hourly observed temperatures are averages of 1-min observed temperatures over the preceding 5 min. Simulated temperatures at 2 m, the lowest model level (approximately 5 m) and the second-lowest model level (approximately 16 m) are shown for two forecast experiments, NOCAN and NRIMAX0.*

Figure 1 presents the hourly air temperatures at 2 m, the lowest model level (approximately 5 m) and the second-lowest model level (approximately 16 m) for two 33-hour forecast experiments initialised at 00 UTC 5 February 2024: NOCAN and NRIMAX0. The control member of C-LAEF 1k was run with  $\text{XRIMAX} = 0.2$  in the NOCAN experiment and  $\text{XRIMAX} = 0$  in NRIMAX0. In addition to this change, the initial conditions for the experiments were obtained from continuous data assimilation cycles that started seven days prior (at 00 UTC 29 January 2024) using the respective model configurations. The simulated temperatures were extracted at the grid point nearest to the i-Box Kolsass observation station (Rotach et al., 2017), situated in the Inn Valley at an elevation of 545 m MSL, approximately 20 km east of Innsbruck. The model's surface elevation at the grid point nearest to the i-Box Kolsass station is 584 m MSL. Hourly air temperatures observed at 2, 4, and 17 meters at the i-Box Kolsass station are also shown in Fig. 1.

While the 2-m air temperatures simulated in both experiments are comparable, the nocturnal temperatures at the two lowest model levels in NRIMAX0 are much closer to the temperatures observed at 4 and 17 m than those simulated in NOCAN. The increased cooling of the near-surface air in NRIMAX0 is due to stronger surface-atmosphere interaction simulated under stable conditions. Similar results were observed in the series of 3-hour temperature forecasts from the continuous data assimilation cycles that provided the initial conditions.

### 3 Effect of a modified version of the soil freezing scheme

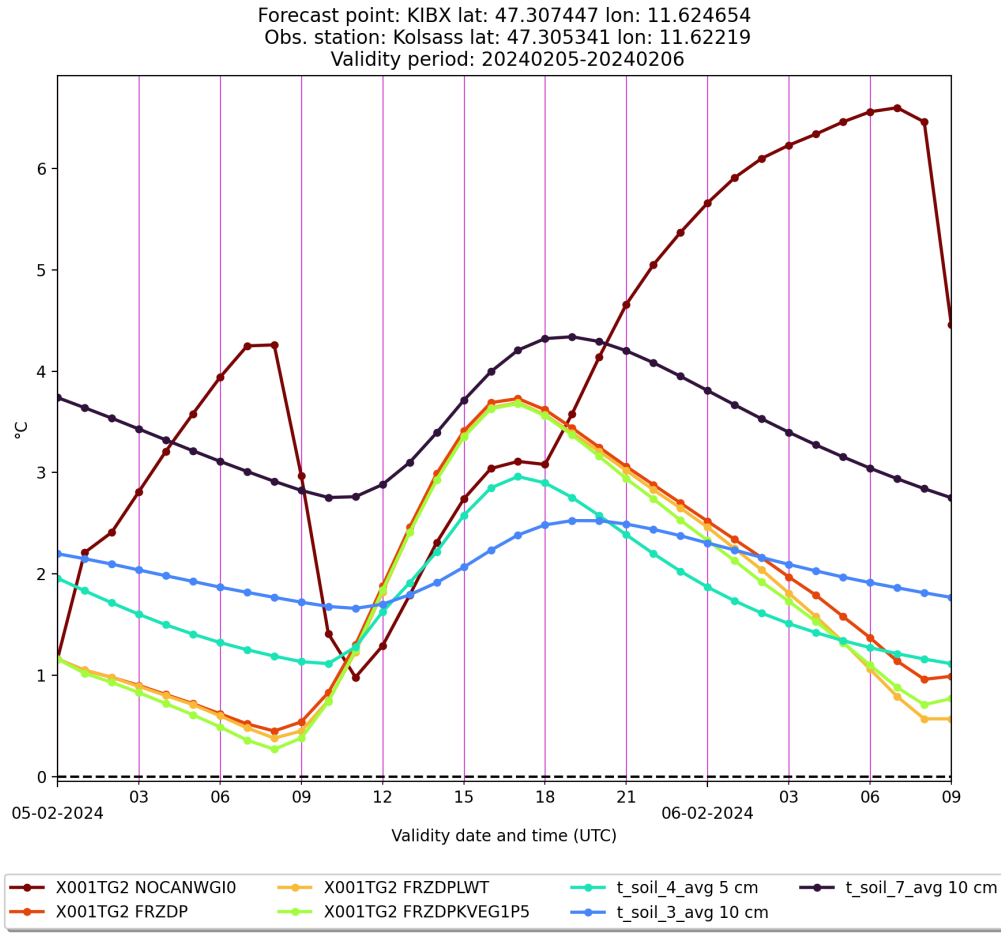


*Figure 2: Hourly soil temperatures observed at the i-Box Kolsass station and simulated at the nearest grid point. The deep-soil temperature (TG2) is shown for the NOCANWGI0, FRZDP, FRZDPLWT and FRZDPKVEG1P5 experiments. Soil temperature was measured at two sites located 5 m apart: t\_soil\_3 and t\_soil\_4 were measured at one site at depths of 10 cm and 5 cm, respectively, while t\_soil\_7 was measured at the second site at a depth of 10 cm.*

Unrealistic deep-soil temperature (TG2 variable) variations associated daily soil freeze-thaw cycles have been observed in C-LAEF 1k simulations, particularly in grid cells fully or largely covered by grass. For example, Figure 2 illustrates TG2 evolution in the NOCANWGI0 experiment, alongside more realistic simulations of the same variable in three additional experiments: FRZDP, FRZDPLWT and FRZDPKVEG1P5. The NOCANWGI0 experiment uses the configuration of the C-LAEF 1k control member, while the FRZDP experiment tests a modified version of the soil freezing and melting scheme used in ISBA’s force-restore mode, as described later in this section. In addition to this modification, the soil freezing characteristic curve (relating sub-zero soil temperatures to unfrozen water content) is activated in the FRZDPLWT experiment by setting the CSOILFRZ option to LWT. Another change relative to the FRZDP experiment is the reduction of the  $K_2$  coefficient in the vegetation insulation coefficient  $K_s$  (Le Moigne, 2018) from 5 to 1.5 in the FRZDPKVEG1P5 experiment to enhance the insulation effect of vegetation. All experiments used initial conditions from the NOCAN experiment described in the previous section, except for the initial soil water and ice contents. Soil ice was converted to soil moisture to initialise the model with ice-free soil, while keeping the total water content unchanged.

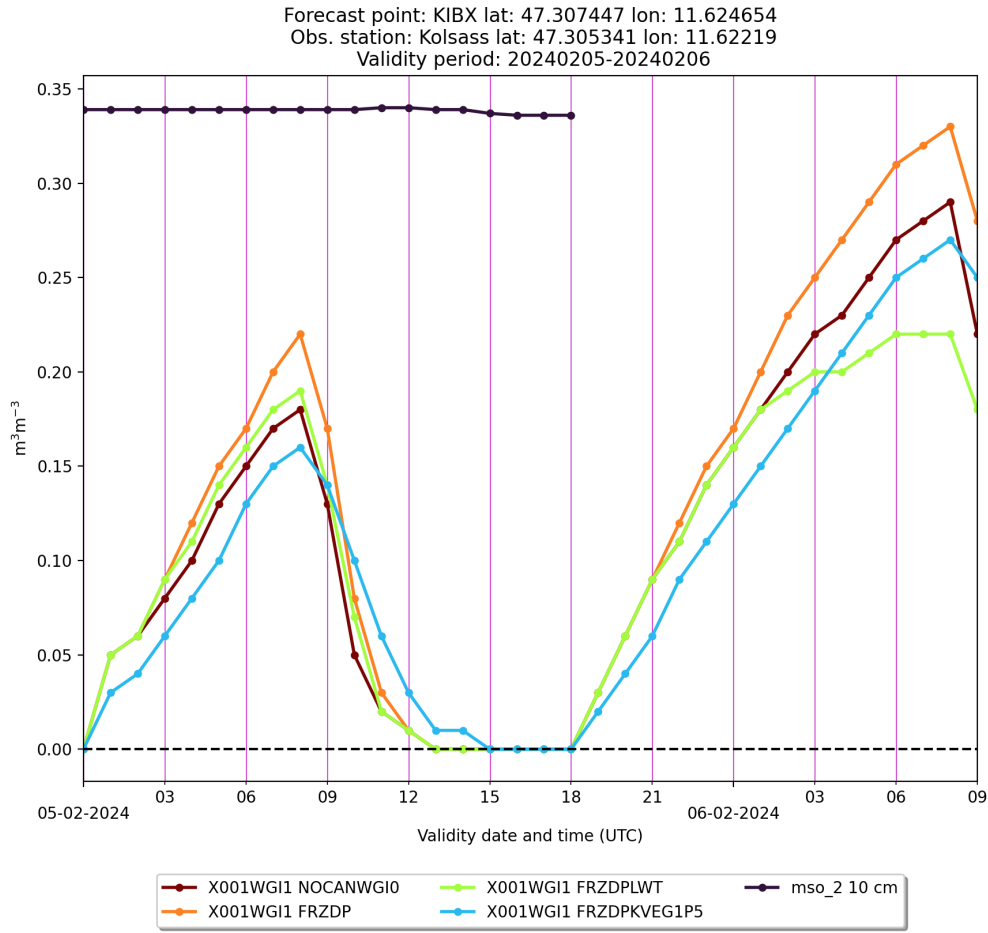


Figure 3: Hourly soil moisture observed at the i-Box Kolsass station at a depth of 10 cm, along with the hourly liquid water equivalent volumetric ice content of the 1-cm-thick surface soil layer simulated at the nearest grid point for the NOCANWGI0, FRZDP, FRZDPLWT and FRZDPKVEG1P5 experiments.

In the NOCANWGI0 experiment, TG2 rises by approximately 3 °C within the first seven hours, then decreases by more than 3 °C within just three hours during the morning in the simulation depicted in Fig. 2. A significant TG2 increase is also simulated after 18 UTC. These variations are primarily driven by the freezing and thawing occurring within the 1-cm-thick surface soil layer (Fig. 3). The high sensitivity of TG2 to these processes, while the subsurface layer remained ice-free throughout the integration (not shown), was deemed particularly unusual and prompted an investigation, leading to the revision of the soil freezing and melting scheme. It is important to note that, on its own, the nighttime warm bias of the surface temperature (TG1 variable, Fig. 4) would hardly suggest any anomalous behaviour of TG2.

The FRZDP experiment simulated a more realistic TG2 evolution, despite the increased production and melting of soil ice in the surface soil layer compared to the NOCANWGI0 experiment (Fig. 3). Additionally, the continuous nighttime decrease in surface temperature (TG1) in FRZDP is more realistic (Fig. 4). Consequently, the 2-meter temperature (T2M) also decreases (see Fig. 5), becoming more accurate under the clear-sky conditions and weak synoptic forcing of the experiment. In comparison to FRZDP, nocturnal soil temperatures TG2 and TG1, and consequently T2M, show further reductions in the FRZDPLWT and FRZDPKVEG1P5 experiments. This is due to the reduced latent heat release from a lower amount of ice produced during soil freezing in these experiments, compared to FRZDP.

The revision of the ISBA's soil freezing and thawing scheme applied in force-restore mode is described in this



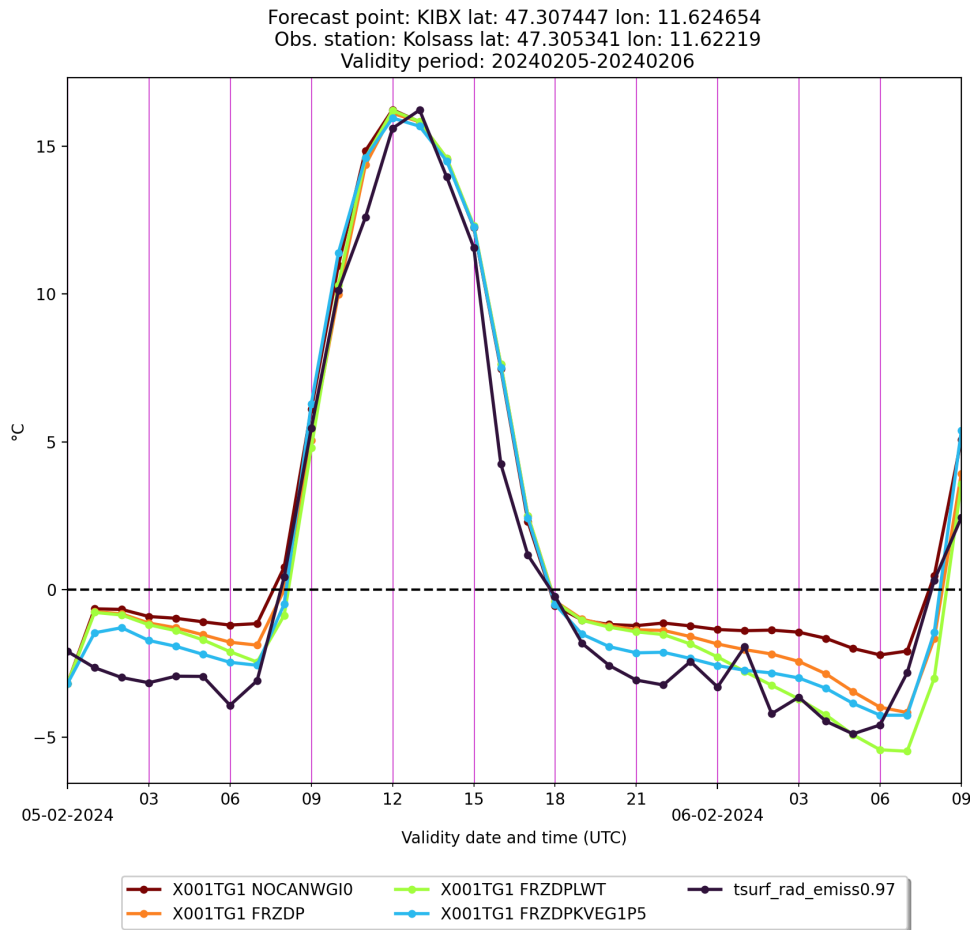


Figure 4: Hourly surface temperature simulated at the nearest grid point in experiments NOCANWG10, FRZDP, FRZDPLWT and FRZDPKVEG1P5. Also shown is the (radiative) surface temperature derived from the incoming and outgoing longwave radiation fluxes at the surface measured at the i-Box Kolsass station, assuming a surface emissivity of 0.97.

paragraph. In the original version, the deep soil layer is divided into a surface layer and a subsurface layer. Freezing and melting rates are calculated separately for each layer, following the method described by Boone et al. (2000). For the subsurface layer, these rates require soil liquid water and ice content values, which are derived from the prognostic variables of the surface and deep layers. The modifications tested in experiment FRZDP involve calculating freezing and melting rates for the entire deep layer rather than the subsurface layer, relying solely on the existing prognostic soil liquid water and ice contents of the entire deep layer. These modifications have been communicated to the SURFEX developers.

## 4 Summary and Outlook

A set of candidate changes has been proposed to upgrade C-LAEF 1k and reduce the nocturnal warm bias in Alpine valleys. Increasing surface turbulent fluxes under stable conditions by capping the bulk Richardson number at 0 has proven highly beneficial. The soil freezing and melting scheme used in ISBA's force-restore mode has been revised to eliminate the anomalous sensitivity of deep soil temperature to freezing and melting in the surface soil layer. This modification results in a more realistic simulation of deep soil temperature, which

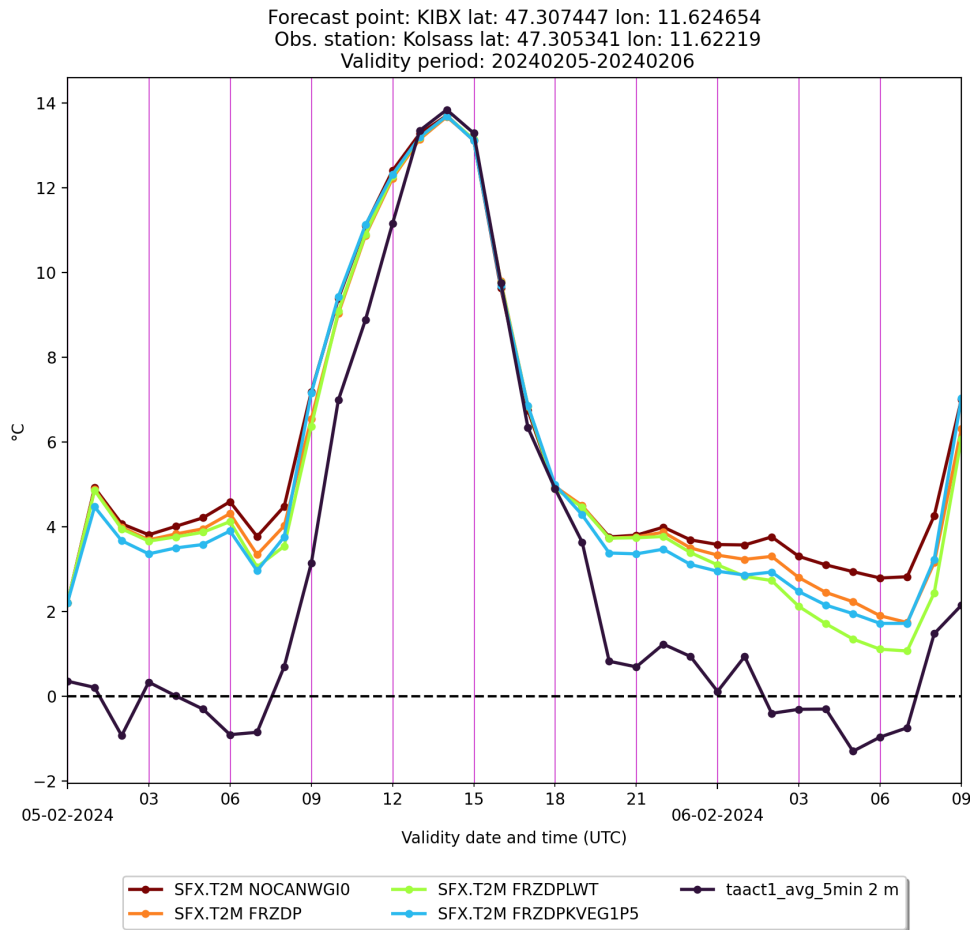


Figure 5: Hourly 2-m temperatures observed at the i-Box Kolsass station and simulated at the nearest grid point in experiments NOCANWG10, FRZDP, FRZDPLWT and FRZDPKVEG1P5. The hourly observed temperature is the average of 1-min observed temperatures over the preceding 5 min.

in turn reduces the nocturnal warm bias in both surface and 2-meter temperatures. This warm bias is further reduced by using the soil freezing characteristic curve and enhancing the insulation effect of vegetation. The combined impact of these changes will be assessed before their implementation in a system that will run in parallel with the pre-operational C-LAEF 1k system during the winter of 2024-2025.

## 4.1 Acknowledgements

We would like to thank Aaron Boone from Météo-France for testing the soil freezing modifications in SURFEX and providing valuable feedback. We are also grateful to Manuela Lehner and Lena Pfister from the University of Innsbruck for their help with the i-Box data. Daniel Deacu is funded through the Innsbruck Network for Weather and Climate Research (IWCR).

## 5 References

Boone A., V. Masson, T. Meyers, and J. Noilhan, The Influence of the Inclusion of Soil Freezing on Simulations by a Soil–Vegetation–Atmosphere Transfer Scheme, *J. Appl. Meteor. Climatol.*, 39, 1544–1569, 2000.

- Le Moigne, P., SURFEX scientific documentation, v8.1, 2018. Available at: [http://www.umr-cnrm.fr/surfex/IMG/pdf/surfex\\_scidoc\\_v8.1.pdf](http://www.umr-cnrm.fr/surfex/IMG/pdf/surfex_scidoc_v8.1.pdf) (last access: 4 November 2024).
- Masson V. and Y. Seity, Including Atmospheric Layers in Vegetation and Urban Offline Surface Schemes, *J. Appl. Meteor. Climatol.*, 48, 1377–1397, 2009.
- Meier F., C. Wastl, F. Weidle and C. Wittmann, Adapting the screening level diagnostics to improve AROME temperature forecasts in Alpine areas, *ACCORD Newsletter*, 1, 119–126, 2021.
- Rotach M., I. Stiperski, O. Fuhrer, B. Goger, A. Gohm, F. Obleitner, G. Rau, E. Sfyri and J. Vergeiner, Investigating Exchange Processes over Complex Topography: The Innsbruck Box (i-Box), *Bull. Amer. Meteor. Soc.*, 98, 787–805, 2017.
- Wastl C., Y. Wang, A. Atencia, F. Weidle, C. Wittmann, C. Zingerle, E. Keresturi, CLAEF: Convection-permitting Limited-Area Ensemble Forecasting system, *Quarterly Journal of the Royal Meteorological Society*, 147, 1431–1451, 2021.

# Analysis of Wind Shear Intensity at Constantine Airport

Imad Eddine Helali Mahiddine<sup>1</sup>, Mohamed Mokhtari<sup>1</sup> Khaled Deiboune<sup>(2)</sup>

<sup>(1)</sup>Numerical Weather Prediction Department, Office Nationale de la Météorologie, Algiers,ALGERIA

<sup>(2)</sup>Aeronautical Sciences Laboratory, Aeronautical and Spatial Studies Institute, BLIDA1 University, Blida, Algeria

## 1 Introduction

The study of wind shear is essential due to its substantial impact on aviation safety, particularly during takeoff and landing. Detecting and forecasting wind shear events are crucial steps in reducing potential hazards and enhancing flight safety. However, modeling these phenomena poses challenges, including the variability of wind patterns and the influence of terrain and atmospheric conditions.

Constantine, located in a mountainous region of Algeria, is especially prone to wind shear, given the complex interactions between its topography and prevailing wind patterns. This makes it an area of significant interest for understanding and mitigating the risks associated with sudden changes in wind speed and direction.

Figure 1 illustrates the monthly distribution of wind speed and direction at Constantine Airport, based on Windfinder data [1]. This wind rose shows the predominant wind directions and speeds for each month, with certain directions associated with higher wind speeds. The monthly variations observed underscore the importance of localized monitoring and tailored forecasting to improve safety around the airport.

The objective of this study is to analyze wind shear intensity at Constantine Airport, with a focus on identifying peak shear levels at critical altitudes and interpreting the wind shear output added to the AROME model. By examining specific periods with significant wind shear and assessing the influence of local topography, this study provides insights into local atmospheric conditions and potential impacts, supporting future work in wind shear analysis for this region.

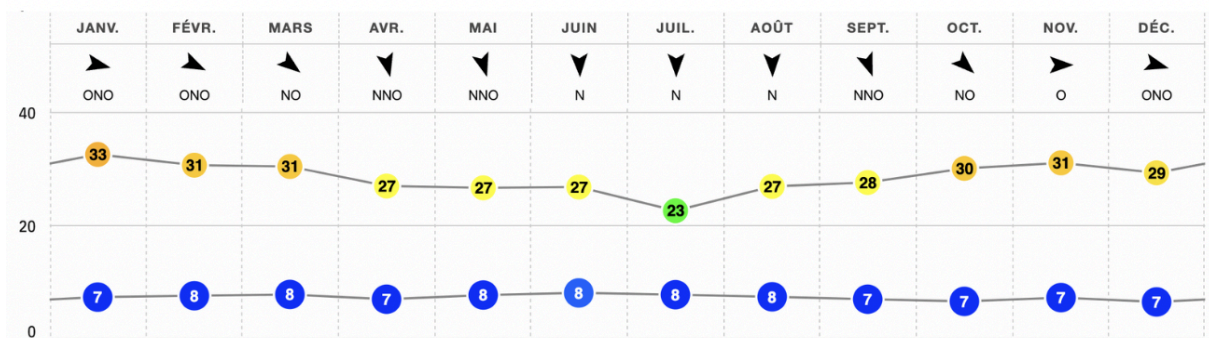


Figure 1: Monthly Distribution of Wind Speed (kt) and Direction at Constantine Airport [1]

## 2 Geographical Position and Orientation of Constantine Airport

The **Constantine Mohamed Boudiaf Airport** is located at an altitude of **685 meters**, in the heart of the Constantine province, within a mountainous region characterized by diverse topography.

The airport is surrounded by mountains with altitudes ranging from **880 to 1300 meters**. This terrain, with its deep valleys and mountain passes, plays a significant role in the dynamics of air masses, particularly by modifying their circulation and influencing the formation of local weather phenomena.

The geographical configuration of the airport means that it is often influenced by air masses coming from different directions. Maritime air masses, predominantly from the **West and Northwest**, interact with continental air masses coming from the **Southwest and South**. This interaction generates turbulence and rapid weather changes, which can directly affect airport operations.

The orientation of the airport's runways follows the dominant wind directions to optimize flight conditions. Indeed, during takeoffs and landings, it is crucial for aircraft to face into the wind. This orientation maximizes the lift of the aircraft, reducing the distance required for takeoff or landing. The configuration of the runways is designed to take advantage of the prevailing winds to ensure flight safety.

The two main runways at Mohamed Boudiaf Airport are oriented along the **337°-157°** and **314°-134°** directions, which allows the airport to benefit from the most frequent headwinds, especially those coming from the **Northwest** sector. These orientations were chosen based on the local climatology, which shows a dominance of winds from the **West-Northwest**.

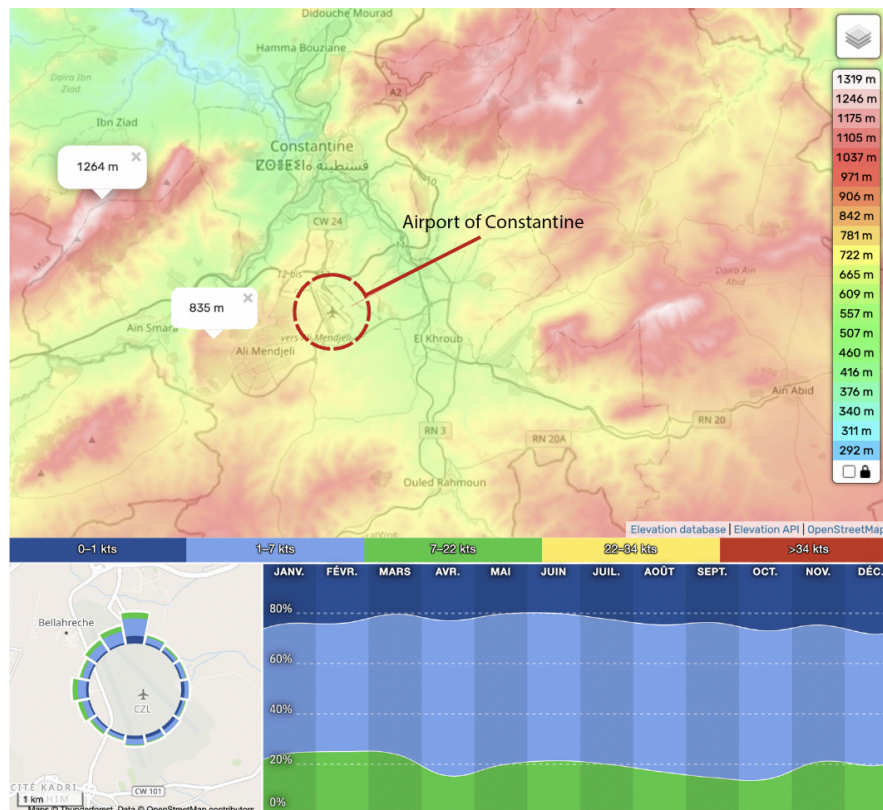


Figure 2: Geographical Location of Constantine Airport and Surrounding Mountain Ranges and Monthly Distribution of Wind Direction and Strength [1] [2]

### 3 Methodology

#### 3.1 Model Used

For this study, the **AROME model based on CY46 cycle** with 500 meters resolution was used to simulate atmospheric conditions around **Constantine Airport**. AROME is a high-resolution, non-hydrostatic, numerical weather prediction (NWP) model, which is well-suited for capturing small-scale atmospheric phenomena such as turbulence, wind shear, and localized convective systems. The model configuration is mentioned in the Table 1.

AROME was initialized and coupled with **boundary conditions** from **ALADIN** forecast models every 3 hours and generates outputs hourly.

Table 1: AROME 500m Constantine airport configuration

Model	AROME 500m	
Horizontal resolution	500 x 500 m	
Vertical resolution	41 levels	
Grid points	320*320	
Initial conditions	Aladin	
Forecast range	48 h	
Time Step	60s	
Area	<b>Lat</b>	35.61 – 36.95 N
	<b>Lon</b>	5.78 E – 7.44 E

#### 3.2 Development: Addition of the Shear Equation

To calculate **vertical wind shear**, the **APL\_AROME.F90** routine was modified to include the shear calculation, which is performed after the turbulence calculation block in the model's processing chain. Vertical wind shear is defined as the difference in wind speed between two adjacent vertical levels, providing an indicator of how rapidly the wind changes with height, which is a critical parameter for assessing turbulence and flight safety.

The formula :

$$V_{\text{shear}} = |V_{\text{level1}} - V_{\text{level2}}|$$

where:

**V<sub>level1</sub>**: The wind speed at the upper atmospheric level

**V<sub>level2</sub>**: The wind speed at the lower atmospheric level

In the code :



```

ZCIVERT=0.
ZDVENT=0.

DO JLEV=KLEV,2,-1

  DO JLON=KIDIA,KFDIA
    ZDVENT(JLON,JLEV)= &
      & (PUM(JLON,JLEV-1)-PUM(JLON,JLEV))**2 &
      & +(PVM(JLON,JLEV-1)-PVM(JLON,JLEV))**2

    ZCIVERT(JLON,JLEV)=sqrt(PUM(JLON,JLEV-1)**2 + (PVM(JLON,JLEV-1)**2) &
      & - sqrt(PUM(JLON,JLEV)**2 + PVM(JLON,JLEV)**2))

  ENDDO
  ZDVENT(JLON,1)=0.
  ZCIVERT(JLON,1)=0.

ENDDO

```

Once the **wind shear** has been computed within the model code, it is integrated into the model's output as a diagnostic variable, ensuring that it is available for further analysis. The shear values are stored and outputted in the relevant model diagnostic arrays.

In the code, the integration process is carried out as follows:

```

DO JLEV=1,KLEV
  DO JLON=KIDIA,KFDIA
    PEZDIAG(JLON,JLEV,5)=ZCIVERT(JLON,JLEV)
  ENDDO
ENDDO

```

The computed vertical wind shear values stored in the array **ZCIVERT** are transferred to the diagnostic array **PEZDIAG**. The third dimension of the **PEZDIAG** array (indexed by **5** in this case) corresponds to the specific diagnostic variable for vertical wind shear. This array will then contain the wind shear values at each horizontal grid point and vertical level, ready for output.

This integration ensures that the wind shear variable is seamlessly incorporated into the model's diagnostic system and outputs, making it a valuable addition to the meteorological data generated by the AROME model as FULLPOSS (pressure and geopotential levels) and ICMSH (model levels).

## 4.Meteorological Data : Study case of two days

This study focuses on two specific wind shear events identified by an **aerial operator**: one on February 2, 2023, and the other on June 8, 2024. These periods were chosen due to their significance in understanding wind shear phenomena during critical phases of flight, particularly during takeoff and landing. The study provides detailed shear maps, quantitative analyses, and comparisons with known critical thresholds for vertical wind shear. **Periods Analyzed:**

- **February 2, 2023:** Between **07:00 and 07:40 UTC**.
- **June 8, 2024:** From **11:25 to 11:40 UTC**, and from **19:05 to 19:25 UTC**.

The analysis focuses on the **altitude levels** ranging from **0 to 1000 feet**, a critical altitude zone for flight operations, specifically during the **takeoff and landing phases**. This range was selected because it is within the typical altitude band where wind shear can have the most significant impact on aircraft performance, especially in relation to **low-altitude flight dynamics**.

## 5. Results

The analysis of wind shear observed during the study periods revealed the following maximum values:

- **February 2, 2023:** A maximum wind shear of **6.973 m/s** was observed at **model level 40**, approximately **73 meters above the ground**, between **07:00 UTC**.

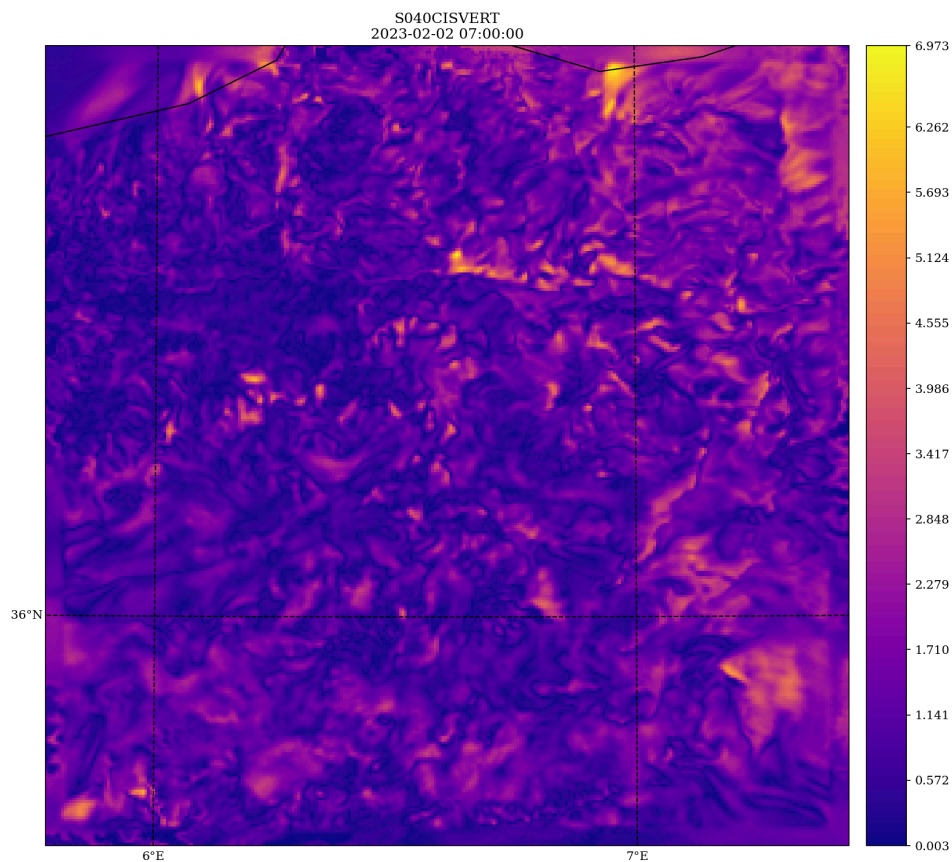


**Figure 3:** Wind Shear Distribution at Level 40 (~73 meters from the ground) over Constantine Airport, February 2, 2023, at 7 UTC

- **June 8, 2024:** A maximum wind shear of **13.5 m/s** was recorded at **model level 39**, approximately **99 meters above the ground**, at **19:00 UTC**.

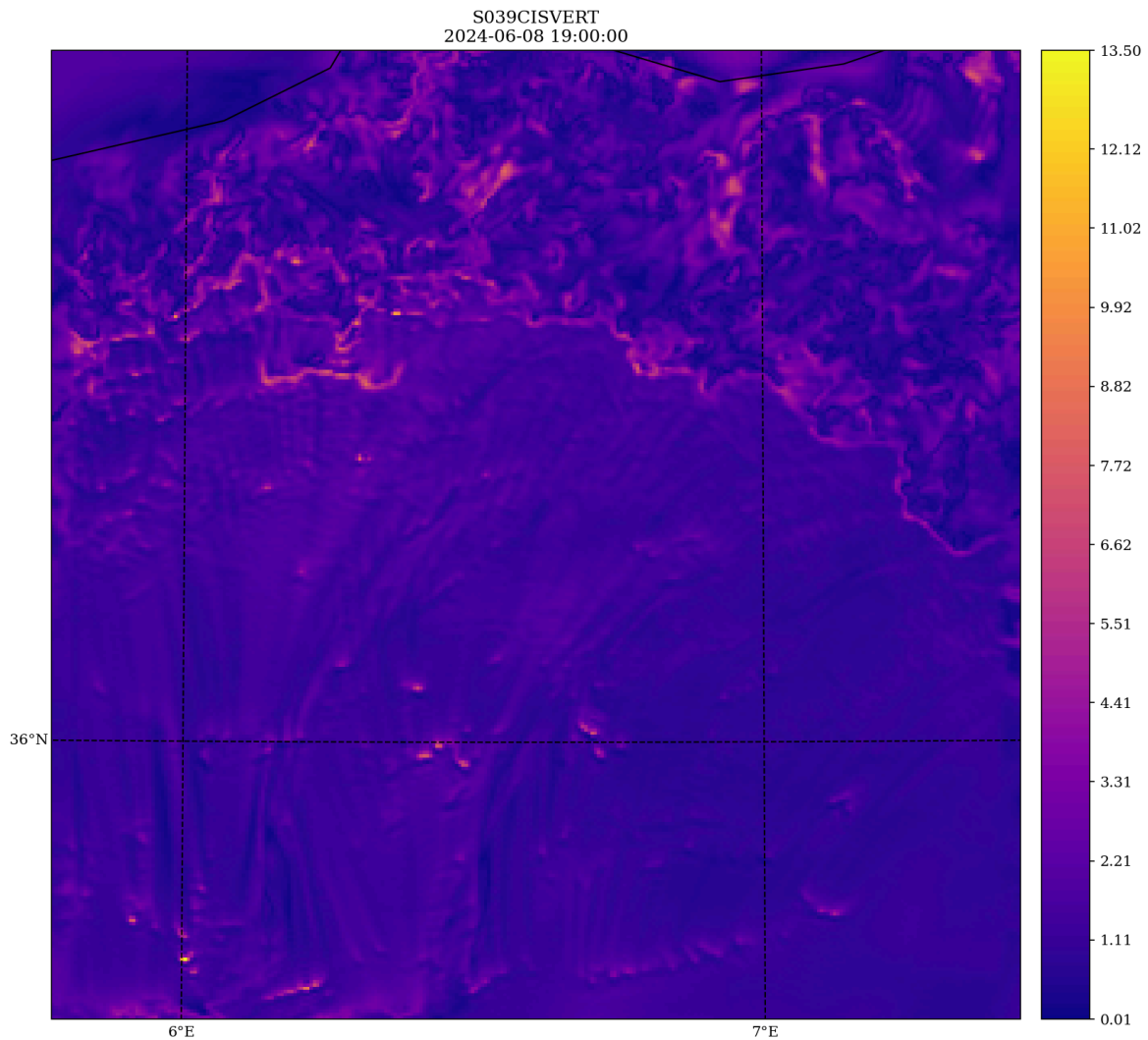


**Figure 4:** Wind Shear Distribution at Level 39 (~99 meters from the ground) over Constantine Airport, June 8, 2024, at 19 UTC .

These shear values exceed the critical thresholds established for aviation safety, which are commonly defined as follows: [3]

- **Strong wind shear:** Between 4-6 m/s.
- **Severe wind shear:** Between 6-10 m/s.
- **Critical wind shear:**  $\geq 10$  m/s.

These results indicate that during the analyzed periods, the shear experienced around the airport could pose a significant risk, particularly during the **takeoff and landing** phases, where aircraft are most sensitive to wind-related disturbances.

## 6. Discussion

The simulated wind shear values, especially on June 8, 2024, where the shear reached 13.5 m/s, suggest a considerable risk during the critical flight phases (takeoff and landing). The most intense shear values were recorded at low altitudes, which is typical for the critical height zone, where aircraft

are highly vulnerable to fluctuations in wind speed and direction. Shear at these altitudes can lead to flight instability, loss of control, and other safety hazards.

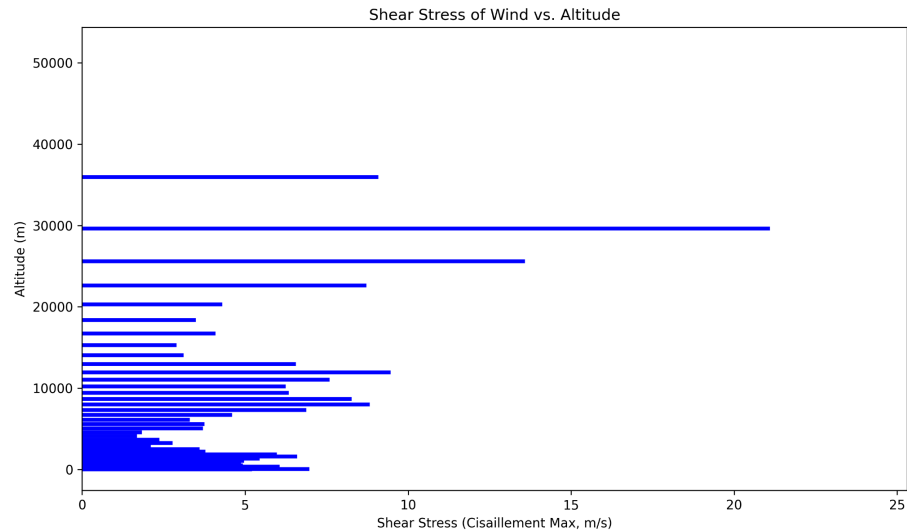


**Figure 5:** Vertical Profile of Maximum Wind Shear simulated by AROME over Constantine Airport for February 2, 2023 at 7 UTC; This vertical section bar represents the wind shear intensity at various model levels for February 2, 2023, showing how shear changes with altitude.

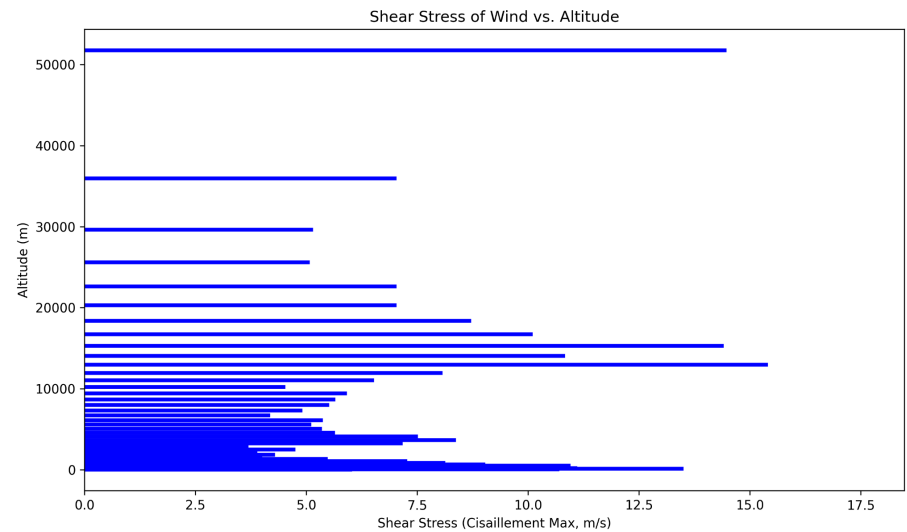


**Figure 6:** Vertical Profile of Maximum Wind Shear simulated by AROME over Constantine Airport for June 8, 2024 at 19 UTC; This vertical section bar depicts the maximum observed wind shear at different altitudes on June 8, 2024, highlighting the shear distribution at various levels.

In aviation, the critical wind shear threshold is generally considered to be around 4 m/s at low altitudes, as this value significantly impacts aircraft maneuverability and performance [3]. The study shows that shear values exceeded this threshold, particularly on June 8, 2024, where the maximum shear of 13.5 m/s was recorded. This level of shear is considered severe and may pose substantial risks during the takeoff and landing phases.

The rugged mountainous terrain surrounding Constantine airport significantly contributes to the intensification of wind shear. The interaction of wind with the complex topography, including valleys and mountain ridges, causes rapid fluctuations in wind speed and direction. These conditions exacerbate wind shear at low altitudes, requiring heightened situational awareness from flight crews and constant monitoring of wind conditions in the area. Aircraft operating in this region must be prepared for variable wind patterns that could affect stability during the takeoff and landing phases.

## 7. Perspective

---

Building upon the findings of this study, future research will aim to extend the analysis of wind shear at **Constantine airport** over a **longer time period** to better understand the **seasonal variations** and **long-term trends** in wind shear intensity. This expanded timeframe will allow for a more comprehensive understanding of the frequency, intensity, and distribution of wind shear events throughout the year, particularly in relation to the different **meteorological conditions** and **topographical influences**.

Furthermore, future studies will incorporate the **direction of wind shear** alongside its intensity. The directional component is crucial for understanding how wind shear impacts aircraft depending on its orientation relative to the **flight path**. By analyzing both the intensity and direction of wind shear, we can gain deeper insights into the **spatial variability** of shear events and their potential **impact on flight safety** during takeoff and landing phases.

The integration of wind shear direction will also enable the development of more **precise forecasting tools** and **early warning systems**, tailored to the specific needs of **Constantine airport** and similar locations with challenging terrain. This directionality analysis will be crucial in providing a more **holistic view** of the wind shear phenomena, allowing **aviation authorities** and **pilots** to take appropriate precautionary measures in real-time.

By expanding the temporal scope and adding wind shear direction to the analysis, the next phase of this study will provide a more **robust dataset** for aviation safety, helping to mitigate risks and optimize flight operations in the region.

## 8. References

---

- [1] **Windfinder.com**. Source for wind direction and frequency data used in Figures 1 and 3. Accessed from <https://www.windfinder.com>.
- [2] **Topographic-map.com**. Source for topographical data used in Figure 2 to represent the surrounding terrain and altitude variations around Constantine airport. Accessed from <https://www.topographic-map.com>.
- [3] **METWSG/1-SN No. 6 - Appendix A**. Threshold values for wind shear severity in aviation safety assessments. This reference outlines critical thresholds used to categorize wind shear intensity and assess potential risks to aviation.

# Recent developments in ACCORD Poland team

Piotr Sekuła, Jadwiga Róg, Gabriel Stachura, Natalia Szopa, Małgorzata Szczęch-Gajewska, Marcin Kolonko, Bogdan Bochenek

## 1 Introduction

The operational configuration of ALARO and AROME remains the same. The new topics are 1h LBC (by Małgorzata Szczęch-Gajewska and Piotr Sekuła), ensemble forecasts using AI weather models (by Jadwiga Róg). Gabriel Stachura continues comparison of ISBA snow schemes.

## 2 Verification of ALARO-1 CY46T1 and test of 1h LBC

### CY46T1 test runs

Tests started in Feb 2024 and lasted until May 2024. 4 packages were applied into this export version (CMC). There is significant improvement of verification results on the new CMC in relation to CY43 version (see orange lines on Figure 1). Example fields are T2m, RH2m and 10m wind speed.

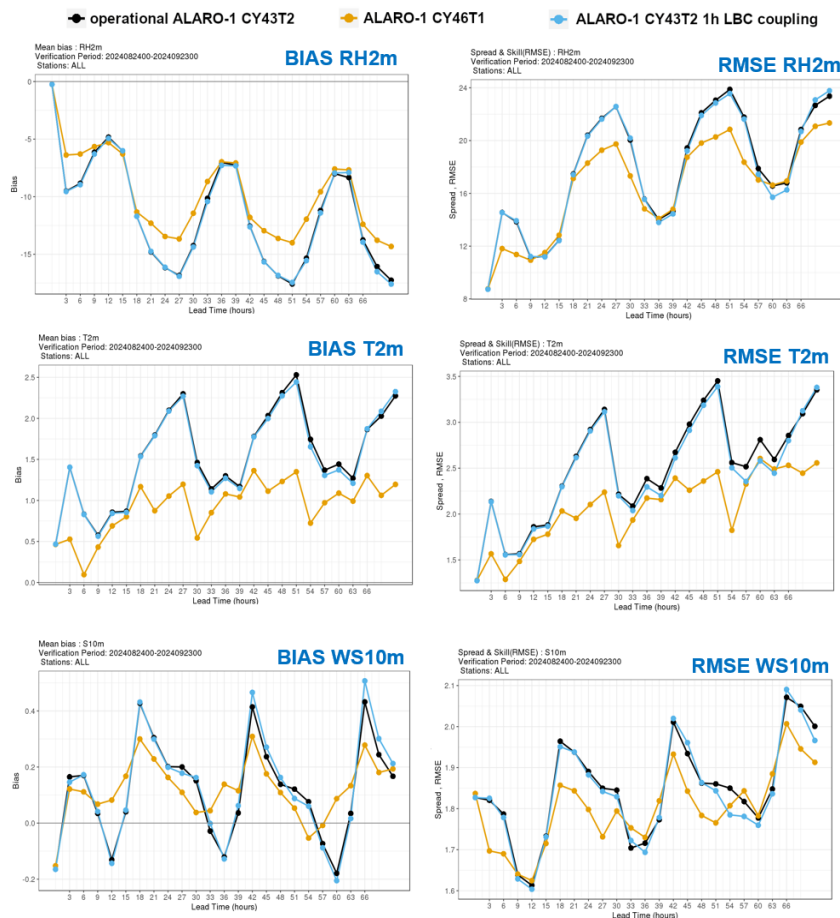


Figure 1. The verification scores (left BIAS and right - RMSE) for RH2m, T2m, WS10m and WD10m . Operational fcst in black, 1h LBC in blue and ALARO CY46 version in orange (the best scores).



### CY43T2 1h LBC tests

New version of ARPEGE enables higher frequency of LBC – 1 hour instead of 3 hours. Tests were performed from the beginning of 2024. No significant improvement was noticed, verification results for example meteorological field are presented on Figure 1.

## 3 Ensemble forecasts using AI global weather models

---

### Model information

This work is relying on FourCastNet data-driven global NWP model [1][2]. The training sample was ERA5 reanalysis for 1979-2015. It involved 20 meteorological variables (5 on the surface level). Timestep is 6 h, spatial resolution 0.25 degrees and final grid is 720x1440 point map of predicted values.

Such ensemble forecast can count either the constant number (e.g. 128) of forecasts or increasing one (2 to the power of time steps number, with n from 1 to 7). These two approaches are compared below.

### Methodology and data

The experiment generated AI-driven ensemble forecasts. Only 3 surface variables (T2m, wind speed at 10m and mean pressure at the sea level) were considered. The testing period was Jun 2024, with the model being run each day at 00:00 UTC for 7 timesteps (max. 42 hours lead time).

Additional data was from 54 synoptic stations to calculate RMSE of the forecasts. Then the data for both approaches (2 to the power of n or constant number of ensemble members) were processed and the results compared.

### Results

**Air temperature** (Fig. 2): Variable with the highest RMSE values. The mean RMSE values initially decrease with time. For the increasing ensemble count, 4th timestep has lowest RMSE, which corresponds to 00:00 UTC the next day of the forecast. For the constant ensemble count it's the 5th timestep, 06:00 UTC. We speculate that the variation in RMSE is tied to the amplitude of temperature during the diurnal cycle, and daytime temperature fluctuating more than nighttime one. The error for the 1st step with 2 ensembles is 0.4°C lower than with 128 ensembles, but otherwise the model with the constant ensemble count seems to perform better.

**Wind speed** (Fig. 3): Calculated from zonal + meridional components. The constant count method performs better, but not as visibly as for other variables. The increasing method's error is smaller on 4th and 5th timestep. The lack of trend may be tied to the natural variability of wind speed.

**Pressure** at sea level (Fig. 4): RMSE is, more predictably, rising with every step. Along with the ensemble count increasing from 2 to 128 consistently worse results appeared, even though there is almost no difference between the methods at the beginning. The biggest difference (over 0.4hPa) is on the 5th timestep.

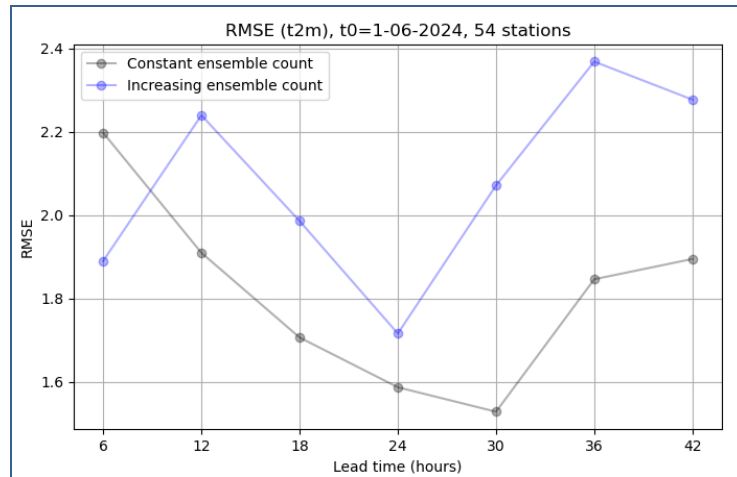


Figure 2. T2m RMSE for 54 stations and two kinds of FourCastNet ensembles.

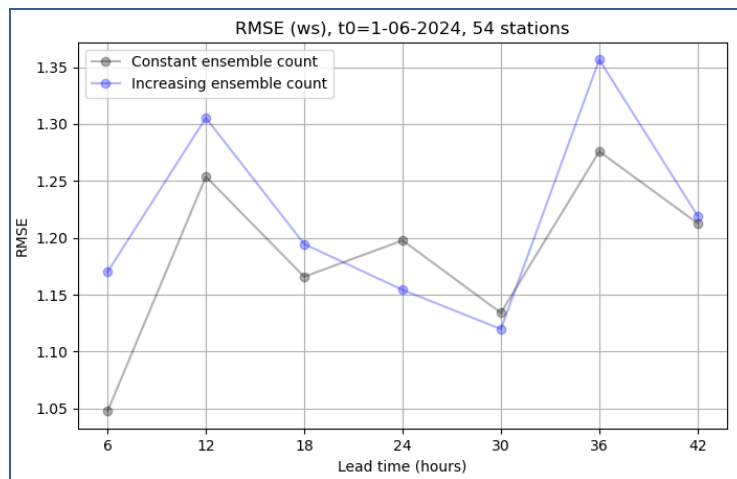


Figure 3. Wind speed RMSE for 54 stations and two kinds of FourCastNet ensembles.

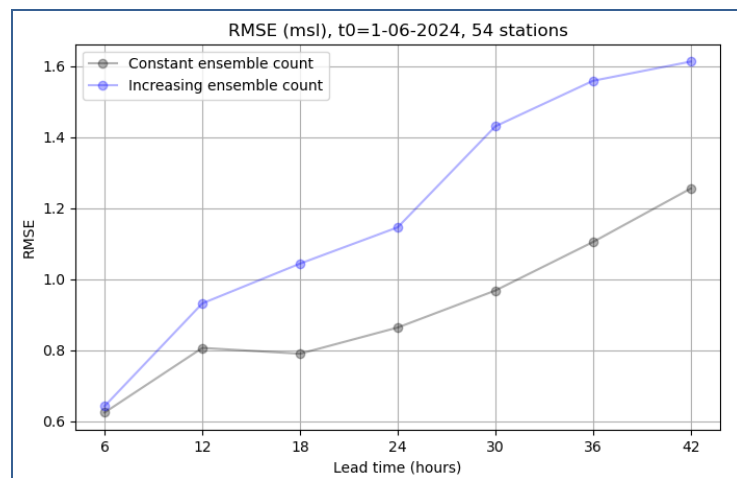


Figure 4. The same as Figs 3 and 4, but for mean pressure at sea level (msl).

## 4 Comparison of ISBA snow schemes in SURFEX

### Methodology and data

Four snow schemes available in SURFEX 8.1 have been compared and verified regarding snow properties. These are two-layered, composite schemes (D95 and EBA) and two multi-layered schemes: Explicit Snow Scheme (ESS) and CROCUS. Basic setup of the experiments is listed in Table 1. The only parameters changed in the namelist were CSNOW and CISBA.

Comparison spans from November 2023 to March 2024. Two snow variables were evaluated: snow depth (SD) and snow water equivalent (SWE). On the Fig. 5 below one can see the SWE results from three stations: a high-mountain station (SBSL, 1523 m a.s.l.), a mountain-valley station (ZAKO, 857 m a.s.l.) and a lowland station (SUWALKI, 184 m a.s.l.). The metrics on the charts were calculated only for cases where snow cover was present.

Table 1: SURFEX setup used in the experiment

Forcing model	AROME (2.5 km)
Forcing frequency	1 h
Forecast length	24 h
Forecast timestep	900 s
NPATCH	1
CISBA	DIF / 2-L
TEB	Off
CSNOW	CRO / 3-L / D95 / EBA
Data assimilation	Off

### Conclusions

In the period of snow accumulation, D95, ESS and CROCUS perform roughly similar. EBA is the only scheme which moderately underestimates snow cover. During melting episodes, EBA responds the fastest and corresponds to observations the best. Other schemes respond with a delay and reduce snow cover insufficiently, which is most visible in spring. In D95 scheme, melting is extremely delayed. ESS and CROCUS are very similar regarding snow depth. SWE is considerably larger in ESS. In spring, ESS melts snow faster than CROCUS. Overall metrics favour EBA as the most accurate snow scheme. However, it has to be investigated more deeply whether this is not due to some existing biases or limitations in EBA that offset overestimation of snow (e.g. positive bias of surface temperature as there is only one composite surface temperature, or low upper threshold of snow density ( $300 \text{ kg/m}^3$ ) which in reality is easily exceeded in the mountains).

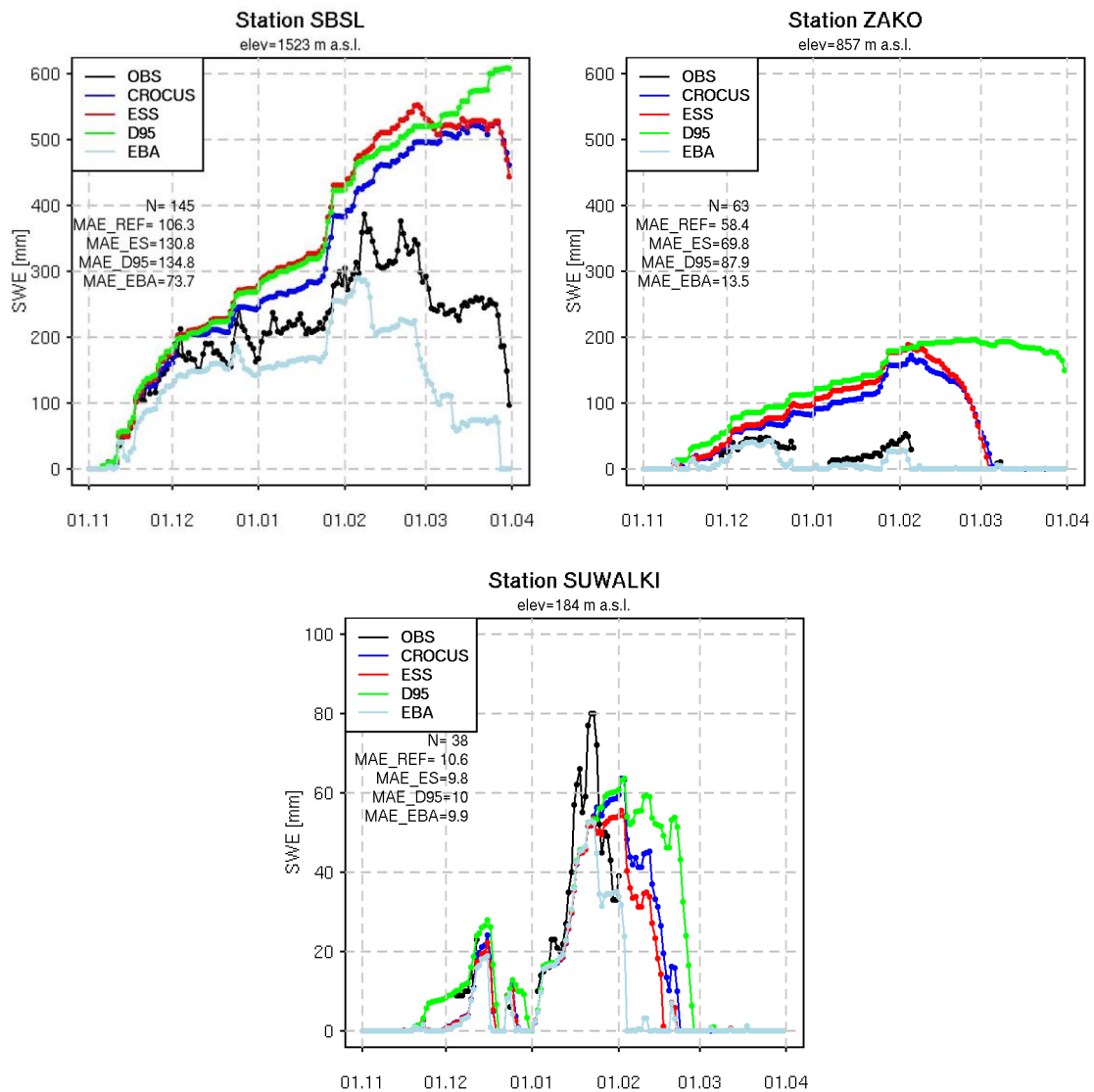


Figure 5. Forecasted and observed SWE for stations SBSL, SUWALKI and ZAKO in winter season 2023/2024.

## 5 References

- [1] FourCastNet, [last access 23.07.2024] <https://github.com/NVlabs/FourCastNet>  
 [2] FourCastNet (by Filip Øskar Łanecki), [last access 23.07.2024] <https://github.com/orhid/FourCastNet>

# Patricia around ACCORD 26 beautiful countries in 2024

Patricia Pottier

<http://pottier.pat.meteo.free.fr/>

# 1 “C'est la vie !”

2023 ended on a high note with a surprise visit to the ACCORD Assembly in Reading, and 2024 began in much the same way, with reading and research to prepare the itinerary for a 3-month spring trip to Slovenia, Croatia, Austria and .....

Things didn't go exactly to plan in 2024 ('c'est la vie', as Jean-François would have said).

Spring involved a lot more manual activities at home than walks outside. The long waits at the hospital to visit my parents after their car accident were an opportunity to make huge progress in amigurumi! and the fact that we had to postpone our big spring trip had the advantage of allowing me to pop up at a coffee break and meet the participants in the Strategic Workshop in Toulouse, at least that's what I thought in April. Unfortunately, I broke my foot just before the workshop. So, definitely, no spring trip in 2024, not even to Meteo-France CIC !... and a lot more amigurumi.

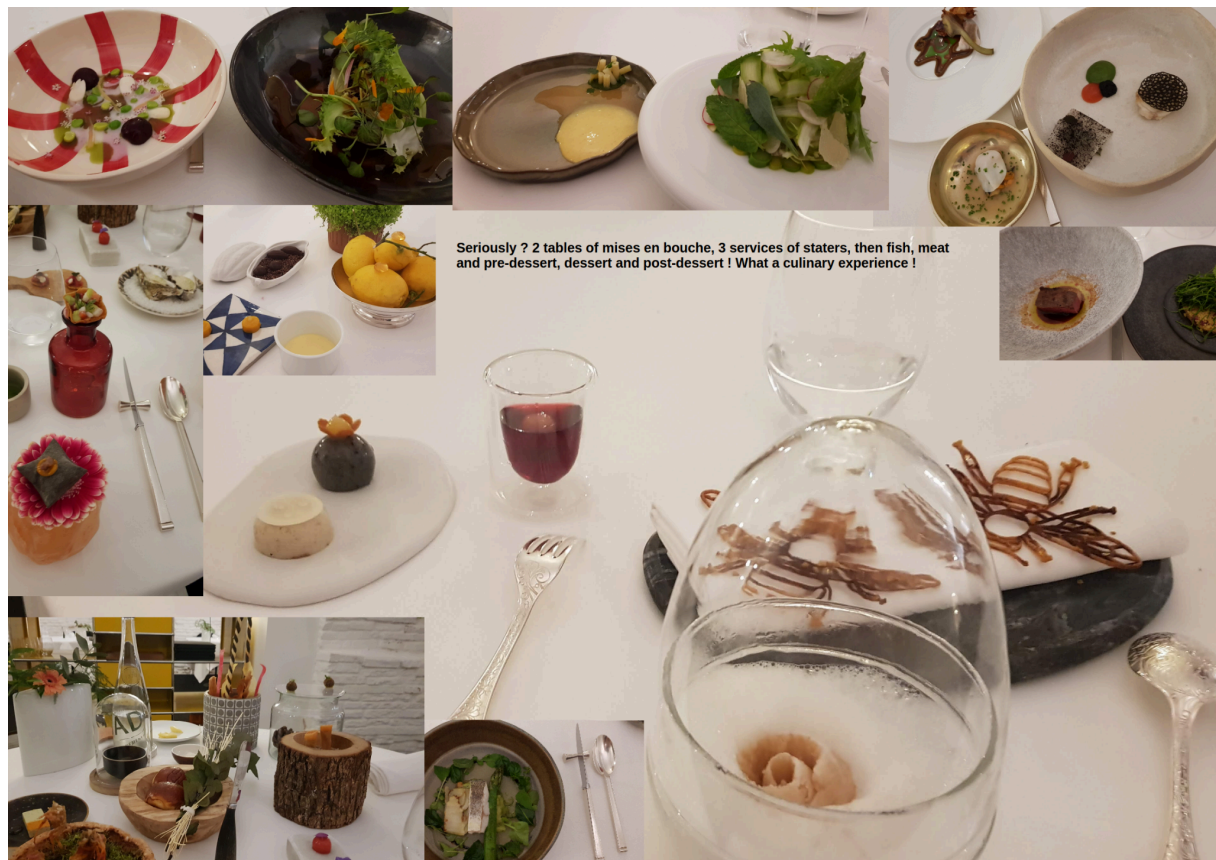


The orchid that my colleagues at GMAP gave me when I left didn't survive, even though I bathed it and

talked to it (I really don't have a green thumb)! I took advantage of my prolonged immobility to replace it with a crocheted version, which should survive just fine!



## 2 Gastronomic experience



At the end of June, to celebrate almost a year of retirement and thanks to a gift from my GMAP colleagues, we enjoyed a wonderful gastronomic experience with the 'Spectacle in 8 courses' menu at the Py-R restaurant in Toulouse. Seriously? 2 'mise en bouche' tables, 3 courses of starters, then fish, meat and pre-dessert, dessert and post-dessert!

## 3 Heading east, at last

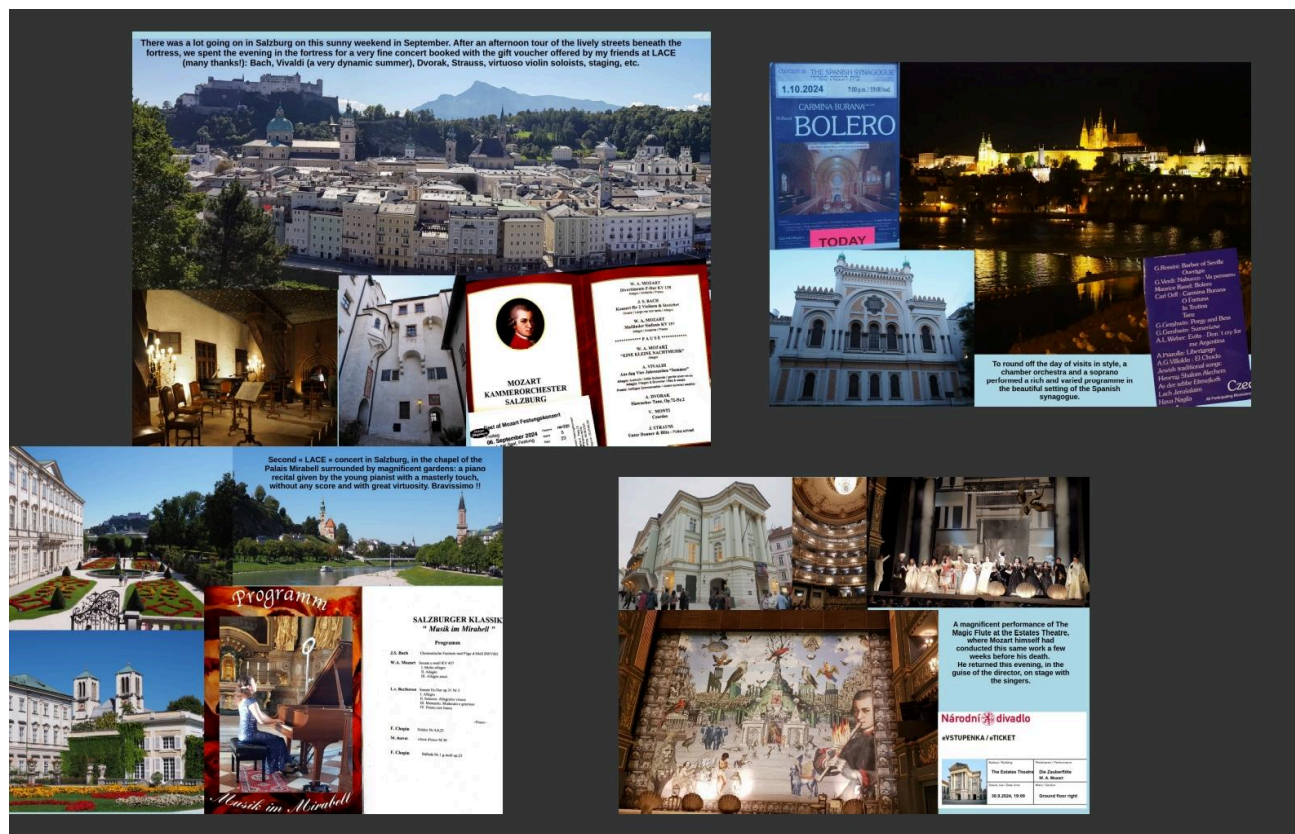




At the end of August 2024, just as the summer holidays were coming to an end for many, we headed east for 2 months. Austria, Slovakia, the Czech Republic: an incredible trip with beautiful landscapes, great visits and concerts offered by my friends from LACE.

A magnificent trip indeed... even if it didn't go entirely to plan.

The itinerary had to be adapted to avoid the worst of the flooding in Central Europe, thanks to the vigilance pages on the CHMI and SHMU websites. We made it through the bad weather unscathed and had a great time, including concerts in Salzburg and Prague, and the opportunity to meet up with friends during EWGLAM.



In the Salzburg fortress, we enjoyed a very fine concert booked with the gift voucher offered by my friends from LACE: Bach, Vivaldi (a very dynamic summer), Dvorak, Strauss, with virtuoso violin soloists. The second 'LACE' concert in Salzburg took place in the chapel of the Mirabell Palace, surrounded by magnificent gardens: a piano recital given by the young pianist in masterly fashion, without scores and with great virtuosity. Bravissimo!

A magnificent performance of The Magic Flute was given at the Prague State Theatre, where Mozart himself had conducted the same work a few weeks before his death. He returned to the stage with the singers, in the guise of the director.

The fourth of the LACE concerts was a chamber orchestra and a soprano who performed a rich and varied programme in the magnificent setting of the Spanish synagogue.

Many thanks to the friends of LACE for these magical moments!





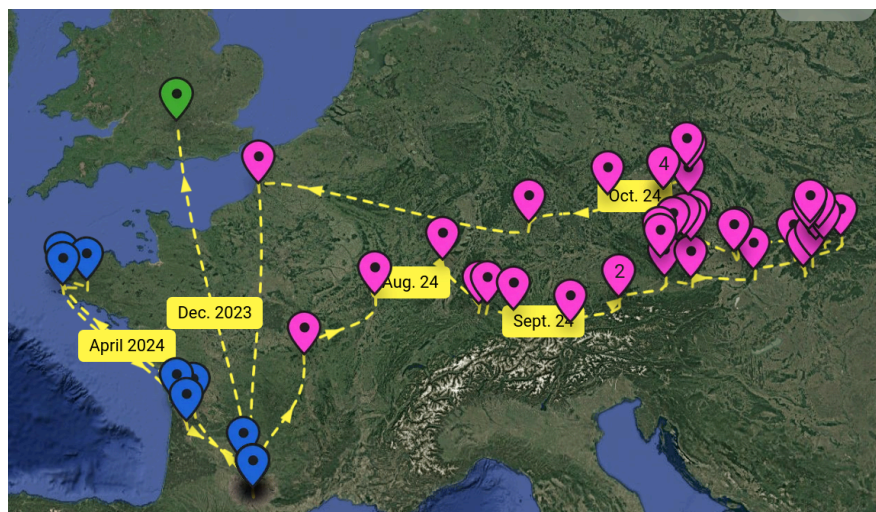
After Prague and getting lost in the nearby Czech paradise, the plan was to return via Belgium and visit the Plat Pays. Unfortunately, we had to return home earlier and more quickly than planned. But there's no place like home... even if the house has been visited by intruders and needs a bit of tidying up and cleaning!

Clearly 2024 is not my year... Can't wait for 2025!

## 4 Travel blog

The [travel blog](#) offers for real-time or slightly delayed photos during trips, and also this year some

photos from home (by chance, some nice guys visited our garden when we were stuck at home).



You can zoom in by using CTRL + scroll wheel; click on a pin (blue in France, rose in Austria, Slovakia and Czech Republic) to open the slide for that location and double-click on the slide to enlarge it. Once the slide is open, you can move from one slide to another using the arrows (please note that the slides

appear in reverse chronological order, with the most recent first). Comments are very welcome.

## 5 Slide shows of the travel blog

The travel blog is updated during trips and pages piled up in anti-chronological order. Once back home after a trip, I made a slideshow of it as some kind of photobook.

The [Volume 2](#) was published in November 2024 with the first semester in France, followed by trips to Austria, Slovakia, the Czech Republic, with a few stops in Germany.

### Patricia around ACC RD 26 beautiful countries

#### [Vol.2 Nov. 2024]


**DEC 2023:** Surprise visit at the ACCORD Assembly in Reading

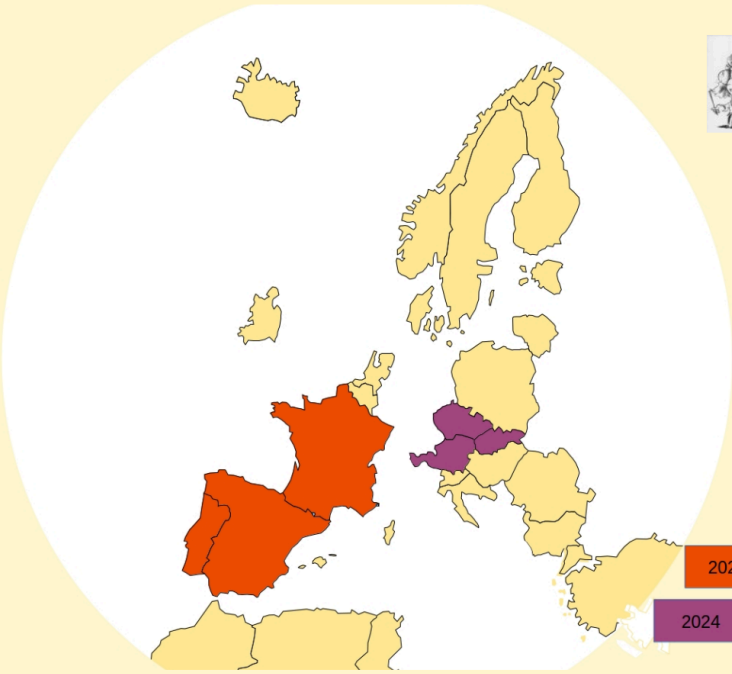

**EARLY 2024:** the itinerary for the big spring trip is ready

**SPRING-SUMMER 2024:** Stuck at home, spring travel postponed until 2025, amigurumi, gastronomy and garden visitors

**SEPT.-OCT. 2024:** finally, Austria, Slovakia, the Czech Republic, beautiful landscapes, lovely towns, LACE concerts and friends at EWGLAM

Not exactly what was originally planned for 2024, but ... it was better than we expected !



**Real-time Travel blog:** [https://padlet.com/pottierpatmeteo/Around accord 26 beautiful countries](https://padlet.com/pottierpatmeteo/Around%20accord%2026%20beautiful%20countries)

To find about more about these trips to our 26 beautiful countries and to keep in touch, visit: <http://pottier.pat.meteo.free.fr/>



# Previous editions of the ACCORD Newsletter

Anne-Lise Dhomps, ACCORD Consortium Scientific Secretary



[1st ACCORD Newsletter](#),  
published on 5 October 2021



[2nd ACCORD Newsletter](#),  
published on 28 February 2022



[3rd ACCORD Newsletter](#),  
published on 24 October 2022



[4th ACCORD Newsletter](#),  
published on 19 June 2023



[5th ACCORD Newsletter](#),  
published on 27 March 2024

The joint ALADIN-HIRLAM Newsletter (2013-2021, 16 editions) can be found on the [ALADIN dedicated webpage](#).

### Elaboration of the ACCORD Newsletters

For the concrete writing of an article, please refer to the editorial guidelines, accessible at: <http://www.accord-nwp.org/?Recommendations-templates>

The newsletter content is based on voluntary contributions by the scientists and the teams in the consortium. We want it to be a useful tool for sharing both “practical” information and experience (code engineering, quality assurance, system aspects) and “more fundamental” results (advances in research work, outcome of specific meetings or working days etc.).

NL7 is expected for mid-2025, however contributors can upload their material at any time during the year [on this shared folder](#). Do also not hesitate to encourage scientific contributions by young scientists (PhDs, post-docs etc.) or technical contributions (codes, porting, optimization etc.).